

Reaction and Diffusion on the Sierpinski Gasket

Riley, Caroline J.

2006

MIMS EPrint: **2007.6**

Manchester Institute for Mathematical Sciences
School of Mathematics

The University of Manchester

Reports available from: <http://eprints.maths.manchester.ac.uk/>

And by contacting: The MIMS Secretary
School of Mathematics
The University of Manchester
Manchester, M13 9PL, UK

ISSN 1749-9097

Reaction and Diffusion on the Sierpinski Gasket

A thesis submitted to the University of Manchester for the degree of
Doctor of Philosophy
in the Faculty of Engineering and Physical Sciences.

2006

Caroline Jane Riley

School of Mathematics

Contents

Abstract	10
Declaration	11
Copyright Statement	12
Acknowledgements	13
1 Introduction	14
2 Fractals and Laplacians	27
2.1 Iterated Function Systems and Self-Similar Sets	27
2.2 Energy and Harmonic Functions on the Sierpinski Gasket	36
2.3 Defining the Laplacian on the Sierpinski Gasket	40
2.3.1 Physically-Motivated Derivation	42
2.4 Other p.c.f. Self-Similar Sets	45
3 Spectrum and Eigenfunctions of the Laplacian on the Sierpinski Gas-	
ket	50
3.1 Introduction	50
3.2 Eigenvalues of the Laplacian on the Sierpinski Gasket	52
3.2.1 Eigenvalues of $-\mathcal{H}_m^0$ (Dirichlet Boundary Condition)	52
3.2.2 Eigenvalues of $-\mathcal{H}_m$ (Neumann Boundary Condition)	61

3.2.3	Properties of the Eigenvalues of $-\Delta$	65
3.3	A Problem with \mathcal{H}_m and a Solution	68
3.4	Localised Eigenfunctions of the Laplacian on the Sierpinski Gasket	70
4	The Cable Equation	73
4.1	Introduction	73
4.2	Derivation of the Cable Equation	75
4.2.1	Definition of Parameters	75
4.2.2	Derivation of the Cable Equation	78
4.2.3	Space and Time Constants	80
4.3	The Solution of the Cable Equation on the Sierpinski Gasket	81
4.3.1	Dirichlet Boundary Conditions	83
4.3.2	Neumann Boundary Conditions	88
4.3.3	Conclusion	92
5	FitzHugh-Nagumo Type Models	94
5.1	Introduction	94
5.2	Excitable Media	94
5.3	Hodgkin-Huxley Theory	96
5.3.1	The FitzHugh-Nagumo Model	98
5.4	The Heart as an Excitable Medium	100
5.5	Wave Solutions of a Modified FitzHugh-Nagumo System-Euclidean Domain	103
5.5.1	Planar Wave Fronts in Two Dimensions	103
5.5.2	Curved Wave Fronts in Two Dimensions	111
5.6	Wave Solutions of a Modified FitzHugh-Nagumo System-Sierpinski Gasket	114
5.7	Spiral Waves Solutions of a Modified FitzHugh-Nagumo System	120
5.7.1	Spirals Waves in the Myocardium	120

<i>CONTENTS</i>	3
5.7.2 Spirals on the Sierpinski Gasket	127
6 Conclusions and Further Work	144
Bibliography	154

List of Figures

1.1	The approximating sequence E_0, E_1, E_2, E_3 and E_7 to the Cantor Set.	15
1.2	The approximating sequence E_0, E_1, E_2, E_3 and the Koch Curve. . .	20
2.1	Generating the Sierpinski Gasket when the initial set is (a) a circle, and (b) a square.	29
2.2	The approximating sequence $\Gamma_0, \Gamma_1, \Gamma_2$ and the Sierpinski Gasket. . .	31
2.3	The overlap of $f_1(K)$ and $f_3(K)$ is a single point.	32
2.4	The harmonic extension from Γ_0 to Γ_1	37
2.5	The star-triangle transformation for Hookian springs.	44
2.6	The Γ_1 system of springs can be reduced to the Γ_0 system with related spring constants.	45
2.7	The approximating sequence $\Gamma_0, \Gamma_1, \Gamma_2$ and a random iteration procedure converging to Hata's tree-like set. Here we have taken $c = 0.4 + 0.3\sqrt{-1}$	47
3.1	The nodes considered for the decimation procedure.	53
3.2	The three eigenfunctions of $-\mathcal{H}_2^0$ with eigenvalue $\lambda = 6$	56
3.3	An eigenfunction on Γ_3 with eigenvalue $\lambda = 6$ that is constructed from an eigenfunction on Γ_2 , also with eigenvalue $\lambda = 6$	57
3.4	The three remaining eigenfunctions of $-\mathcal{H}_3^0$ with eigenvalue $\lambda = 6$. . .	58
3.5	The three eigenfunctions of $-\mathcal{H}_2^0$ with eigenvalue $\lambda = 5$	58

3.6	The eigenfunction $v_{5,1}^3$	59
3.7	The Decimation method used to calculate the eigenvalues (and multiplicities) of $-\mathcal{H}_m^0$	60
3.8	The Spectrum of \mathcal{H}_6^0	61
3.9	The eigenfunction of $-\mathcal{H}_6^0$ with eigenvalue $\lambda = (\phi_-(2))^6$	62
3.10	An eigenfunction of $-\mathcal{H}_6^0$ with eigenvalue $\lambda = (\phi_-(5))^5$	62
3.11	The Decimation method used to calculate the eigenvalues (and multiplicities) of $-\mathcal{H}_m$	64
3.12	The Spectrum of $-\mathcal{H}_6$	64
3.13	An eigenfunction of $-\mathcal{H}_6$ with eigenvalue $\lambda = (\phi_-(\phi_+(6)))^3$	65
3.14	An eigenfunction of $-\mathcal{H}_6$ with eigenvalue $\lambda = (\phi_-(\phi_+(6))^2))^3$	66
3.15	The difference between the spectra of \mathcal{H}_m and \mathcal{H}_m^N , for $m = 4, 5, 6$	69
3.16	The second order approximation to the double of SG.	70
3.17	The extension of a pre-localised eigenfunction on Γ_5 to Γ_6 under the map f_3	72
4.1	This figure shows three segments of our neuronal cable, length Δx , radius a , along with the currents we shall be considering.	76
4.2	The equivalent electrical circuit to Figure 4.1.	78
4.3	The solution of the discrete cable equation (4.20) on Γ_6 with Dirichlet boundary conditions.	85
4.4	The average voltage of the neighbours of the boundary point P_2 obtained by solving the cable equation with Dirichlet boundary conditions, subject to an initial stimulus, amplitude 1, at the neighbours of the boundary point P_1	86
4.5	A log plot of the the average voltage of the neighbours of the boundary point P_1 against time.	87
4.6	Here, the input is scaled by a factor of $(\frac{25}{3})^m$, and we see that the output is now independent of the level of approximation of the gasket	88

4.7	The solution of the discrete cable equation (4.20) on Γ_6 with Neumann boundary conditions.	90
4.8	The voltage at the boundary point P_2 obtained by solving the cable equation with Neumann boundary conditions, subject to an initial stimulus, amplitude 1, at the boundary point P_1	91
4.9	The voltage at the boundary point P_2 obtained by solving the cable equation with Neumann boundary conditions, subject to an initial stimulus, amplitude 3^k , at the boundary point P_1	92
5.1	A typical phase portrait for the system (5.9).	99
5.2	The nullclines of the modified FHN system. The red curves show $\frac{dX}{dt} = 0$ and the blue curves show $\frac{dY}{dt} = 0$	102
5.3	The potential, u , plotted for a planar wave initiated by putting u above the threshold at the left edge of the domain. A movie of this figure can be found on the accompanying CD, named FHNMov1.avi.	105
5.4	The position of a planar wave for discrete times.	106
5.5	The position of the wavefront as a function of time.	106
5.6	Schematic diagram showing the form of u and v in the travelling frame.	107
5.7	Phase portraits of the system (5.26) for different values of c	111
5.8	The propagation of a target wave resulting from a stimulus applied to the centre of the domain. A movie of this figure can be found on the accompanying CD, named FHNMov2.avi.	113
5.9	The potential, u , plotted for a planar wave, resulting from setting $u = 1$ along the edge between the boundary points P_1 and P_3 . A movie of this figure can be found on the accompanying CD, named FHNMov3.avi.	115
5.10	The propagation of a planar wave, resulting from setting $u = 1$ at the boundary point P_3 and its two neighbours. A movie of this figure can be found on the accompanying CD, named FHNMov4.avi.	115
5.11	The wave profiles of a planar wave propagating across Γ_7^6	116

5.12	The nodal position of the wavefront (blue) and a linear least squares approximation (red) plotted as a function of time.	117
5.13	The normalised wave speed as a function of the level of approximation, m for a wave propagating from a corner to an edge (blue) and from an edge to a corner (red).	119
5.14	The potential, u , plotted for a rotating spiral wave. The initial condition in this case is a broken planar wave. A movie of this figure can be found on the accompanying CD, named FHNMov5.avi.	122
5.15	The potential, u , plotted for a skewed spiral wave. The initial condition in this case is a broken planar wave.	122
5.16	The potential, u , plotted for the break-up of a spiral wave. The initial condition in this case is a broken planar wave. A movie of this figure can be found on the accompanying CD, named FHNMov6.avi.	124
5.17	Mean values of the time series $B_{(10)}$ (squares), and the mean values of the time series $B_{(100)}$ (dots), as functions of ε^{-1}	126
5.18	The potential, u , plotted for the analogue of a spiral wave. The times shown are after the truncation of a planar wave, propagating for 5 time units. A movie of this figure can be found on the accompanying CD, named FHNMov7.avi.	128
5.19	The position of the planar wave at $t = 4.5$	129
5.20	The potential, u , plotted for the analogue of a spiral wave. The times shown are after the truncation of a planar wave, propagating for 4.5 time units. A movie of this figure can be found on the accompanying CD, named FHNMov8.avi.	130
5.21	The potential, u , plotted for the analogue of a spiral wave. The times shown are after the truncation of a planar wave, propagating for 5 time units. A movie of this figure can be found on the accompanying CD, named FHNMov9.avi.	133

5.22	The location of the nodes we are interested in, a, b, c and d	134
5.23	The phase space for $t = 0$ to $t = 4$ for the nodes a and b . In the left had column the planar wave has been truncated at $t = 4.5$. In the right hand column the planar wave has been truncated at $t = 5$	135
5.24	The phase space for $t = 0$ to $t = 4$ for the nodes c and d . In the left had column the planar wave has been truncated at $t = 4.5$. In the right hand column the planar wave has been truncated at $t = 5$	135
5.25	The u (blue) and v (red) values plotted against time for the nodes a and b . In the left had column the planar wave has been truncated at $t = 4.5$. In the right hand column the planar wave has been truncated at $t = 5$	136
5.26	The u (blue) and v (red) values plotted against time for the nodes c and d . In the left had column the planar wave has been truncated at $t = 4.5$. In the right hand column the planar wave has been truncated at $t = 5$	136
5.27	A comparison between actual phase trajectories (with diffusion) and the vector field of the diffusionless FHN system.	138
5.28	The relationship between the state of node c and the recovery variable on node d	139
5.29	The initial condition here is a plane wave reset to $K_1 = 0$ after propagating until $t = 5$. $\varepsilon^{-1} = 12.5$. A movie of this figure can be found on the accompanying CD, named FHNMov10.avi.	140
5.30	The left hand plot shows the state of node q_1 and the right hand plot shows this state in relation to the value of the recovery variable at node n	141
5.31	The initial condition here is a plane wave reset to $K_1 = 0$ and $K_{31} = 0$ after propagating until $t = 4.5$. $\varepsilon^{-1} = 12.5$	142

- 5.32 The initial condition here is a plane wave reset to $K_1 = 0$ and $K_{31} = 0$ after propagating until $t = 4.5$. $\varepsilon^{-1} = 12$. A movie of this figure can be found on the accompanying CD, named FHNMov11.avi. 143

Abstract

In this thesis we study non-linear dynamical systems on complex domains. Although the systems we consider are mathematical abstractions, our motivation is to gain insights into neurobiological systems. The mathematical techniques we employ concern analysis on a particular class of fractal sets. This theory allows one to construct a Laplacian and to study the spectrum and eigenfunctions given a variety of boundary conditions. This thesis uses these results to define and study the cable equation and the FitzHugh-Nagumo system on the Sierpinski Gasket.

Declaration

No portion of the work referred to in this thesis has been submitted in support of an application for another degree or qualification of this or any other university or other institute of learning.

Copyright Statement

Copyright in text of this thesis rests with the author. Copies (by any process) either in full, or of extracts, may be made **only** in accordance with instructions given by the author and lodged in the John Rylands University Library of Manchester. Details may be obtained from the librarian. This page must form part of any such copies made. Further copies (by any process) of copies made in accordance with such instructions may not be made without the permission (in writing) of the author.

The ownership of any intellectual property rights which may be described in this thesis is vested in The University of Manchester, subject to any prior agreement to the contrary, and may not be made available for use by third parties without the written permission of the University, which will prescribe the terms and conditions of any such agreement.

Further information on the conditions under which disclosures and exploitation may take place is available from the Head of School of Mathematics.

Acknowledgements

Firstly I would like to express thanks to my supervisor, Professor David Broomhead. Dave has supported and encouraged me with his natural enthusiasm throughout my studies.

A huge thanks goes to my parents for their unwavering emotional and financial support, and also to my sisters for being there for me through times of stress.

I am grateful to all the friends I have made at UMIST and The University of Manchester over the last nine thoroughly enjoyable years. In particular, I thank the postgraduate students in the School of Mathematics. Their companionship and conversation on all the fun Fridays in Harry's bar has inspired me (in spite of the headaches!).

I also wish to thank Dr. Manuchehr Soleimani, who introduced me to the delights of Matlab and Rob Livesey, for helping me with all the technical problems I have encountered.

Finally, I thank Samina Ali and Marianne Johnson for all their friendship, help and support.

Chapter 1

Introduction

Before the 20th century, mathematical intuition was bound up with ideas of continuity and smoothness. The development of calculus in the 17th century was built on this intuition and proved to be so spectacularly successful that in many of the applied sciences differentiability almost took the role of an axiom. However, by the early 20th century, many examples of objects or functions with peculiar properties had been created. In 1872 Karl Weierstraß found a function that is continuous everywhere yet nowhere differentiable. In 1904 Helge von Koch gave a geometric definition of a similar function: his famous Koch curve (see Figure 1.2).

By far the most important (although not the most visually appealing) of these non-classical sets is an uncountable subset of the unit interval (in fact there is a bijection between it and the unit interval) which has zero Lebesgue measure. This set was first described by Cantor in 1883. The Cantor set is constructed from the unit interval by removing a sequence of open intervals. Let E_0 be the interval $[0, 1]$, the set E_1 is obtained by removing the open middle third of E_0 so $E_1 = [0, \frac{1}{3}] \cup [\frac{2}{3}, 1]$. Removing the middle third of each of these two intervals produces E_2 and so on. The set E_k thus consists of 2^k intervals of length 3^{-k} . The Cantor set can then be thought of as the limit of the sets E_k as $k \rightarrow \infty$. In the late 19th and early 20th centuries mathematicians such as Poincaré, Klein, Fatou and Julia had investigated

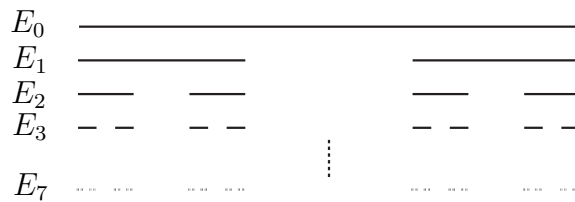


Figure 1.1: The approximating sequence E_0, E_1, E_2, E_3 and E_7 to the Cantor Set.

iterated functions of the complex plane and found several examples of such complex sets. However, without the aid of computer graphics, they were unable to see the beauty of the objects they had created.

For a long time the irregular sets described here were often disregarded as pathological counterexamples and certainly were not thought of as a class of objects on which a general theory could be developed. The change in this point of view is due to the mathematician Benoît Mandelbrot. While working for IBM in the early 1960s he worked on an astonishing number of seemingly unrelated problems: noise on telephone lines, game theory, linguistics, economy and turbulence to name just a few. In 1962 Mandelbrot became interested in a problem related to the fluctuation of prices on the stock exchange. Classical theories dictated that short term fluctuations were largely random whereas long term fluctuations reflected the fundamental laws of economy. Mandelbrot discovered that the sequence of price changes was independent of scale: there was no statistical difference between the short term and long term fluctuations. On the basis of this, Mandelbrot was able to develop a mathematical model that could simulate very realistic stock exchange price fluctuations.

Soon afterwards, Mandelbrot concerned himself with the problem of noise in telecommunications lines at IBM. All such lines are subject to random fluctuations and if this noise fluctuates above a certain threshold, some information can be lost, creating an error. The engineers at IBM noticed that the errors seemed to arrive in clusters, separated by quiet intervals of variable length. Upon further inspection of a batch of errors, it was noticed that these too are made up of smaller batches also

separated by quiet periods without error and so on. Mandelbrot discovered that at every timescale, the relationship of errors to clean transmission remained constant. Again, therefore, he had found scale invariance in a seemingly unrelated physical phenomenon.

Mandelbrot turned to other data from geophysical origins and in 1968 he published a paper discussing the length of the coastline of Britain [51]. The paper discusses the research published by Lewis Fry Richardson [3] on how the measured lengths of coastlines are dependent on the scale of measurement. Mandelbrot was finding the same notion running through his research into so many diverse and unrelated areas: self-similarity.

A self-similar object is one that contains copies of itself at different levels of magnification. These copies may be exact versions of the original object or an approximate or distorted version. Exact self-similarity is seen predominately in mathematical objects constructed by deterministic methods, such as the Cantor set. Many natural phenomena exhibit approximate self-similarity, whereby as the object is observed at different scales one sees structures that are recognisably similar but not identically so. For example, the leaf of a fern looks similar to the original fern. Sometimes self-similarity is not visually obvious, however there may be certain properties that are preserved across scales. This property is known as statistical self-similarity.

Mandelbrot claimed that many real world phenomena are not collections of smooth Euclidean shapes and are much better represented by irregular self-similar objects. Mandelbrot brought these objects together for the first time and coined the term “Fractals” from the Latin *fractus* meaning “fragmented and irregular” as a name for them [52, 53]. Mandelbrot pioneered the use of fractals to model a wide variety of scientific phenomena including the shapes of mountains, clouds and coastlines; the structure of plants, blood vessels and lungs; galaxy clusters. A new area of mathematics – Fractal Geometry – became a part of applied mathematics.

Much of the work that has been carried out in Fractal Geometry has been con-

cerned with computing certain quantities which can be used to characterise fractals, the most important being that of dimension. We are all happy with the notion that a point has (Euclidean) dimension zero, a line is 1-dimensional, a plane 2-dimensional and so on, but what about the dimension of fractal objects? Fractal dimension is a quantity that gives us an indication of how completely a fractal appears to fill space as one observes the object on finer and finer scales. There have been many suggestions given as to what is a suitable definition of fractal dimension, the most important of which being the Hausdorff dimension, see, for example [17] (sometimes referred to as the Hausdorff-Besicovitch dimension). This fundamental idea was proposed by Hausdorff (1919) and subsequently developed by Besicovitch (1935).

The Hausdorff dimension of a set $F \subset \mathbb{R}^n$ is calculated by considering the number of sets $U \subset \mathbb{R}^n$, whose diameter is at most δ , required to cover F . If $\{U_i\}$ is a countable collection of sets with $\text{diam}(U_i) \leq \delta \forall i$ that cover F , then we call $\{U_i\}$ a δ -cover of F . Now for any $s \geq 0$ and any $\delta > 0$ we define

$$\mathcal{H}_\delta^s(F) = \inf \left\{ \sum_{i=1}^{\infty} |U_i|^s : \{U_i\} \text{ is a } \delta\text{-cover of } F \right\}, \quad (1.1)$$

where $|U_i|$ is the diameter of the set U_i . We then define the s -dimensional Hausdorff measure of a set $F \subset \mathbb{R}^n$ to be

$$\mathcal{H}^s(F) = \lim_{\delta \rightarrow 0} \mathcal{H}_\delta^s(F). \quad (1.2)$$

This limit exists for any $F \subset \mathbb{R}^n$, although as δ decreases, the infimum in equation (1.1) increases so the limiting value may be ∞ . For any F , $\mathcal{H}^s(F)$ is non-increasing as s increases from 0 to ∞ . In fact, if $s < t$ we have

$$\mathcal{H}_\delta^t(F) \leq \delta^{t-s} \mathcal{H}_\delta^s(F), \quad (1.3)$$

which implies that (letting $\delta \rightarrow 0$) if $\mathcal{H}^s(F) < \infty$ then $\mathcal{H}^t(F) = 0$. There exists a critical value of s , $\dim_H F$ such that

$$\begin{aligned} \mathcal{H}^s(F) &= \infty & s < \dim_H F, \\ \mathcal{H}^s(F) &= 0 & s > \dim_H F. \end{aligned} \quad (1.4)$$

This critical value of s , $\dim_H F$ is called the *Hausdorff dimension of F* .

The Hausdorff has the following desirable properties:

Open Sets: If F is an open subset of \mathbb{R}^n , then $\dim_H F = n$.

Smooth Sets: If F is a smooth m -dimensional manifold, then $\dim_H F = m$.

Monotonicity: If $E \subset F$, then $\dim_H E \leq \dim_H F$.

Countable Stability: $\dim_H \left(\bigcup_{i=1}^{\infty} F_i \right) = \sup_{1 \leq i \leq \infty} \dim_H F_i$.

Countable Sets: If F is finite or countable, then $\dim_H F = 0$.

Although the Hausdorff dimension is technically the best definition of a fractal dimension, it has the disadvantage of being difficult to compute. There are, however, different definitions of fractal dimensions that are easy to calculate. One of the most widely-used is the box counting dimension, \dim_B . The box counting dimension of a non-empty set, $F \subset \mathbb{R}^n$ is given by

$$\dim_B F = \lim_{\delta \rightarrow \infty} \frac{\log N_\delta(F)}{-\log \delta}, \quad (1.5)$$

where $N_\delta(F)$ is the smallest number of sets of diameter at most δ which cover F . The box counting dimension shares many properties with the Hausdorff dimension although there are some disadvantages. For example, countable sets can have non-zero box counting dimension.

Now we introduce the notion of the similarity dimension of a set F , $\dim_S F$. This is only meaningful for a small class of fractals, however it is easy to compute and for strictly self-similar objects, the value of \dim_S agrees with that of \dim_H and \dim_B . It is worth noting here that all fractal objects exhibit self-similarity, yet not all self-similar objects are fractals. The simplest example of a self-similar set is that of a line. We may break this into two self-similar intervals each looking exactly like our original line that may be magnified by a factor of two to yield our original line. In general, we can break a line segment into N self-similar pieces each scaled by a factor

of $\frac{1}{N}$. Similarly a square and a cube may be decomposed into N^2 and N^3 self-similar copies respectively, each scaled by $\frac{1}{N}$. We see that in all these cases there is a nice power law relation between the number of pieces the object is broken into, N , and the scaling factor, S . If F is a line segment, or a square, or a cube etc. then

$$N = \frac{1}{S^{\dim_S F}}, \quad (1.6)$$

where $\dim_S F = 1, 2, 3$ for the line, square and cube respectively. Equivalently we have

$$\dim_S F = \frac{\log N}{\log \frac{1}{S}}, \quad (1.7)$$

and we see that in the case of the line, the square and the cube the value of the similarity dimension $\dim_S F$ agrees with the Euclidean dimension.

Now, we shall calculate \dim_S for a fractal set. We consider the Koch curve which is constructed iteratively as follows. Begin with a straight line of unit length, E_0 . To produce E_1 remove the middle third of E_0 and replace it with two sides of an equilateral triangle that each have the same length as the remaining lines on each side. We now repeat this procedure, taking each of the resulting straight line segments, removing the middle third and so on, see Figure 1.2. The self-similarity of the Koch curve is immediately apparent. We see that the whole curve comprises four copies of the original, each one third the size. From (1.7) the similarity dimension of the Koch curve (KC) is therefore

$$\dim_S KC = \frac{\log 4}{\log 3} \approx 1.2619. \quad (1.8)$$

A similar calculation can be made on the Cantor set (CS) to give

$$\dim_S CS = \frac{\log 2}{\log 3} \approx 0.6309. \quad (1.9)$$

From a mathematical point of view, a fractal is defined to be an object whose similarity dimension exceeds its topological dimension.

In recent years it has been realised that many physiological and biological systems have no characteristic length or time scale, i.e. they have fractal properties. As an

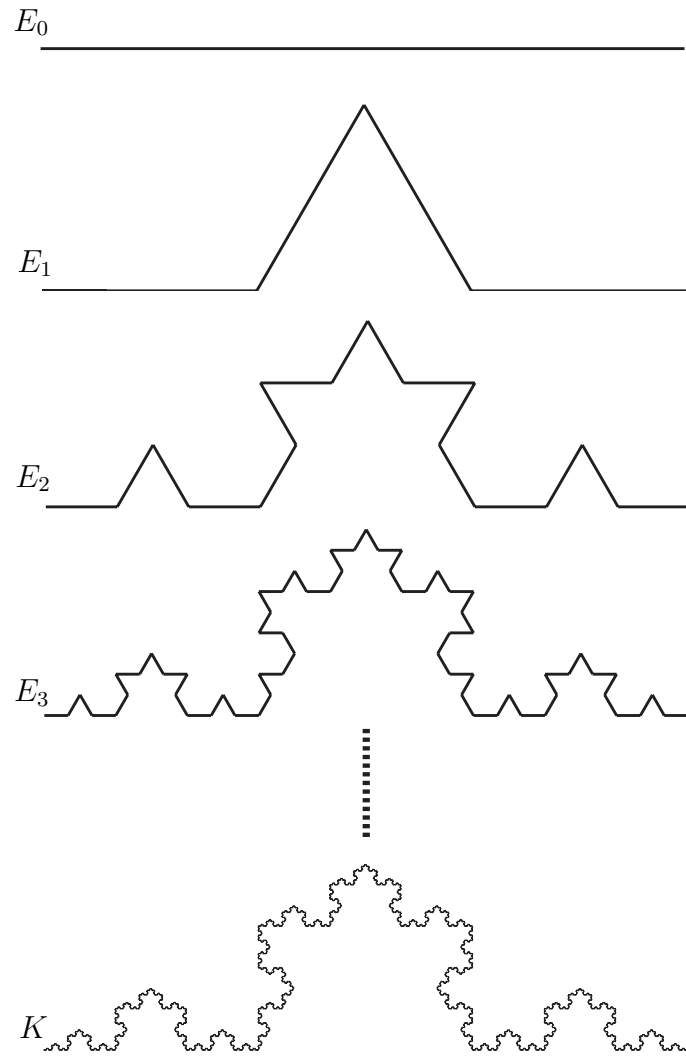


Figure 1.2: The approximating sequence E_0 , E_1 , E_2 , E_3 and the Koch Curve.

example, consider the behaviour of the heart. The human heart's natural healthy rhythm is described as the "regular sinus rhythm". In fact, it is anything but "regular". The intervals between consecutive heartbeats normally fluctuate in a complex, apparently erratic manner, even in individuals at rest [37]. An ECG showing the meanderings of heart rate over a thirty minute period looks roughly the same as a graph that covers just three minutes – the heartbeat is self-similar. Interestingly, this randomness is an indication of a healthy heart: diseased hearts show more regular heartbeats [28].

Another physiological structure that is known to behave in a fractal manner is the neuron or nerve cell. The neuron responds to stimuli applied to its dendrites by opening and closing ion channels in its axon. This causes an electrical signal to propagate down the axon, which can, in turn, stimulate the dendrites of impinging neurons. Fundamentally, a neuron is a threshold device: if the stimulus is large enough, the neuron responds, if not, it does not. Thus, the output of a neuron is a discrete spike-train, which can be measured as a time series. In [23], it was shown that the interspike interval of some neurons in the auditory cortex of the cat was essentially independent of the resolution of the timescale.

In this thesis, we shall be mainly concerned with naturally-occurring objects whose structure is fractal. A particular characteristic of fractal objects is the very large surface to area (or volume) ratio. In many biological situations surface area is of crucial importance and all the distributive systems of the human body – cardiovascular, respiratory, lymphatic, digestive and excretory – display fractal characteristics. As an example, consider the structure of the lung, which is a branching structure. The trachea (or windpipe) branches into two bronchi, which in turn branch into smaller and smaller bronchioles eventually ending at the alveoli where the exchange of oxygen and carbon dioxide takes place. In order to maximise efficiency, the surface area of the lung must be as large as possible. In fact, the surface area of a human lung is as large as a tennis court. The structure of the bronchial tree has been analysed using

fractal techniques [72, 66] and it has been shown that the average dimensions of the bronchial tubes decays according to a power law rather than exponentially as had previously been thought.

Another example of fractals occurring in nature is the structure of certain types of fungi and bacteria. An example of this are the soil bacteria *streptomyces* that produce many different kinds of antibiotics. The life-cycle of the *streptomyces* is complex: initially the bacterium consists of a single free spore. The spore germinates growing long, branching filaments known as hyphae. A typical hypha consists of a tubular wall which surrounds, supports and protects the cells that compose the hypha. Hyphae do not grow through cell division as animal, plant or yeast cells, but by extending their cells. When a single cell has become a longer tube, a wall called a septum grows to produce two separate cells, the second having a nucleus copied from the first. This process of elongation and separation repeats producing a network of hyphae known as the mycelium. The unusual growth process of the hyphae leads to the mycelium having a geometrically complex structure.

An approach to quantifying the branching of the mycelia relies on fractal geometry. Obert *et al* [57] have applied fractal techniques to calculate the box counting dimension of mycelial structures. This can be used to quantify the extent to which the mycelia permeate the space in which they grow. Obert *et al* analysed photographs of various mycelia: that is, they studied planar projections of objects that grow in two- or three-dimensional space.

The structure of a young mycelium was found to be a mass fractal, where the interior contains gaps and so the whole of the object is treated as a fractal. As the mycelium develops, the hyphae grow and gradually fill the interior. Now the mycelium is treated as a surface fractal, where only the boundary of the object is fractal. To distinguish between these two different types of fractal structure, two different box counting methods were applied. The box mass dimension of the mycelium (M), $\dim_{BM}M$, considers the whole mass of the mycelium, whereas the box surface

dimension, $\dim_{BS}M$, just considers the boundary.

In the case where the mycelial structure is a mass fractal, the two methods give $\dim_{BM}M = \dim_{BS}M$. For a surface fractal, $\dim_{BS}M$ describes the surface irregularities, whereas $\dim_{BM}M$ gives the dimension of the embedding space ($d = 2$ in this case). The fractal dimension is then defined to be the value of $\dim_{BS}M$ in both cases. Obert *et al* showed that fractal geometry is a suitable technique to describe some biological growth patterns and that the fractal dimension of the mycelium increases during growth up to a value of 1.5.

Many other biological objects display fractal properties, including the patterns of blood vessels, DNA sequences and, as we shall now discuss, the branching structure of the dendritic tree of neurons. Not only does the neuronal spiking pattern follow fractal behaviour, as we have seen, but the structure of dendritic tree is geometrically complicated and self-similar. This is another example of how the body uses fractal structures to be as efficient as possible: the small nerve fibres and massive surface area means the greatest number of neurons can be packed into the brain and each nerve cell can connect with as many neurons as possible. It is in this context that much of this thesis will be concerned.

We have seen how many natural objects are well-described by fractals, so the question we wish to ask is “How can we model the dynamical processes that occur on them?” For example, the air flow in the respiratory system, the blood flow in the cardiovascular system, the transportation of moisture and nutrients in the mycelium of the streptomyces and the conduction of an action potential in neurons are all examples of natural processes on a fractal structure. We are therefore interested in modelling dynamical processes on fractal sets with a view to understanding how the complexity of the structure affects well-known processes such as reaction and diffusion.

The basic question is “what is the analogue of diffusion on such objects?” We begin with the problem of how to define a “Laplacian” on an object that is not

smooth enough to define differential operators on from a classical viewpoint. This problem was first tackled by physicists in the 1970s, when it was suggested that fractals may represent the geometrical features of percolation clusters. This led to the calculation of the spectral dimensionality and other physical characteristics of fractals. The spectral dimension, d_s is an exponent describing the scaling of the density of states with the energy on a fractal.

The fractal most commonly considered is the Sierpinski Gasket (SG). This is constructed from an equilateral triangle, subdividing it into four smaller triangles and removing the open central triangle. Repeating this process to infinity we arrive at the Sierpinski Gasket. The first progress from a mathematical point of view came when Kusuoka, [50], and Goldstein, [26], independently constructed Brownian motion on the Sierpinski Gasket by considering a sequence of random walks on the graphs that approximate SG. Under a certain scaling these random walks converge to a diffusion process on SG.

In 1989 Jun Kigami proposed a direct definition of a Laplacian on the Sierpinski Gasket [43]. This so-called analytical approach considers a sequence of graphs approximating SG and the Laplacian on the Sierpinski Gasket is then the renormalised limit of the graph Laplacians. This approach gives rise to a natural and direct definition of a Laplacian on the Sierpinski Gasket using Dirichlet forms. It is also possible to describe harmonic functions, Green's functions and solutions of Poisson's equations. Later this approach was extended to define Laplacians on a class of fractals called post-critically finite (p.c.f.) self-similar sets [44]. With the definition of a Laplacian now in place it is possible to study dynamical processes involving diffusion on objects that can be approximated by p.c.f. fractals. The book [48] gives a detailed description of the approach and progress made so far in the area of Analysis on Fractals. In this thesis we shall mainly be considering the case of the Sierpinski Gasket and looking whether the complex geometry has any consequences in the dynamics of these processes. With a definition of a Laplacian on SG in place we can solve numerically

differential equations involving second order spatial derivatives.

This thesis is organised as follows. In Chapter 2 we begin by discussing the theory of iterated function systems, which are often used to generate self-similar sets deterministically. We introduce the Sierpinski Gasket and use this as an example throughout the chapter to illustrate the theory. Following the approach of Kigami we discuss the geometry of self-similar sets and introduce the notion of a self-similar structure to give a topological definition of self-similar sets. We then give a definition of what is meant by a post-critically finite (p.c.f.) self-similar set: the class of self-similar set on which the theory has been developed. We then go on to describe harmonic functions and their properties on p.c.f. self-similar sets and give a pointwise definition for the Laplacian on the Sierpinski Gasket, which is the rescaled limit of the Laplacians on the graph approximations to SG. Finally, we consider another p.c.f. self-similar set called Hata's tree-like set, which geometrically resembles the dendritic tree of a neuron and show that the methods applied for SG do not give such nice results in the case of Hata's tree-like set.

In Chapter 3 we consider the eigenvalues and eigenfunctions of the m -harmonic difference operators on the graph approximations to SG (The Laplacian on SG is simply the renormalised limit of the harmonic difference operators as $m \rightarrow \infty$). We consider two cases: Dirichlet boundary conditions and Neumann boundary conditions. In both cases the spectrum can be completely determined: the eigenvalues of the level m approximation to SG can be related to those on the level $m - 1$ approximation by a decimation procedure and the eigenfunctions can be computed via a local extension algorithm. In the Neumann case we find that in order for us to be able to apply the decimation method, we must sacrifice the orthogonality of the Laplacian eigenfunctions. A way around this problem is to introduce the notion of a fractafold called the double of the Sierpinski Gasket. Finally we talk about the existence of localised eigenfunctions of the Laplacian on the Sierpinski Gasket.

In Chapters 4 and 5 we shall be considering two mathematical models describing

physiological phenomena. The first model is the linear cable equation, which describes the passive propagation of electrical signals in nerve cells. Secondly we shall consider the FitzHugh-Nagumo system, which is a more sophisticated reaction-diffusion system accounting for the excitable nature of nerve cells or cells in cardiac tissue. In both of these cases, we look for those properties which owe their origin to the fractal nature of the domain. Finally, in Chapter 6, we summarise the results of this research and provide some concluding remarks.

Chapter 2

Fractals and Laplacians

2.1 Iterated Function Systems and Self-Similar Sets

Many self-similar sets can be generated by a class of mathematical systems which combine notions of randomness and determinism in an interesting way. These systems were first studied by Hutchinson in 1981 [36] and were later given the name *iterated function system* (IFS) by Barnsley [8]. Currently the most complete theory of IFSs concerns transformations of a complete metric space, (X, d) , which are in some sense contractive. The basic theory begins with the following definition:

Definition 2.1. *A hyperbolic iterated function system consists of a complete metric space (X, d) and a finite set of contraction mappings $\{f_i\}_{i=1}^N$ with respective contractivity factors s_i , $0 < s_i < 1$, $i = 1, 2, \dots, N$. The contractivity factor for the IFS is then $s = \max\{s_1, \dots, s_N\}$.*

Weaker ideas of contractivity can be employed, for example contractions-on-average [15], but for the purposes of this thesis we shall deal entirely with hyperbolic IFSs. We can think of self-similar sets as closed and bounded subsets of the set X , so we introduce the associated space of non-empty, compact subsets of X , $\mathcal{H}(X)$. This set, when endowed with the Hausdorff metric h forms a complete metric space. Consider

an IFS $\{f_i\}_{i=1}^N$ acting on (X, d) , we define the map $F : \mathcal{H}(X) \rightarrow \mathcal{H}(X)$ by

$$F(A) = \bigcup_{i=1}^N f_i(A) \quad \forall A \in \mathcal{H}(X). \quad (2.1)$$

The following theorem establishes the existence of a unique attractor for the IFS and suggests how to compute such a set.

Theorem 2.2. *Let $\{f_i\}_{i=1}^N$ be an IFS on the complete metric space (X, d) with contractivity factor s . Then the map F defined in (2.1) is a contraction mapping on $(\mathcal{H}(X), h)$ with contractivity factor s . It then follows from the Contraction Mapping Theorem that F has a unique fixed point, $K \in \mathcal{H}(X)$, satisfying*

$$K = F(K) = \bigcup_{i=1}^N f_i(K) \quad (2.2)$$

and is given by

$$K = \lim_{i \rightarrow \infty} F^i(U) \quad (2.3)$$

for any $U \in \mathcal{H}(X)$. K is called a self-similar set with respect to the IFS $\{f_i\}_{i=1}^N$.

As an example of Theorem 2.2 consider the following collection of maps of the plane:

$$f_i(\mathbf{x}) = \begin{pmatrix} 0.5 & 0 \\ 0 & 0.5 \end{pmatrix} \mathbf{x} + b_i, \quad i = 1, 2, 3, \quad (2.4)$$

where $\mathbf{x} \in \mathbb{R}^2$, $b_1 = (0, 0)^T$, $b_2 = (\frac{1}{2}, 0)^T$, $b_3 = (\frac{1}{4}, \frac{\sqrt{3}}{2})^T$. The unique fixed point of this IFS satisfying $K = f_1(K) \cup f_2(K) \cup f_3(K)$ is the famous Sierpinski Gasket (SG). In Figure 2.1 we illustrate the convergence implied by Theorem 2.2 for the case of two compact sets. The figure shows a sequence of images of a circle (which could be interpreted as the circle or the closed disc) and of a square (with similar choice of interpretation) under repeated action of the map F .

In this thesis we are concerned with the construction of differential operators, in particular a Laplacian operator, on a certain class of self similar sets. We use the Sierpinski Gasket as an example to illustrate the approach. For this purpose the

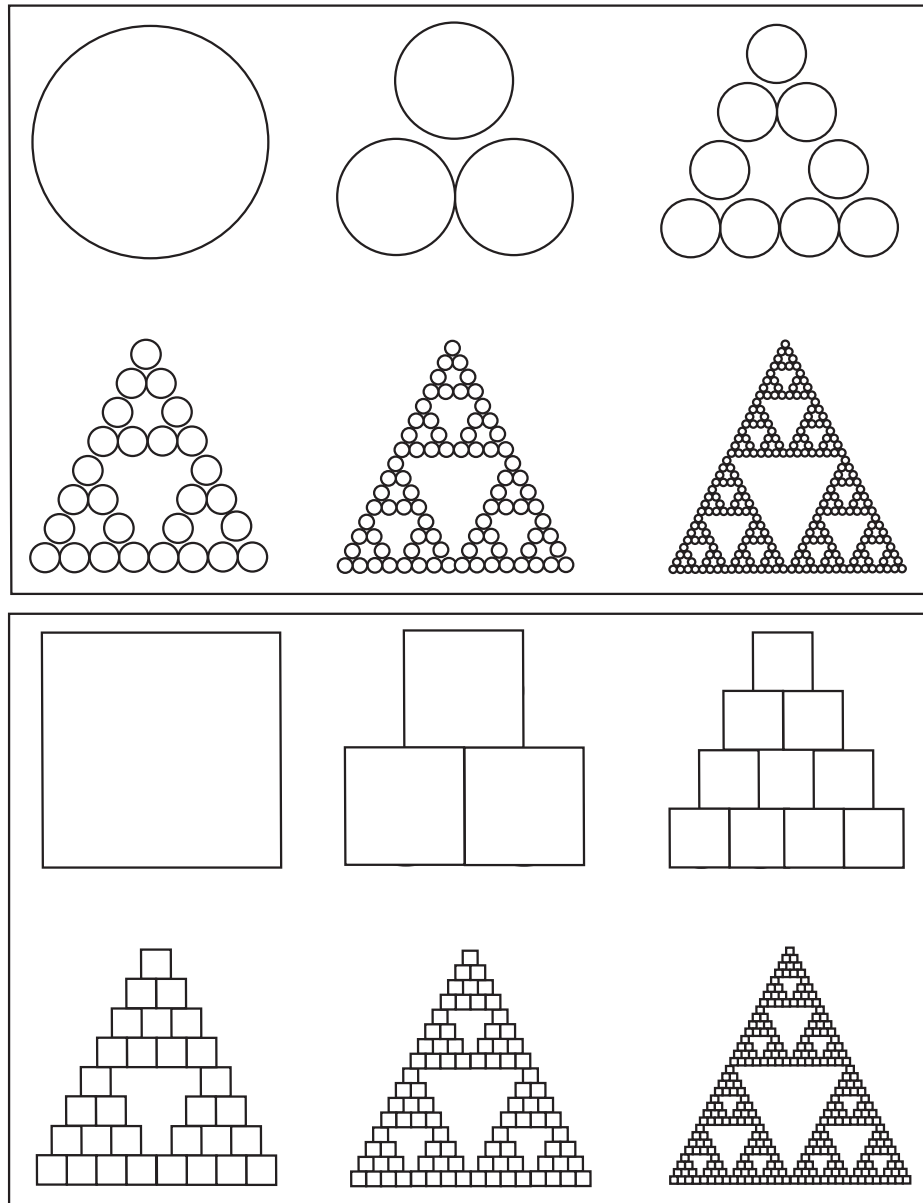


Figure 2.1: Generating the Sierpinski Gasket when the initial set is (a) a circle, and (b) a square.

Sierpinski Gasket is approximated by a sequence of graphs. We use standard graph notation: the level m graph approximation to the Sierpinski Gasket consists of a set of vertices (or nodes), V_m , and a set of edges, E_m , and is denoted by $\Gamma_m = \{V_m, E_m\}$, see Figure 2.2. We begin our graph sequence with the zero level approximation to the Sierpinski Gasket, Γ_0 , which consists of the nodes $V_0 = \{P_1, P_2, P_3\}$, the three vertices of an equilateral triangle¹ and the edges between them. Subsequent sets of vertices are then obtained inductively by

$$V_{m+1} = \bigcup_{i=1}^3 f_i(V_m). \quad (2.5)$$

Clearly by Theorem 2.2 the set of vertices alone will converge to SG as $m \rightarrow \infty$. However, since we shall use the analogue of finite difference methods to approximate derivatives on self similar sets, we require a notion of adjacency. We therefore specify that adjacent vertices are joined by an edge. We can think of the set of edges as a subset of the set of all ordered pairs of vertices $V_m \times V_m$. For two vertices $V_m^i, V_m^j \in V_m$, we have

$$(V_m^i, V_m^j) \in E_m \iff (f_k(V_m^i), f_k(V_m^j)) \in E_{m+1} \text{ for } k = 1, 2, 3.$$

That is: vertices in V_{m+1} are joined by an edge if and only if their preimages in V_m under any of the contractions f_i are joined by an edge. With this in mind, we shall use the following notation to denote that two vertices on the graph Γ_m are joined by an edge: $x \underset{m}{\sim} y$, and we say vertices x and y are *neighbours* on Γ_m . The set V_0 is referred to as the boundary of SG. We note that V_m and E_m contain $\frac{3}{2}(3^m + 1)$ and 3^{m+1} elements respectively and that $\lim_{m \rightarrow \infty} V_m = K$. We shall adopt the following notation: the graph Γ_m comprises 3^m order- m (or *minimal*) triangles and we refer to the vertices that are common to neighbouring order- m triangles as (order- m) junction points.

¹Actually, P_1, P_2, P_3 can be chosen to be any three non-colinear points in the plane without altering the theory.

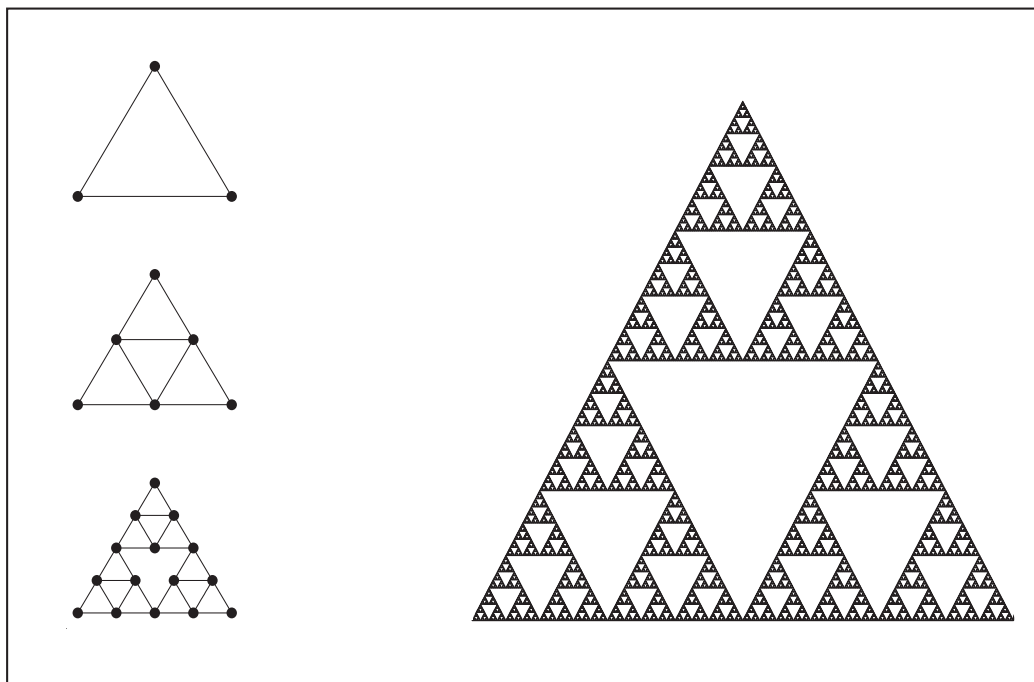


Figure 2.2: The approximating sequence $\Gamma_0, \Gamma_1, \Gamma_2$ and the Sierpinski Gasket.

The set of vertices V_m becomes dense in the Sierpinski Gasket in the sense that for any point x in K and any $\varepsilon > 0$ we can choose some suitably large m such that the ε -neighbourhood of x contains a point in V_m . Continuous functions on the Sierpinski Gasket are then uniquely determined by their restrictions to the V_m .

Consider the structure of a self-similar set K ; it is clear that K satisfies

$$K = \bigcup_{i=1}^N f_i(K) = \bigcup_{i=1}^N f_i \left(\bigcup_{j=1}^N f_j(K) \right) = \bigcup_{i=1}^N \bigcup_{j=1}^N f_i \circ f_j(K). \quad (2.6)$$

Since maps of the IFS $\{f_i\}_{i=1}^N$ are contracting, continuous maps, we have a decreasing nested sequence of compact sets:

$$K \supset f_i(K) \supset f_i \circ f_j(K) \supset \dots \quad i, j = 1, 2, \dots, N, \quad (2.7)$$

and the limit of such is non-empty. In fact, the limit of this sequence is a single point, the coordinates of which depend on the particular sequence of maps applied. We can

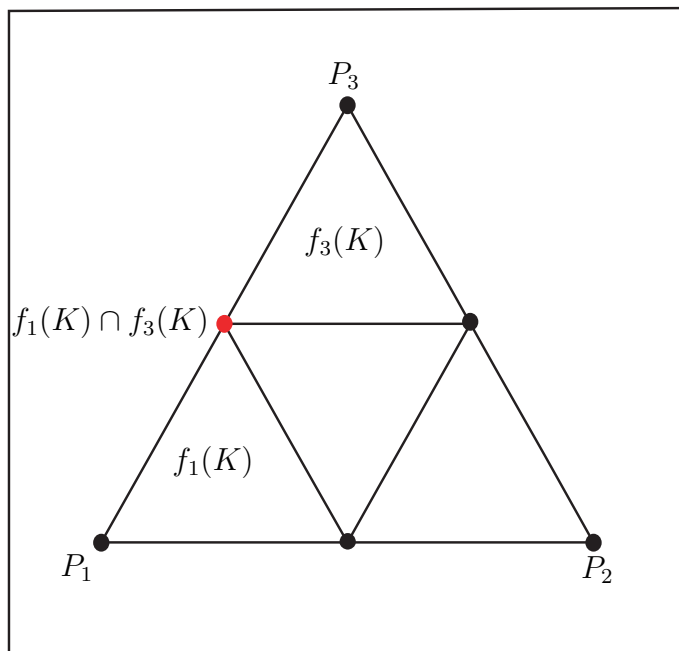


Figure 2.3: The overlap of $f_1(K)$ and $f_3(K)$ is a single point.

think of such a sequence of maps as an infinite sequence of symbols and that this constitutes the *address* of the limiting point. Although every point in K corresponds to at least one symbol sequence (i.e. has an address), it is possible for two different symbol sequences to give rise to the same point. For example, consider the red point in Figure 2.3. This point can be thought of as either the image of the point P_1 under the map f_3 , or the image of the point P_3 under the map f_1 , so the corresponding symbol sequence could begin with either a 1 or a 3.

A way to formalise this idea is to consider the space of symbol sequences. We shall refer to a sequence of m symbols as a word of length m . This idea is fundamental to the understanding of the topological structure of self-similar sets.

Definition 2.3. Let $\Sigma^N = \{w_1w_2w_3 \dots : w_i \in \{1, 2, \dots, N\}, i \in \mathbb{N}\}$ be the collection of infinite words in N symbols. Then Σ^N is called the shift space in N symbols.

It is often useful to consider words of finite length, which we formally define as follows:

Definition 2.4. For $m \geq 1$, $W_m^N = \{w_1 w_2 \dots w_m : w_i \in \{1, 2, \dots, N\}\}$ is a word of length m in N symbols. Then, we define

$$W_*^N = \bigcup_{m \geq 0} W_m^N$$

to be the set of all finite words in N symbols. We also define the empty word, $W_0^N = \emptyset$.

From this point onwards, we shall drop the superscript N when using Σ , W_m , and W_* . Using the above definitions, we state the following summary Theorem:

Theorem 2.5. For $w = w_1 w_2 \dots w_m \in W_*$, set $f_w = f_{w_1} \circ f_{w_2} \circ \dots \circ f_{w_m}$ and $K_w = f_w(K)$, where K is the self-similar set with respect to the contractions $\{f_i\}_{i=1}^N$. Then for any $\omega \in \Sigma$ the map $\pi : \Sigma \rightarrow K$ defined by

$$\{\pi(\omega)\} = \bigcap_{m \geq 1} K_{\omega_1 \omega_2 \dots \omega_m}$$

is a continuous surjective map and $\bigcap_{m \geq 1} K_{\omega_1 \omega_2 \dots \omega_m}$ contains only one point.

A nice property of the map π can be seen by considering shift maps on Σ , which we define here.

Definition 2.6. For $k \in \{1, 2, \dots, N\}$, we define the map $\sigma_k : \Sigma \rightarrow \Sigma$ by $\sigma_k(w_1 w_2 w_3 \dots) = k w_1 w_2 w_3 \dots$. Also, we define the shift map, $\sigma : \Sigma \rightarrow \Sigma$, by $\sigma(w_1 w_2 w_3 \dots) = w_2 w_3 w_4 \dots$.

The map π plays an important role in our analysis. We can think of π as a map that takes words in Σ to points on our self-similar set K and every point in K can be represented in this way. Since $\pi(\Sigma)$ is a non-empty compact set Theorem 2.2 implies that $\pi(\Sigma) = K$.

The procedure defined in Theorem 2.5 converges to a single point because we are considering *backward iteration*: as we add a new symbol to our word, the corresponding contraction is applied first and the previous sequence acts upon this set. If, on the other hand we were to consider *forward iteration*, the process would not converge

since each new symbol added to the sequence determines the final contraction applied. Forward iteration defines a dynamical process on K which is stochastic. Given any $x \in K$, this can move to one of N new points in K according to which of the maps f_i is applied. This is also known as a random iteration procedure and leads to an ergodic process. The forward and backward iteration of random (Lipschitz) functions is considered in [15].

Clearly, for any $i \in \{1, 2, \dots, N\}$,

$$\{\pi \circ \sigma_i(w)\} = \bigcap_{m \geq 1} K_{iw_1w_2\dots w_m} = \bigcap_{m \geq 1} f_i(K_{w_1w_2\dots w_m}) = \{f_i \circ \pi(w)\}. \quad (2.8)$$

Moreover, if we define $\dot{w} = w w w \dots$ for $w \in W_*$, $w \neq \emptyset$ then by Theorem 2.2 and Theorem 2.5 $\pi(\dot{w})$ is the unique fixed point of f_w . This idea can be extended to give

$$\pi(v_1v_2\dots v_kv\dot{w}) = f_v(p_w),$$

where $v_1v_2\dots v_k \in W_*$ and p_w is the fixed point of f_w . Since periodic sequences are dense in Σ , given a suitable topology (see [48]), we have

$$K = \overline{\{p_w : w \in W_*, w \neq \emptyset\}}.$$

Throughout this thesis we will use the following notation to refer to subsets of SG: if w is a word of length m , then K_w is an order- m subgasket.

Now we introduce the notion of self-similar structure to give a topological definition of self-similar sets and also give a definition of post critically finite (p.c.f.) self-similar sets, to which the analysis presented here can be applied.

Definition 2.7. *Let K be a compact metrisable topological space and let S be a finite set. Also, let f_i , $i \in S$ be a collection of continuous injections from K to itself. Then $(K, S, \{f_i\}_{i \in S})$ is called a self-similar structure if there exists a continuous surjection π as defined in Theorem 2.5.*

Most commonly we think of a self-similar structure as being $(K, \{1, 2, \dots, N\}, \{f_i\}_{i=1}^N)$ where $\{f_1, f_2, \dots, f_N\}$ are injective contractions.

Definition 2.8. Let $\mathcal{L} = (K, S, \{f_i\}_{i \in S})$ be a self-similar structure. We define

$$C_{\mathcal{L},K} = \bigcup_{i,j \in S, i \neq j} (f_i(K) \cap f_j(K)).$$

Then $\mathcal{C}_{\mathcal{L}} = \pi^{-1}(C_{\mathcal{L},K})$ is called the critical set of \mathcal{L} and $\mathcal{P}_{\mathcal{L}} = \bigcup_{n \geq 1} \sigma^n(\mathcal{C}_{\mathcal{L}})$ is called the post critical set of \mathcal{L} . Also, we define $V_0(\mathcal{L}) = \pi(\mathcal{P}_{\mathcal{L}})$.

We can think of $C_{\mathcal{L},K}$ as being the set of overlapping points when we apply each of the maps $\{f_i\}_{i \in S}$ to K and take the union of the resulting sets. Then the critical set is the set of words in Σ that, when the map π is applied, result in the set $C_{\mathcal{L},K}$. Also, the post critical set is the set of all possible pre-images of the critical set. The above definitions of the critical and post critical sets let us introduce the key notion of a p.c.f. self-similar structure. We say that a self-similar structure $\mathcal{L} = (K, S, \{f_i\}_{i \in S})$ is p.c.f. if and only if the post critical set is finite.

Once again, let us consider our continuing example of the Sierpinski Gasket. We have that

$$\mathcal{L} = (SG, \{1, 2, 3\}, \{f_i\}_{i=1}^3) \tag{2.9}$$

with the f_i as defined in (2.4) is a self-similar structure. It is easy to see that $\pi(\dot{j}) = P_j$ is the unique fixed point of f_j , $j = 1, 2, 3$. Let the vertex midway along the edge between P_i and P_j be q_k where $i \neq j \neq k \in \{1, 2, 3\}$. The set of overlaps is given by

$$C_{\mathcal{L},SG} = \{q_1, q_2, q_3\}, \tag{2.10}$$

and the critical set and post critical set are

$$\begin{aligned} \mathcal{C}_{\mathcal{L}} &= \{\dot{1}\dot{2}, \dot{2}\dot{1}, \dot{1}\dot{3}, \dot{3}\dot{1}, \dot{2}\dot{3}, \dot{3}\dot{2}\}, \\ \mathcal{P}_{\mathcal{L}} &= \{\dot{1}, \dot{2}, \dot{3}\}. \end{aligned} \tag{2.11}$$

Clearly, $\mathcal{P}_{\mathcal{L}}$ is a finite set and so the self-similar set SG is indeed post critically finite.

2.2 Energy and Harmonic Functions on the Sierpinski Gasket

We begin our discussion of harmonic functions on p.c.f. self-similar sets by considering the classical case of harmonic functions of \mathbb{R}^2 . Consider a bounded, connected and open domain in \mathbb{R}^2 denoted by Ω . We define the boundary of Ω by $\partial\Omega$, and the corresponding closed set $\bar{\Omega}$ is given by

$$\bar{\Omega} = \Omega \cup \partial\Omega.$$

Then a function $u \in C^2(\Omega) \cap C(\bar{\Omega})$ is said to be *harmonic* in Ω if

$$\Delta u = 0 \quad \text{for all } (x, y) \in \Omega,$$

where Δ is the Laplacian on \mathbb{R}^2 . Here, $u \in C^2(\Omega)$ means that all partial derivatives of u up to second order are continuous in Ω . A harmonic function u with given boundary values has the following properties: u attains its maximum and minimum on the boundary, u is uniquely determined by the values on the boundary, and u minimises the energy for all functions f that share the same boundary values, where the energy of a function f is defined to be

$$\mathcal{E}(f) = \int |\nabla f|^2. \tag{2.12}$$

The above properties can also be made to hold for harmonic functions on the Sierpinski Gasket. However, we have not yet defined what is meant by the Laplacian on Sierpinski Gasket so we must work backwards. We will define first of all what we mean by a harmonic function, u , on SG and later show that it satisfies the condition $\Delta u = 0$. The theory of harmonic functions on p.c.f. self-similar sets was developed by Kigami, see [45, 43, 44]. We shall adopt his approach here and begin by introducing the harmonic difference operator on the graph Γ_m .

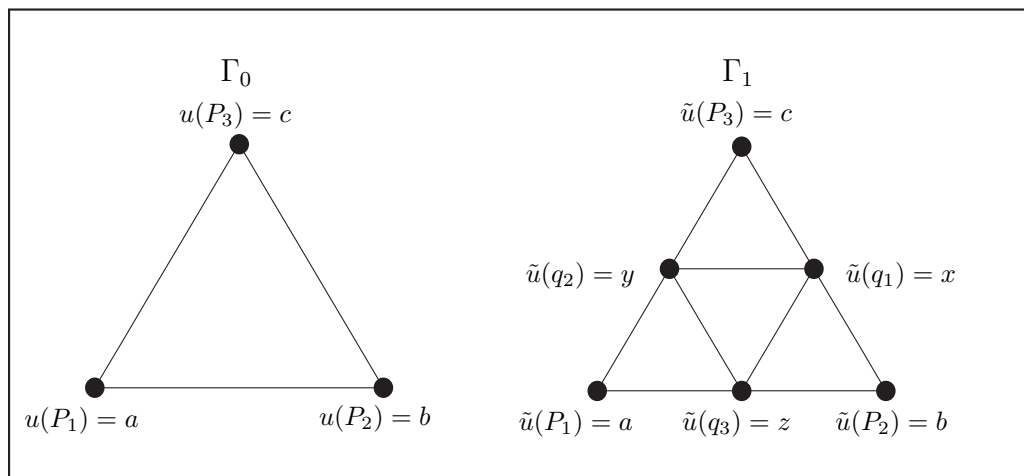


Figure 2.4: The harmonic extension from Γ_0 to Γ_1 .

Definition 2.9. Let $l(V_m) = \{f | f : V_m \rightarrow \mathbb{R}\}$ and define the map $H_m : l(V_m) \rightarrow l(V_m)$ by

$$(H_m f)(x) = \sum_{x \underset{m}{\sim} y} (f(y) - f(x)), \quad (2.13)$$

where $f \in l(V_m)$ and $x \in V_m$.

Consider the level m graph approximation to SG (or indeed any p.c.f. self-similar set) and a function $f \in l(V_m)$ defined on the graph. We define the graph *energy* of f to be

$$E_m(f) = \sum_{x \underset{m}{\sim} y} (f(y) - f(x))^2, \quad (2.14)$$

however, these energy forms are not related to each other for different m . Given a function f on V_m , there are many extensions of f onto V_{m+1} but only one that minimises the energy. We denote this energy-minimising extension \tilde{f} and call it the harmonic extension of f . We would like the following consistency condition to hold:

$$E_{m+1}(\tilde{f}) = c_m E_m(f), \quad (2.15)$$

where c_m is a renormalisation factor.

To calculate c_m consider a function u defined on V_0 where the boundary vertices P_1, P_2, P_3 take the values a, b, c respectively, see Figure 2.4. We want to extend the function u to V_1 , where the values of the extension \tilde{u} at the nodes q_i , $i = 1, 2, 3 \in V_1 \setminus V_0$ are chosen so that the energy is minimised. Calculating E_1 from equation (2.14) and minimising with respect to \tilde{u} at q_1, q_2 and q_3 , we find that the values of the harmonic extension \tilde{u} at nodes q_1, q_2, q_3 are given by

$$\begin{aligned} 4x &= b + c + y + z, \\ 4y &= a + c + x + z, \\ 4z &= a + b + x + y. \end{aligned} \tag{2.16}$$

We see that the value of \tilde{u} at the interior node q_i , $i = 1, 2, 3$ is the average of the value of the function at the four neighbours of q_i . Equations (2.16) lead us to give a definition of a harmonic function on the Sierpinski Gasket.

Definition 2.10. *The function $u \in l(V_m)$ is said to be harmonic on Γ_m if, for every interior node, the value of u at node x is the average of the values of u at the four neighbours of x . That is:*

$$u(x) = \frac{1}{4} \sum_{x \underset{m}{\sim} y} u(y). \tag{2.17}$$

Equations (2.16) can be rearranged to give an explicit expression for $\tilde{u}(q_i)$ in terms of the boundary values a, b, c .

$$\begin{aligned} x &= \frac{2}{5}b + \frac{2}{5}c + \frac{1}{5}a, \\ y &= \frac{2}{5}a + \frac{2}{5}c + \frac{1}{5}b, \\ z &= \frac{2}{5}a + \frac{2}{5}b + \frac{1}{5}c. \end{aligned} \tag{2.18}$$

Equations (2.18) give the “ $\frac{2}{5} - \frac{1}{5}$ ” rule for determining the values of the harmonic extension \tilde{u} on V_1 for given boundary values. In fact, the self-similarity of the gasket means that the harmonic extension can be seen as local and therefore the same result

holds for all harmonic extensions from V_m to V_{m+1} . A nice way to describe this harmonic extension algorithm is in the following form.

$$\begin{pmatrix} u(F_w P_1) \\ u(F_w P_2) \\ u(F_w P_3) \end{pmatrix} = A_{w_1} \cdots A_{w_m} \begin{pmatrix} u(P_1) \\ u(P_2) \\ u(P_3) \end{pmatrix}, \quad (2.19)$$

where the A_i , $i = 1, 2, 3$ are matrices given by

$$A_1 = \begin{pmatrix} 1 & 0 & 0 \\ \frac{2}{5} & \frac{2}{5} & \frac{1}{5} \\ \frac{2}{5} & \frac{1}{5} & \frac{2}{5} \end{pmatrix}, \quad A_2 = \begin{pmatrix} \frac{2}{5} & \frac{2}{5} & \frac{1}{5} \\ 0 & 1 & 0 \\ \frac{1}{5} & \frac{2}{5} & \frac{2}{5} \end{pmatrix}, \quad A_3 = \begin{pmatrix} \frac{2}{5} & \frac{1}{5} & \frac{2}{5} \\ \frac{1}{5} & \frac{2}{5} & \frac{2}{5} \\ 0 & 0 & 1 \end{pmatrix}. \quad (2.20)$$

Using the harmonic extension algorithm we can express the energy E_1 in terms of the boundary values a, b, c and we find that $c_1 = \frac{5}{3}c_0$. In general the renormalisation constant is

$$c_m = \left(\frac{5}{3}\right)^m c_0, \quad (2.21)$$

and for simplicity we take $c_0 = 1$. Then we have

$$\mathcal{E}_1(\tilde{u}) = \frac{5}{3}E_1(\tilde{u}) = \mathcal{E}_0(u), \quad (2.22)$$

and in general

$$\mathcal{E}_{m+1}(\tilde{u}) = \left(\frac{5}{3}\right)E_{m+1}(\tilde{u}) = \mathcal{E}_m(u). \quad (2.23)$$

We will now go on to state some theorems regarding harmonic functions on SG and their properties.

Theorem 2.11. *Given any three numbers a, b, c , there exists a unique harmonic function u on the Sierpinski Gasket satisfying $u(P_1) = a$, $u(P_2) = b$, $u(P_3) = c$.*

Proof of Theorem 2.11 can be found in [76].

Theorem 2.12 (The Maximum Principle). *If a harmonic function defined on the Sierpinski Gasket K , attains the maximum value in the interior $K \setminus V_0$ of K , then u is constant throughout K .*

The following proposition summarises the basic results from [43] concerning the renormalised energy \mathcal{E} and harmonic functions on K :

Proposition 2.13. *For any continuous function f on K , the sequence $\mathcal{E}(f)$ is monotonically increasing and so*

$$\mathcal{E}(f) = \lim_{m \rightarrow \infty} \mathcal{E}_m(f)$$

is well-defined and

$$\mathcal{E}(f) = 0 \Leftrightarrow f \text{ is constant.}$$

We denote by $\text{dom}(\mathcal{E})$ the set of continuous functions for which $\mathcal{E}(f) < \infty$.

For a harmonic function u , the energy remains constant over all levels, in fact

$$\mathcal{E}_m(u) = \mathcal{E}(u) \text{ for all } m.$$

2.3 Defining the Laplacian on the Sierpinski Gasket

The theory of harmonic functions on SG described in Section 2.2 extends to allow us to define what is meant by the Laplacian operator on the Sierpinski Gasket in the sense of Kigami (see [43] for the SG case or [44] for the general case of p.c.f self-similar sets). We can define a Laplacian on the Sierpinski Gasket via the weak formulation for the Poisson problem:

$$\Delta f = g. \tag{2.24}$$

The weak solution satisfying (2.24) is given by

$$\int \nabla f \cdot \nabla v \, dx = - \int g v \, dx \tag{2.25}$$

for all functions v in a suitable test space. On the Sierpinski Gasket, the analogue of $\int \nabla f \cdot \nabla v \, dx$ is given by the energy form $\mathcal{E}(f, v)$ and we must also choose a suitable

measure μ to play the role of dx on the right hand side of (2.25). We consider the standard self-similar probability measure:

$$\mu = \sum_{i=0}^2 \frac{1}{3} \mu \circ F_i^{-1}. \quad (2.26)$$

We can now give a formal definition of the (Kigami) Laplacian on the Sierpinski Gasket:

Definition 2.14. *A function $f \in \text{dom}(\mathcal{E})$ is in the domain of the Laplacian, $\text{dom}(\Delta)$ and $\Delta f = g$ if and only if there exists a continuous function g such that*

$$\mathcal{E}(f, v) = - \int gv \, d\mu, \quad (2.27)$$

for all suitable test functions $v \in \text{dom}(\mathcal{E})$ that vanish on the boundary.

It is also possible to define the Laplacian Δ by the pointwise formula

$$\Delta f(x) = \lim_{m \rightarrow \infty} \frac{3}{2} 5^m \sum_{x \underset{m}{\sim} y} (f(y) - f(x)) \quad (2.28)$$

for any nonboundary vertex x . Note that it is indeed true that a function u is harmonic as defined in Section 2.2 if and only if $\Delta u = 0$ with Δ defined by (2.28). We can also define normal derivatives at the boundary points:

$$\partial_n f(x) = \lim_{m \rightarrow \infty} \left(\frac{5}{3} \right)^m \sum_{x \underset{m}{\sim} y} (f(y) - f(x)). \quad (2.29)$$

The formulae defined in (2.28) and (2.29) make it possible for us to define PDEs involving second order spatial derivatives and to solve them numerically. The simplest idea is to semi-discretise the problem (the analogue of the method of lines) by using the formula (2.28) as a discrete approximation to the Laplacian. The resulting ODE system can be solved by a suitable numerical technique. This technique was used in [14] for the heat and wave equations on SG. The analogue of the finite element method has also been developed on the Sierpinski Gasket using spline spaces, see [25] and [68]. A clear overview of the method, the programs used and the results can be found at [24].

2.3.1 Physically-Motivated Derivation

From a physical point of view we can see where the coefficient $\frac{3}{2}5^m$ comes from in (2.28) by considering the gasket as a system of point masses connected by springs of strength k , as discussed in [76]. We assume that the masses move only perpendicular to the plane in which the gasket lies. This has been called the ‘‘Sierpinski Drum’’.

In Euclidean space, the vibration of a surface can be modelled by the wave equation:

$$M \frac{\partial^2 u}{\partial t^2} = k \Delta u \quad \text{on } \Omega, \quad (2.30)$$

where $u(x, y, t)$ gives the position at time t , M is the mass of the surface, and the domain Ω is the surface of the drum. We can construct the analogue of equation (2.30) on our sequence of graph approximations to SG. Then in the limit as $m \rightarrow \infty$ we will model the vibration on the Sierpinski Gasket. Let $M_{x,m}$ be the point mass at node x on Γ_m , and let the pair (x, y) denote the spring joining node x to node y . Then, using Hooke’s law, the resultant force on node x at time t will be the sum of all forces of springs connected to x . We write

$$F_{x,t} = - \sum_{\substack{x \sim y \\ m}} k_m (u(x, t) - u(y, t)), \quad (2.31)$$

and so for each node x we may write the equation of motion as

$$M_{m,x} \frac{d^2}{dt^2} u(x, t) = k_m (H_m u)(x), \quad (2.32)$$

with $(H_m u)(x)$ as defined by (2.13). The problem remains as to what are suitable values of $M_{m,x}$ and k_m .

The Mass Distribution

We are assuming that the mass, M , of the Sierpinski Gasket is uniformly distributed. Therefore, we divide Γ_m into 3^m order m , or *minimal* triangles. Each minimal triangle

has mass $\frac{1}{3^m} M$. From this it is clear that we can define the point masses by

$$M_{m,x} = \begin{cases} \frac{2}{3^{m+1}} M, & x \in V_m \setminus V_0, \\ \frac{1}{3^{m+1}} M, & x \in V_0, \end{cases} \quad (2.33)$$

since the interior nodes receive contributions from two minimal triangles, while the boundary nodes only receive contributions from one minimal triangle.

The Spring Constant

To obtain the appropriate value for the spring constant k_m we must first consider the properties of Hookian springs in series and in parallel. In fact, using such springs in series and parallel produces effective springs with force constants which look like the parallel and series laws for combining electrical resistances. We find that two springs combined in parallel with force constants k_1 and k_2 behave like a single spring with force constant

$$k_{eff} = k_1 + k_2.$$

Similarly, the same two springs joined in series act as a single spring with force constant given by

$$\frac{1}{k_{eff}} = \frac{1}{k_1} + \frac{1}{k_2}.$$

Now consider the point masses and springs arranged as the zero level graph approximation to the Sierpinski Gasket where each spring has spring constant k_0 . Arranged in this manner the three springs act as a single entity and we can find the force constant of the spring by using the analogue of the star-triangle transformation for electrical resistances: the effective force constant of three Hookian springs arranged as a triangle, each with spring constant k is the same as the effective force constant of three springs arranged as a star, where the spring constant of each spring is $3k$, see Figure 2.5. Using the star-triangle transformation and the rule for springs in series, we see that the three springs arranged as the triangle behave as a single spring with

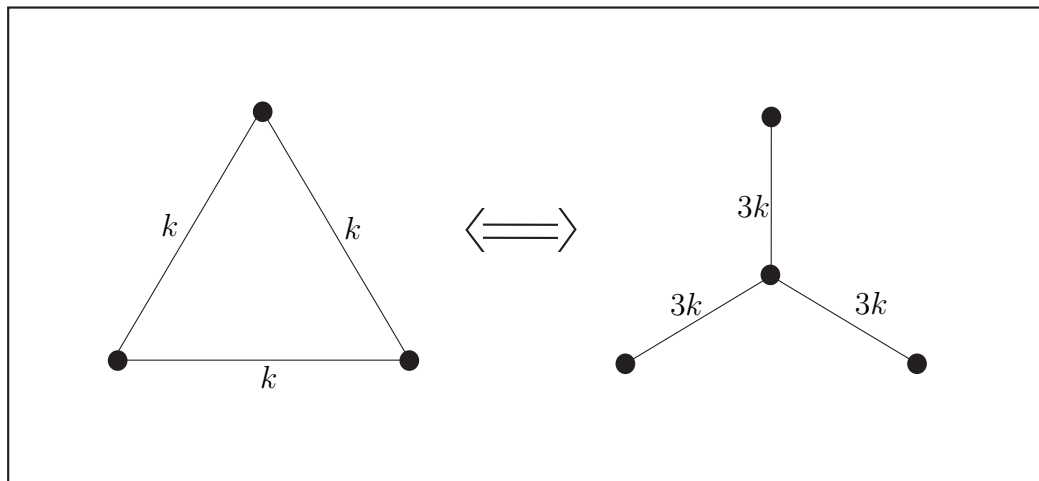


Figure 2.5: The star-triangle transformation for Hookian springs.

spring constant

$$k_{eff} = \frac{3}{2} k_0. \quad (2.34)$$

Next we consider the Γ_1 approximation to SG, where each spring has spring constant k_1 . Once again, by applying the star-triangle transformation and the rule for springs in series, we see that the system behaves as a zero level approximation to the gasket where the spring constant of each spring is given by (see Figure 2.6)

$$k_{eff} = \frac{3}{5} k_1. \quad (2.35)$$

Comparing (2.34) and (2.35) we see that the spring constants are related by $k_1 = \frac{5}{3} k_0$. In general we have for every $m \geq 0$,

$$k_{m+1} = \frac{5}{3} k_m. \quad (2.36)$$

With $k_0 = k$ this becomes

$$k_m = \left(\frac{5}{3}\right)^m k. \quad (2.37)$$

Now we have found suitable values for the mass distribution $M_{m,x}$ and the spring constant k_m , we can substitute these values into our equation of motion (2.32) for the

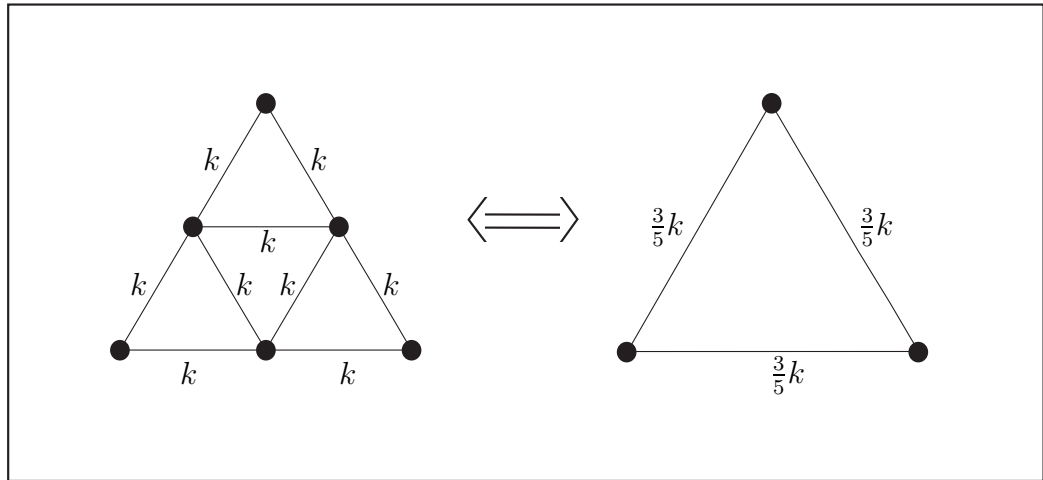


Figure 2.6: The Γ_1 system of springs can be reduced to the Γ_0 system with related spring constants.

system to obtain the following equations:

$$\begin{aligned} M \frac{d^2}{dt^2} u(x, t) &= \frac{3}{2} 5^m k (H_m u)(x) && \text{for } x \in V_m \setminus V_0, \\ M \frac{d^2}{dt^2} u(x, t) &= 3 \times 5^m k (H_m u)(x) && \text{for } x \in V_0. \end{aligned} \tag{2.38}$$

Taking the limit as $m \rightarrow \infty$ we arrive at the wave equation describing the surface vibration of the Sierpinski Drum. Comparing equations (2.38) and (2.30) we see that the Laplacian on the Sierpinski Gasket can indeed be defined by

$$\Delta u(x) = \lim_{m \rightarrow \infty} \frac{3}{2} 5^m (H_m u)(x), \tag{2.39}$$

for vertices $x \in V_m \setminus V_0$.

2.4 Other p.c.f. Self-Similar Sets

In Chapter 1 we discussed how many naturally occurring objects can have fractal structure. Although these objects are only approximately self-similar, they are well-approximated by exactly self-similar sets generated by deterministic processes. Many

of the biological and physiological examples we considered in Chapter 1 share a self-similar tree-like structure, such as the dendritic tree of a neuron and the bronchial tree in the lung.

The Sierpinski Gasket has been a useful example in the development in the theory of Analysis on Fractals. However, a major application of this area of mathematics is to model dynamical processes on approximations to naturally occurring objects. For this purpose, the Sierpinski Gasket is not the best choice of self-similar set to consider. Ideally, we would like to model these processes on a p.c.f. fractal tree. An example of such a self-similar set is the tree-like set which was first defined by Hata [27]. Hata's tree-like set is defined as follows: Let $X = \mathbb{C}$. Set

$$\begin{aligned} f_1(z) &= c\bar{z} \\ f_2(z) &= (1 - |c|^2)\bar{z} + |c|^2 \end{aligned} \tag{2.40}$$

where $c \in \mathbb{Z}$ and $|c| < 1$, $|1 - c| \in (0, 1)$. If we let $A = \{t : 0 \leq t \leq 1\} \cup \{tc : 0 \leq t \leq 1\}$, then $f_1(A) \cup f_2(A) \supset A$. Hence if

$$A_m = \bigcup_{w \in W_m} f_w(A)$$

then $\{A_m\}_{m \geq 0}$ is an increasing sequence and the self-similar set $K = \overline{\bigcup_{m \geq 0} A_m}$ is shown in Figure 2.7. Referring to Definition 2.8 we see that for the Hata Tree, we have

$$\begin{aligned} C_{\mathcal{L}, K} &= \{|c|^2\}, \\ \mathcal{C}_{\mathcal{L}} &= \{1\dot{1}\dot{2}, 2\dot{1}\}, \\ \mathcal{P}_{\mathcal{L}} &= \{1\dot{2}, \dot{2}, \dot{1}\}. \end{aligned}$$

The *boundary* of the Hata Tree is defined as $V_0(\mathcal{L}) = \{0, 1, c\}$. We would like to construct a Laplacian on the Hata Tree in an analogous way to the case of the Sierpinski Gasket. According to Kigami's theory we can calculate the energy of each of the graph approximations to Hata's Tree via the formula defined in equation (2.14)

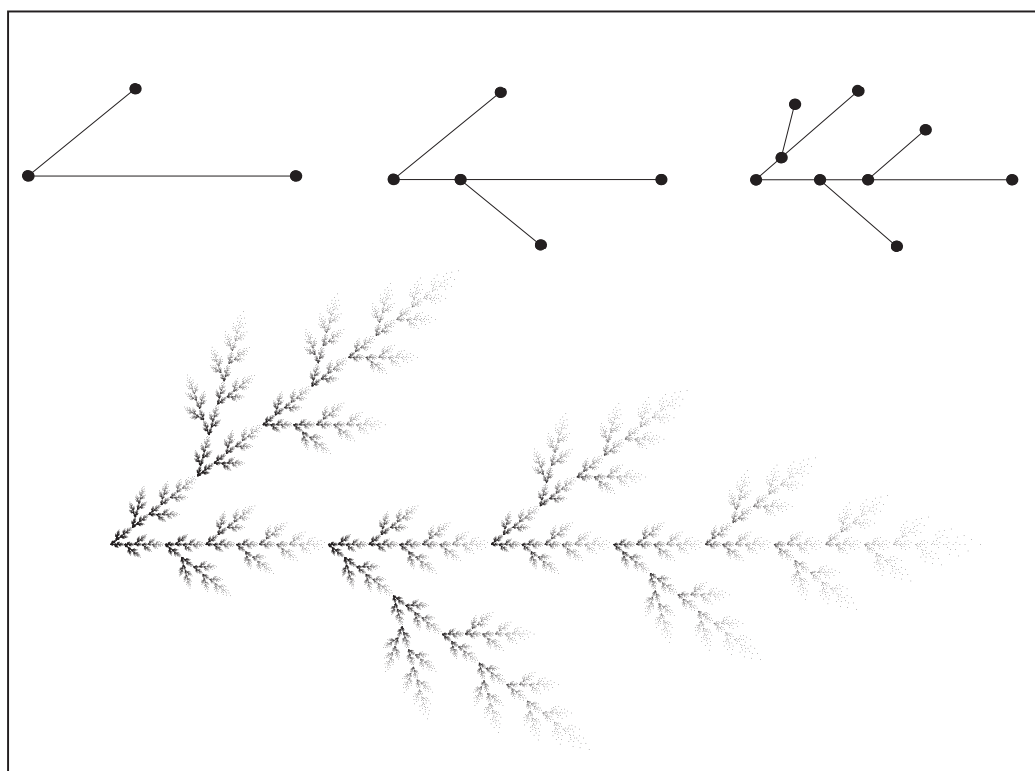


Figure 2.7: The approximating sequence $\Gamma_0, \Gamma_1, \Gamma_2$ and a random iteration procedure converging to Hata's tree-like set. Here we have taken $c = 0.4 + 0.3\sqrt{-1}$.

so that for a function $u \in l(V_0)$ we have

$$E_0(u) = \{u(0) - u(1)\}^2 + \{u(0) - u(c)\}^2. \quad (2.41)$$

We wish to find an extension of u to V_1 that minimises the energy. Once again, this harmonic extension is denoted by \tilde{u} and we would like to find a renormalisation constant c_m such that

$$E_{m+1}(\tilde{u}) = c_m E_m(u). \quad (2.42)$$

We proceed by calculating E_1 and minimising with respect to x and y . We find that

$$\begin{aligned} 3x &= a + b + y, \\ y &= x, \end{aligned} \quad (2.43)$$

so that an explicit expression for the values of \tilde{u} at the points $V_1 \setminus V_0$ is

$$x = y = \frac{1}{2}(a + b). \quad (2.44)$$

and the energy is given by

$$E_1(\tilde{u}) = \frac{1}{2} \{\tilde{u}(1) - \tilde{u}(0)\}^2 + \{\tilde{u}(c) - \tilde{u}(0)\}^2. \quad (2.45)$$

Clearly, in this case, there is no nice counterpart of the harmonic extension algorithm that we found for the Sierpinski Gasket and there is no constant c such that $E_1 = cE_0$. In fact the values of \tilde{u} at the newly generated points are just the average of the values at the neighbouring boundary points. If we were to carry on in this manner, we would see that, as m increases, the harmonic functions will become constant along the branches and the energy will become zero.

This problem occurs due to Kigami's notion of boundary. For a fractal tree, a more natural notion of boundary would be to define the set of boundary points as those points that are the tips of the branches. So, as m increases, the set of boundary points grows also. Thus, for the Hata Tree, K , the set of boundary points would actually be an uncountable set. The addresses of such points would be all symbol sequences not in the critical set $\mathcal{C}_{\mathcal{L}}$ ending in $\dot{2}$.

The necessary development would require the separation of the notions of boundary and the post-critical set and would be a major departure from the theory we have described here. The rest of this thesis will be concerned with understanding the consequences of the complexity implied by defining nonlinear PDEs on the Sierpinski Gasket and so this issue will not be addressed further.

Chapter 3

Spectrum and Eigenfunctions of the Laplacian on the Sierpinski Gasket

3.1 Introduction

Now that we have a definition for a Laplacian operator on the Sierpinski Gasket, we are able to study the eigenvalue problem

$$-\Delta v = \lambda v. \tag{3.1}$$

The spectrum of the Laplacian on SG was first studied by the physicists Rammal and Toulouse, [60], [59]. Subsequently Shima [64] and Fukushima and Shima [20] completely determined the eigenvalues and multiplicities of the harmonic difference operator H_m in the case of both Dirichlet and Neumann boundary conditions. The numerical computation of such eigenvalues was also presented in [14].

Definition 3.1. *If the function v that solves the eigenvalue problem (3.1) also satisfies the condition*

$$v|_{\Gamma_0} = 0$$

then the eigenfunction v is called a *Dirichlet eigenfunction* (*D-eigenfunction* for short) of $-\Delta$. Similarly, if v satisfies the condition

$$\partial_n v(x) = 0 \quad \forall x \in \Gamma_0,$$

where ∂_n is the normal derivative defined in equation (2.29), then v is called a *Neumann eigenfunction* (*N-eigenfunction*) of $-\Delta$.

We specialise to the case of the Sierpinski Gasket in the plane ($N = 3$ in [64] and [20]) and work with our graph approximations to the Sierpinski Gasket: $\Gamma_m = \{V_m, E_m\} \subset \mathbb{R}^2$, $m = 0, 1, 2, \dots$. In this section, we will begin by considering the m -harmonic difference of a function f at a non-boundary vertex $x \in V_m$ as defined in (2.13). The Laplacian on the Sierpinski Gasket is simply defined to be the renormalised limit of H_m , according to (2.28) as $m \rightarrow \infty$.

Consider the discrete eigenvalue problem:

$$-\Delta_m v_m = \lambda_m v_m \tag{3.2}$$

where Δ_m is the graph Laplacian defined on V_m , defined in terms of the harmonic difference operator

$$(H_m f)(x) = \sum_{x \underset{m}{\sim} y} (f(y) - f(x)) \tag{3.3}$$

for all non-boundary vertices x (see equation (2.13)). Until now, we have only defined harmonic differences on interior nodes and have not considered what happens at the boundary vertices P_i , $i = 1, 2, 3$. In the following sections we will describe the spectrum of H_m in the case of Dirichlet and Neumann boundary conditions.

3.2 Eigenvalues of the Laplacian on the Sierpinski Gasket

3.2.1 Eigenvalues of $-\mathcal{H}_m^0$ (Dirichlet Boundary Condition)

First, let us consider Dirichlet conditions at the boundary. We define the linear operator

$$(\mathcal{H}_m^0 f)(x) = \begin{cases} (H_m f)(x) & \text{if } x \in V_m \setminus V_0 \\ 0 & \text{if } x \in V_0 \end{cases}. \quad (3.4)$$

We see that $-\mathcal{H}_m^0$ can be written as a $(\frac{3}{2}(3^m - 1) \times \frac{3}{2}(3^m - 1))$ sparse matrix.

To begin with, we consider the eigenvalues of

$$-\mathcal{H}_1^0 = \begin{pmatrix} 4 & -1 & -1 \\ -1 & 4 & -1 \\ -1 & -1 & 4 \end{pmatrix}. \quad (3.5)$$

We find that there is an eigenvalue equal to 2 which occurs with single multiplicity. Corresponding to this is the eigenfunction

$$v_1^1(x) = \begin{cases} 1 & \text{for } x \in V_1 \setminus V_0, \\ 0 & \text{otherwise} \end{cases}. \quad (3.6)$$

Also, there is an eigenvalue equal to 5 which occurs with multiplicity 2. The corresponding eigenfunctions in this case are v_2^1 and v_3^1 and are given by:

$$v_k^1(x) = \begin{cases} 1 & \text{for } x = q_{k-1}, \\ -1 & \text{for } x = q_3, \\ 0 & \text{otherwise} \end{cases}, \quad k = 2, 3. \quad (3.7)$$

We denote the set of eigenvalues of $-\mathcal{H}_m^0$ by \mathcal{A}_m and so $\mathcal{A}_1 = \{2, 5, 5\}$.

Given the self-similar nature of SG, there exists a natural decimation procedure, which enables us to relate eigenvalues of $-\mathcal{H}_m^0$ to those of $-\mathcal{H}_{m-1}^0$. Consider the

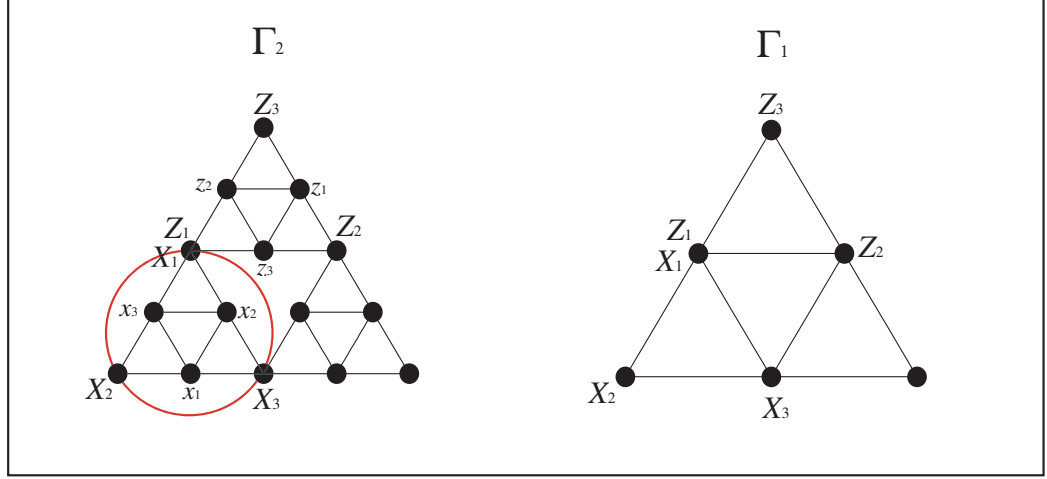


Figure 3.1: The nodes considered for the decimation procedure.

eigenvalue problem for the vertices circled in the left hand part of Figure 3.1 and define the vectors

$$v(\underline{X}) = \begin{pmatrix} v(X_1) \\ v(X_2) \\ v(X_3) \end{pmatrix}, \quad v(\underline{x}) = \begin{pmatrix} v(x_1) \\ v(x_2) \\ v(x_3) \end{pmatrix}, \quad (3.8)$$

and the matrices

$$A = \begin{pmatrix} -4 & 1 & 1 \\ 1 & -4 & 1 \\ 1 & 1 & -4 \end{pmatrix}, \quad M = \begin{pmatrix} 0 & 1 & 1 \\ 1 & 0 & 1 \\ 1 & 1 & 0 \end{pmatrix}. \quad (3.9)$$

We assume here that $v(\underline{X})$ is known and we wish to relate the eigenvalue problem on Γ_2 to that on Γ_1 , that is, we wish to find the values of $v(\underline{x}_i)$, $i = 1, 2, 3$ in terms of the values $v(\underline{X}_i)$, $i = 1, 2, 3$.

The eigenvalue problem restricted to these vertices on Γ_2 is then

$$Av(\underline{x}) + Mv(\underline{X}) = -\lambda \mathbb{I}v(\underline{x}), \quad (3.10)$$

where \mathbb{I} is the 3×3 identity matrix. System (3.10) can be solved to obtain an

expression for $v(\underline{x})$ in terms of $v(\underline{X})$:

$$\begin{aligned} v(\underline{x}) &= -(A + \lambda \mathbb{I})^{-1} M v(\underline{X}) \\ &= \frac{1}{(\lambda - 5)(\lambda - 2)} \begin{pmatrix} 2 & 4 - \lambda & 4 - \lambda \\ 4 - \lambda & 2 & 4 - \lambda \\ 4 - \lambda & 4 - \lambda & 2 \end{pmatrix} v(\underline{X}). \end{aligned} \quad (3.11)$$

Similar relationships exist for expressing $v(z_i)$ in terms of $v(Z_i)$, $i = 1, 2, 3$ in the upper uncircled subgraph of Γ_2 (see Figure 3.1) and similarly with the remaining unlabelled subgraph.

Equation (3.11) describes how the value of the eigenfunction at the nodes $x_i \in V_m \setminus V_{m-1}$ can be expressed purely in terms of the value of the function at the nodes X_i . This means that, given an eigenfunction of $-\mathcal{H}_{m-1}^0$ with eigenvalue λ , we can extend this to an eigenfunction of $-\mathcal{H}_m^0$ with eigenvalue λ' . The relationship between the eigenvalues λ and λ' can be found by comparing the eigenvalue problem for a point X_1 , for example, common to both V_1 and V_2 . We have on Γ_1 :

$$-4v(X_1) + \left(v(X_2) + v(X_3)\right) + \left(v(Z_2) + v(Z_3)\right) = -\lambda v(X_1), \quad (3.12)$$

and on Γ_2 :

$$-4v(X_1) + \left(v(x_2) + v(x_3)\right) + \left(v(z_2) + v(z_3)\right) = -\lambda' v(X_1). \quad (3.13)$$

Using equation (3.11) and its analogue for $v(z_i)$ we can express $\left(v(x_2) + v(x_3)\right)$ and $\left(v(z_2) + v(z_3)\right)$ in terms of $\{v(X_i)\}$ and $\{v(Z_i)\}$ respectively and substitute these values into equation (3.13), which can be written in the form

$$-4v(X_1) + \left(v(X_2) + v(X_3)\right) + \left(v(Z_2) + v(Z_3)\right) = -\lambda'(5 - \lambda')v(X_1). \quad (3.14)$$

Comparing this with equation (3.13) we see the relationship between λ and λ' is a quadratic:

$$\lambda = \lambda'(5 - \lambda'), \quad (3.15)$$

and we note that equation (3.15) is not invertible.

The results of this decimation procedure can be summarised by the following proposition [64]:

Proposition 3.2 (Decimation Method). *Let $l_0(V_m) = \{f \in l(V_m) : f(P_i) = 0, i = 1, 2, 3\}$ be the collection of real-valued functions on V_m that are zero on the boundary.*

1. *If $-\mathcal{H}_m^0 v = \lambda_m v$ for $v \in l_0(V_m)$, $\lambda_m \neq 6$, then $v|_{V_{m-1}} \in l_0(V_{m-1})$ and*

$$-\mathcal{H}_{m-1}^0(v|_{V_{m-1}}) = \lambda_m(5 - \lambda_m)v|_{V_{m-1}}.$$

2. *If $-\mathcal{H}_{m-1}^0 v = \lambda_m(5 - \lambda_m)v$ for $v \in l_0(V_{m-1})$ and $\lambda_m \neq 2, 5, 6$, then there exists a unique extension $\tilde{v} \in l_0(V_m)$ of v such that*

$$-\mathcal{H}_m^0 \tilde{v} = \lambda_m \tilde{v}.$$

Proposition 3.2 says that the restriction of an eigenfunction of $-\mathcal{H}_m^0$ with eigenvalue $\lambda_m \neq 6$ to V_{m-1} is an eigenfunction of $-\mathcal{H}_{m-1}^0$ with eigenvalue $\lambda_{m-1} = \lambda_m(5 - \lambda_m)$. Also, an eigenfunction of $-\mathcal{H}_{m-1}^0$ with eigenvalue $\lambda_{m-1} = \lambda_m(5 - \lambda_m)$, $\lambda_m \neq 2, 5, 6$ can be uniquely extended to an eigenfunction of $-\mathcal{H}_m^0$ with eigenvalue λ_m . The exclusion of the eigenvalue 2 in the second part of Proposition 3.2 is clear since $2 \in \mathcal{A}_m$ only for $m = 1$. It is less simple to explain the exclusion of 6 in part one of the proposition and 5 and 6 in part two of proposition 3.2.

The eigenvalues of $-\mathcal{H}_0^m$ that are calculated by the decimation procedure do not form the complete spectrum of the harmonic difference operator. The following proposition accounts for the existence and multiplicities of the remaining eigenvalues.

Proposition 3.3. *6 is an eigenvalue of $-\mathcal{H}_m^0$ with multiplicity $\frac{3}{2}\{3^m - 2 \times 3^{m-1} - 1\}$. 5 is an eigenvalue of $-\mathcal{H}_m^0$ with multiplicity $\frac{3}{2}\{3^{m-1} - 2 \times 3^{m-2} + 1\}$.*

For a proof of the first part of Proposition 3.3 see [64]. The multiplicity of the eigenvalue equal to 5 then follows since it will be equal to the difference between the

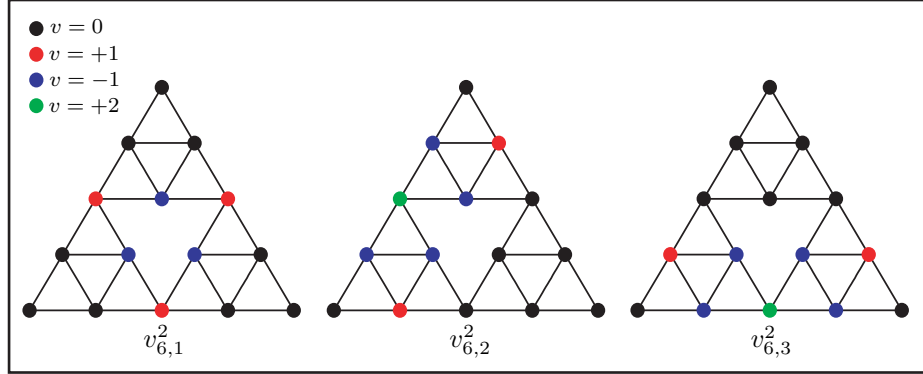


Figure 3.2: The three eigenfunctions of $-\mathcal{H}_2^0$ with eigenvalue $\lambda = 6$.

number of vertices of the graph Γ_m and the number of eigenvalues of $-\mathcal{H}_m^0$ deduced from the decimation procedure and Proposition 3.3.

Consider the eigenvalue $\lambda = 6$. This first occurs when $m = 2$ with multiplicity three. We shall denote the three eigenfunctions corresponding to this eigenvalue by $v_{6,i}^2$, $i = 1, 2, 3$. The values of these three eigenfunctions are shown in Figure 3.2 and it is easy to check that they are linearly independent. We also note that the $v_{6,i}^2$ s all satisfy both Dirichlet and Neumann boundary conditions. This family of three eigenfunctions on Γ_2 gives rise to nine eigenfunctions on Γ_3 that also have eigenvalue $\lambda = 6$. These eigenfunctions are constructed as follows. We take each of our eigenfunctions on Γ_2 , $v_{6,i}^2$, $i = 1, 2, 3$ and for each one, we take each of the maps of our IFS, f_j , $j = 1, 2, 3$. The support of our eigenfunction on Γ_3 will be the nodes $x \in V_3$ whose address begins with the symbol j . The eigenfunction will take the value zero at all other vertices. The value of our eigenfunction at a node $x \in V_3$ is then the value of $v_{6,i}^2$, $i = 1, 2, 3$ at the pre-image of x under the map f_j . This construction is illustrated in Figure 3.3.

According to Proposition 3.3 there exist a further three eigenfunctions of $-\mathcal{H}_3^0$ with eigenvalue $\lambda = 6$. Three such eigenfunctions are shown in Figure 3.4 and are denoted by $v_{6,i}^3$, $i = 10, 11, 12$. Once again the $v_{6,i}^3$ s form a linearly independent set and

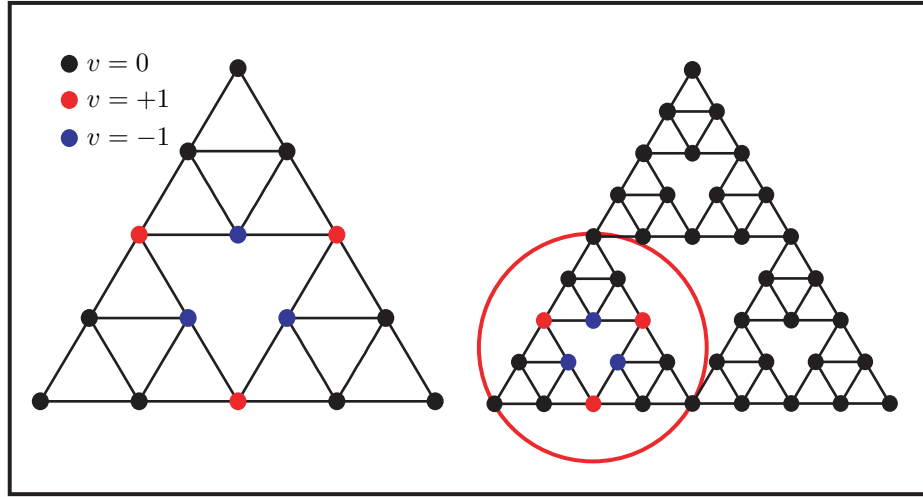


Figure 3.3: An eigenfunction on Γ_3 with eigenvalue $\lambda = 6$ that is constructed from an eigenfunction on Γ_2 , also with eigenvalue $\lambda = 6$.

satisfy Dirichlet-Neumann conditions. It is this property that allows us to construct eigenfunctions corresponding to $\lambda = 6$ on subsequent graph approximations to SG in this manner.

As m increases we can continue in this way to completely determine the eigenfunctions of $-\mathcal{H}_m^0$ with eigenvalue $\lambda = 6$ given that we know those of \mathcal{H}_{m-1}^0 . There will be $\frac{3}{2}\{3^m - 2 \times 3^{m-1} - 3\}$ eigenfunctions that come from contracting each of the eigenfunctions with $\lambda = 6$ on Γ_{m-1} onto the three order-one triangles of Γ_m . The remaining three eigenfunctions are the analogues of those shown in Figure 3.4, where the non-zero values are pulled towards the junction points q_1, q_2, q_3 as m increases.

We can tell a similar story to determine the eigenfunctions of $-\mathcal{H}_m^0$ corresponding to the eigenvalue $\lambda = 5$. On Γ_1 , the eigenvalues corresponding to $\lambda = 5$ are given by equation (3.7), however this is a special case, so, again we begin at $m = 2$. There are three eigenfunctions of $-\mathcal{H}_2^0$ with eigenvalue $\lambda = 5$, which we call $v_{5,i}^2$, $i = 1, 2, 3$. These are shown in Figure 3.5. Again, these three eigenfunctions are all linearly independent. However, only $v_{5,1}^2$ satisfies Dirichlet-Neumann conditions, so, when

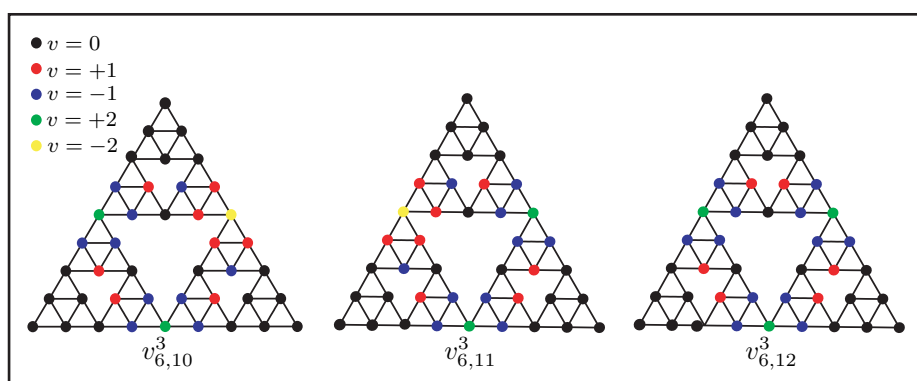


Figure 3.4: The three remaining eigenfunctions of $-\mathcal{H}_3^0$ with eigenvalue $\lambda = 6$.

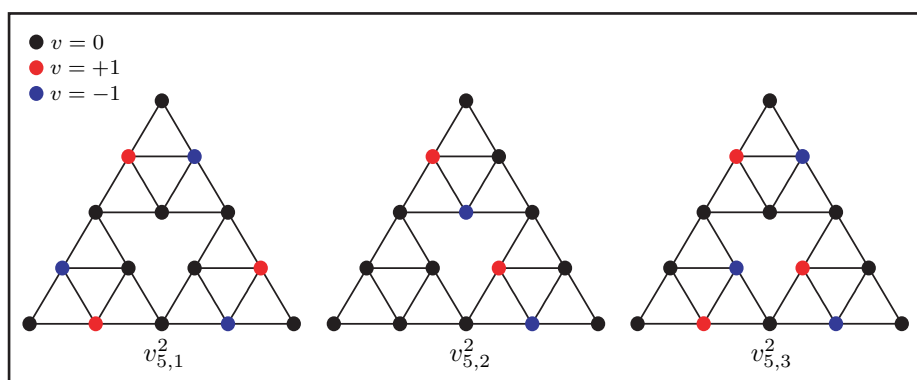


Figure 3.5: The three eigenfunctions of $-\mathcal{H}_2^0$ with eigenvalue $\lambda = 5$.

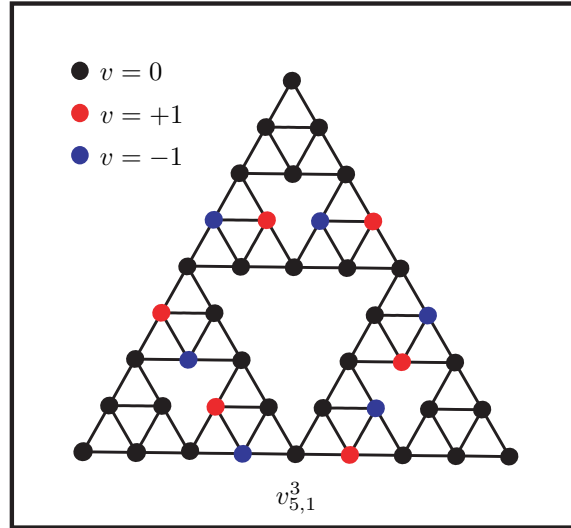


Figure 3.6: The eigenfunction $v_{5,1}^3$.

constructing eigenfunctions corresponding to $\lambda = 5$ on Γ_3 , we only construct three eigenfunctions whose support is confined to each of the three order-one triangles of Γ_3 . Again, Proposition 3.3 tells us that there are a further three eigenfunctions of $-\mathcal{H}_3^0$ with eigenvalue $\lambda = 5$. These are the analogues of those on Γ_2 shown in Figure 3.5.

Consider the Dirichlet-Neumann function $v_{5,1}^2$. We can think of this as a ring, of alternating sign around the central hole, but set back one row of nodes. An analogue of this eigenfunction exists for every Γ_m , which we always refer to as $v_{5,1}^m$. As $m \rightarrow \infty$ the support of this eigenfunction converges towards the nodes surrounding the central hole. The eigenfunction $v_{5,1}^3$ is shown in Figure 3.6. The construction of the eigenfunctions of $-\mathcal{H}_m^0$ corresponding to the eigenvalues 5 or 6 is one of many possible approaches¹.

We now define the map $\Phi(\lambda) = \lambda(5 - \lambda)$ and its inverse

$$\phi_{\pm}(\lambda) = \Phi^{-1}(\lambda) = \frac{5}{2} \left(1 \pm \sqrt{1 - \frac{4}{25}\lambda} \right).$$

¹In a recent publication, Strichartz, [69], outlines an alternative method

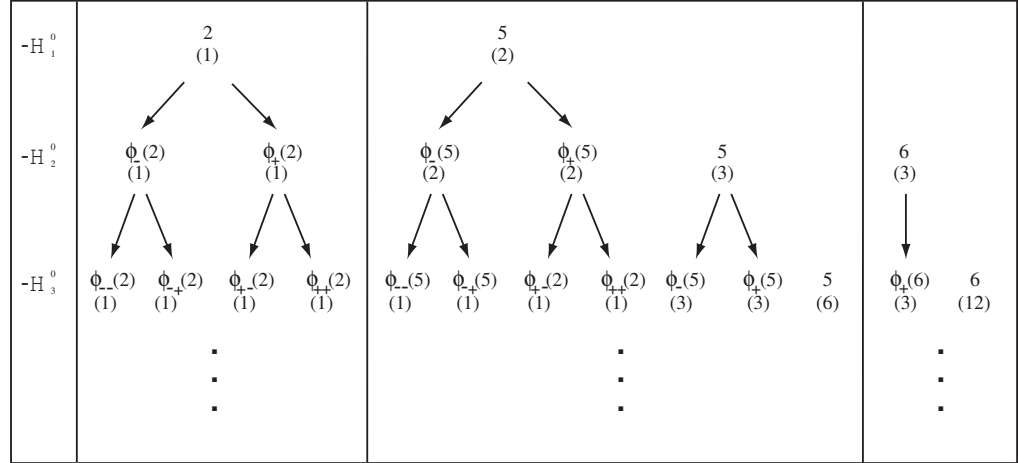


Figure 3.7: The Decimation method used to calculate the eigenvalues (and multiplicities) of $-\mathcal{H}_m^0$.

This, together with Proposition 3.2 leads us to the decimation diagram shown in Figure 3.7. The spectrum of the harmonic difference operator on Γ_6 is shown in Figure 3.8.

In summary, to calculate the eigenvalues and eigenfunctions of $-\mathcal{H}_m^0$, we begin with the Γ_1 approximation to the Sierpinski Gasket. The eigenvalues and eigenfunctions of $-\mathcal{H}_1^0$ are $\mathcal{A}_1 = \{2, 5, 5\}$ and $\{v_k^1\}$, $k = 1, 2, 3$ respectively. Each $v \in \{v_k^1\}$ with eigenvalue $\lambda \in \mathcal{A}_1$ can be extended in two ways, which we shall refer to as the positive and negative extensions v_+ and v_- , to eigenfunctions of $-\mathcal{H}_2^0$. The corresponding eigenvalues are given by $\lambda_+ = \phi_+(\lambda)$ and $\lambda_- = \phi_-(\lambda)$. At vertices $x \in V_1 \cap V_2$ we have $v_{+,-}(x) = v(x)$ and the value of $v_{+,-}(x)$ at vertices $x \in V_2 \setminus V_1$ is obtained by substituting λ_+ or λ_- as appropriate into equation (3.11). By this procedure we obtain six of the twelve eigenfunctions of $-\mathcal{H}_2^0$. The remaining six eigenfunctions correspond to the eigenvalues that are not calculated by the decimation method, the values and multiplicities can be obtained using Proposition 3.3. The corresponding eigenfunctions are constructed using the method outlined earlier in this section.

Once the complete set of eigenvalues and eigenfunctions of $-\mathcal{H}_2^0$ has been com-

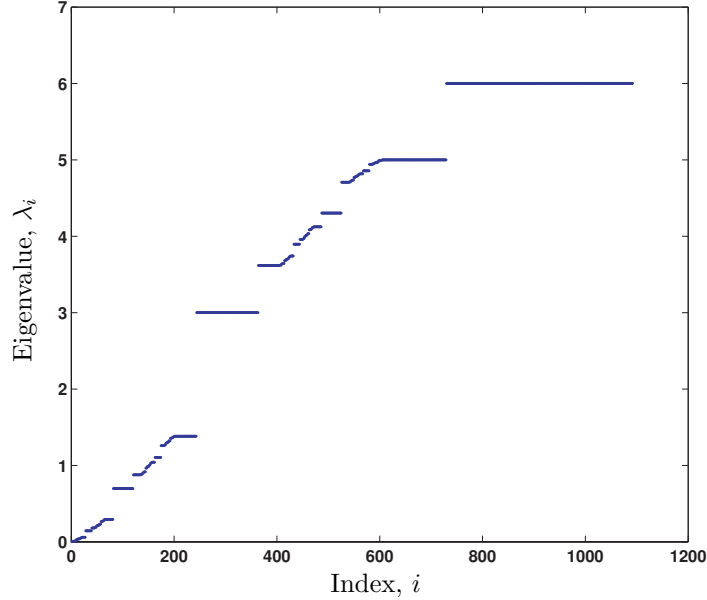


Figure 3.8: The Spectrum of \mathcal{H}_6^0 .

puted we use the same method to extend these eigenfunctions to some of those of $-\mathcal{H}_3^0$. Note that when extending eigenfunctions corresponding to eigenvalue $\lambda = 6$, only the positive extension is taken. The extension of v_1^1 to Γ_6 using ϕ_- each time is shown in Figure 3.9. Figure 3.10 shows one of the three eigenfunctions of $-\mathcal{H}_6^0$ with eigenvalue $(\phi_-(5))^5$, where the power 5 denotes the map ϕ_- composed five times.

3.2.2 Eigenvalues of $-\mathcal{H}_m$ (Neumann Boundary Condition)

We now consider Neumann conditions at the boundary nodes. We begin by defining the following linear operator:

$$(\mathcal{H}_m f)(x) = \begin{cases} (H_m f)(x) & \text{if } x \in V_m \setminus V_0 \\ 2 \sum_{x \sim_m y} (f(y) - f(x)) & \text{if } x \in V_0 \end{cases}. \quad (3.16)$$

Note that, for the boundary vertices, we multiply the corresponding rows in $-\mathcal{H}_m$ by a factor of two. This effectively allows us to treat the boundary vertices as interior vertices (i.e. assuming that every $x \in V_m$ has exactly four neighbours). We can

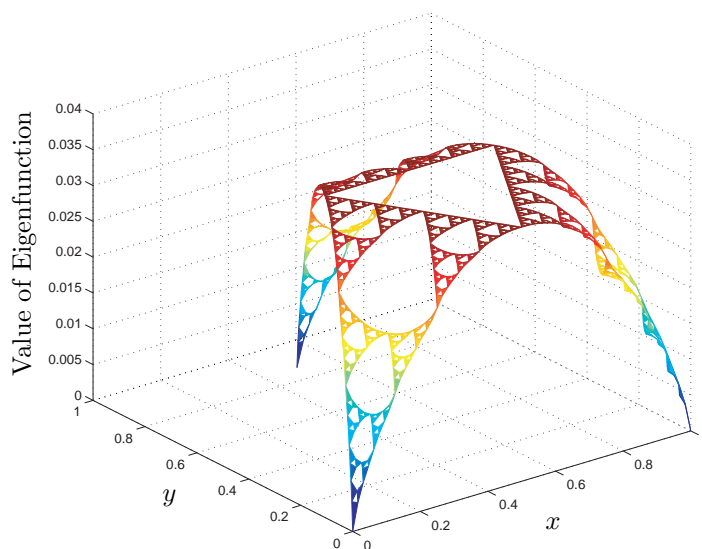


Figure 3.9: The eigenfunction of $-\mathcal{H}_6^0$ with eigenvalue $\lambda = (\phi_-(2))^6$.

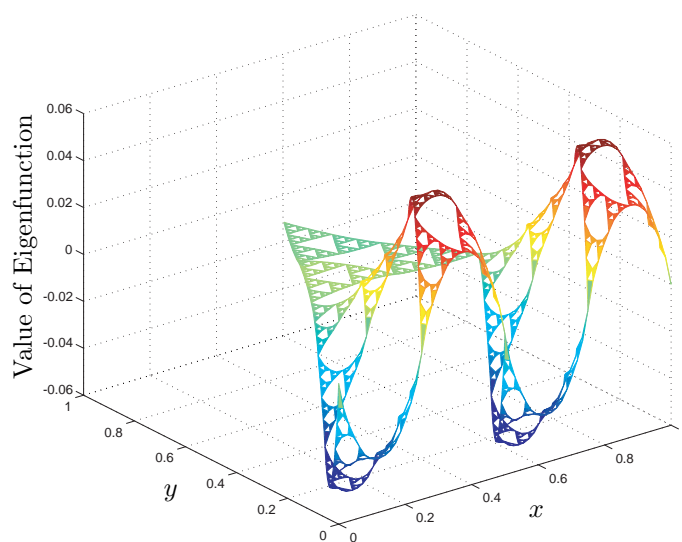


Figure 3.10: An eigenfunction of $-\mathcal{H}_6^0$ with eigenvalue $\lambda = (\phi_-(5))^5$.

therefore use the decimation procedure once again to fully determine the spectrum of \mathcal{H}_m . We denote the set of eigenvalues of $-\mathcal{H}_m$ by \mathcal{B}_m and we see that $\mathcal{B}_1 = \{0, 3, 3, 6, 6, 6\}$. The eigenfunction corresponding to the zero eigenvalue is given by

$$v_1(x) = 1 \quad x \in V_1. \quad (3.17)$$

The eigenvalue 3 corresponds to two eigenfunctions, which are given by

$$v_k(x) = \begin{cases} 1 & x = q_k, \\ -1 & x = q_1, \\ 2 & x = P_1, \\ -2 & x = P_k, \\ 0 & \text{otherwise,} \end{cases} \quad (3.18)$$

for $k = 2, 3$. The eigenvalue 6 corresponds to three eigenfunctions, given by the following function:

$$v_{i,j}(x) = \begin{cases} 1 & x = q_\alpha, \alpha \neq i, j, \\ -1 & x = P_i \text{ or } P_j, \\ 0 & \text{otherwise,} \end{cases} \quad (3.19)$$

where $i, j = 1, 2, 3$, $i < j$. Once again, the eigenvalues and eigenfunctions of $-\mathcal{H}_m$ can be obtained from those of $-\mathcal{H}_{m-1}$ using the decimation method described in Proposition 3.2. As with the Dirichlet case, the decimation procedure does not give the complete spectrum of \mathcal{H}_m . The following proposition accounts for the existence of the remainder of the eigenvalues of \mathcal{H}_m :

Proposition 3.4. *6 is an eigenvalue of $-\mathcal{H}_m$ with multiplicity $\frac{3}{2}\{3^m - 2 \times 3^{m-1} + 1\}$. 5 is an eigenvalue of $-\mathcal{H}_m$ with multiplicity $\frac{3}{2}\{3^{m-1} - 2 \times 3^{m-2} - 1\} + 1$.*

This leads us to the decimation diagram shown in Figure 3.11 which describes the eigenvalues and multiplicities of the eigenvalues of the operator $-\mathcal{H}_m$. The spectrum of $-\mathcal{H}_6$ is shown in Figure 3.12. Once again, eigenvalues and eigenfunction of $-\mathcal{H}_m$ can be found by extending the eigenfunctions of $-\mathcal{H}_1$ as in the Dirichlet case. We

CHAPTER 3: SPECTRUM AND EIGENFUNCTIONS OF THE LAPLACIAN ON THE SIERPINSKI GASKET

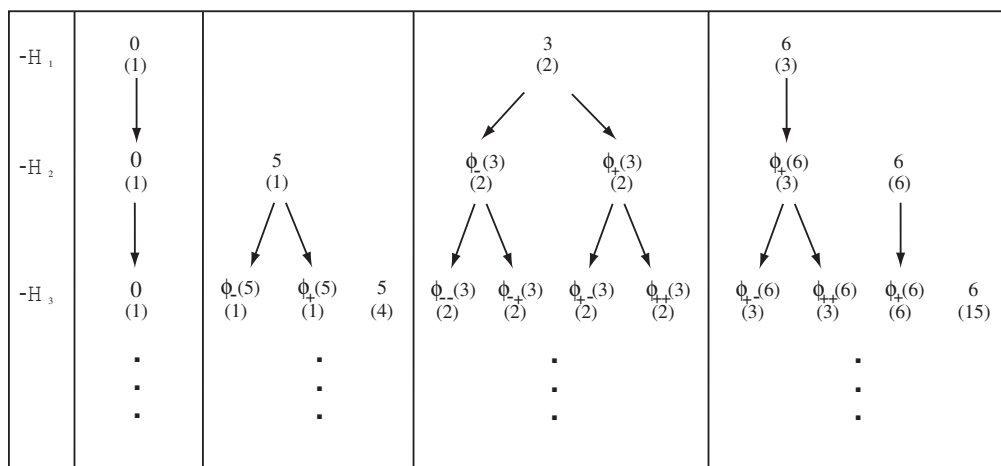


Figure 3.11: The Decimation method used to calculate the eigenvalues (and multiplicities) of $-\mathcal{H}_m$.

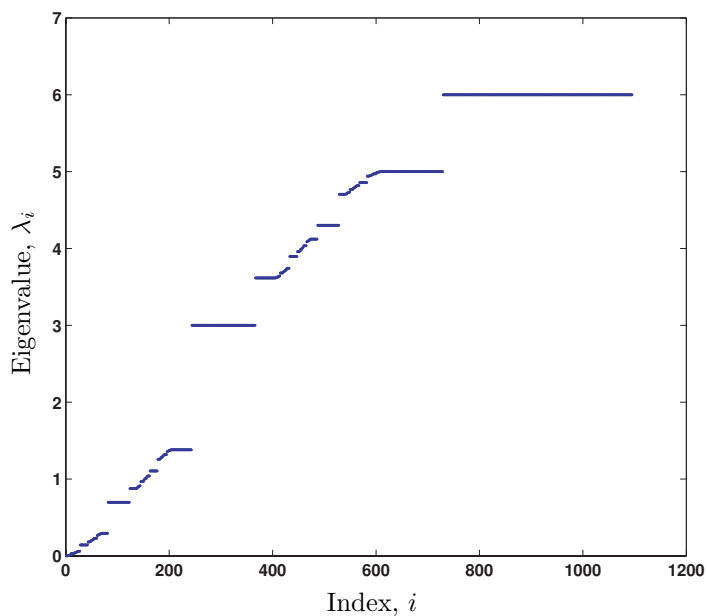


Figure 3.12: The Spectrum of $-\mathcal{H}_6$.

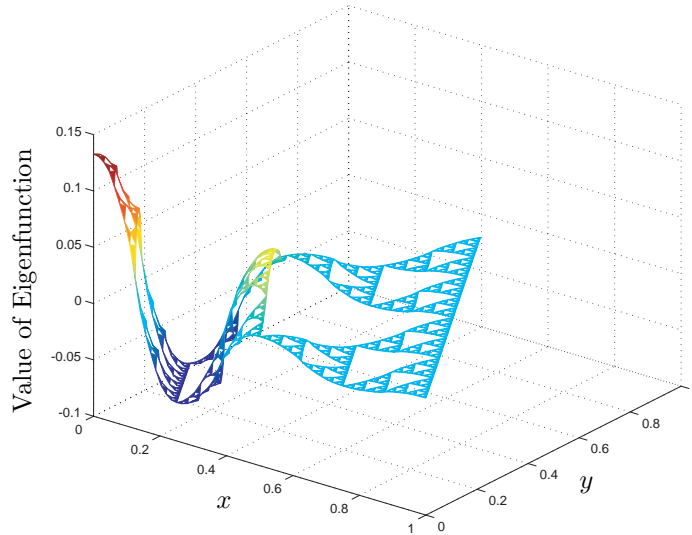


Figure 3.13: An eigenfunction of $-\mathcal{H}_6$ with eigenvalue $\lambda = (\phi_-(\phi_+(6)))^3$.

note that in the Neumann case however, there always exists a constant eigenfunction $v_1^m(x)$ corresponding to the zero eigenvalue. Figures 3.13 and 3.14 show two eigenfunctions of $-\mathcal{H}_6$. The eigenfunction plotted in Figure 3.13 is one of six with eigenvalue $(\phi_-(\phi_+(6)))^3 \approx 0.0289$. The eigenfunction plotted in Figure 3.14 is one of three with eigenvalue $(\phi_-((\phi_+(6))^2))^3 \approx 0.0468$.

3.2.3 Properties of the Eigenvalues of $-\Delta$

We have now considered the spectra of the harmonic difference operators in the cases of both Dirichlet and Neumann boundary conditions. However, when defining the Laplacian on the Sierpinski Gasket, we saw how the graph Laplacians were not related to each other unless they were scaled according to the renormalisation factor $\frac{3}{2}5^m$. Therefore, the spectrum of the Laplacian on the Sierpinski Gasket is the renormalised limit of the spectra of the harmonic differences \mathcal{H}_m^0 or \mathcal{H}_m .

Many properties of the spectrum of the Laplacian on the Sierpinski Gasket have

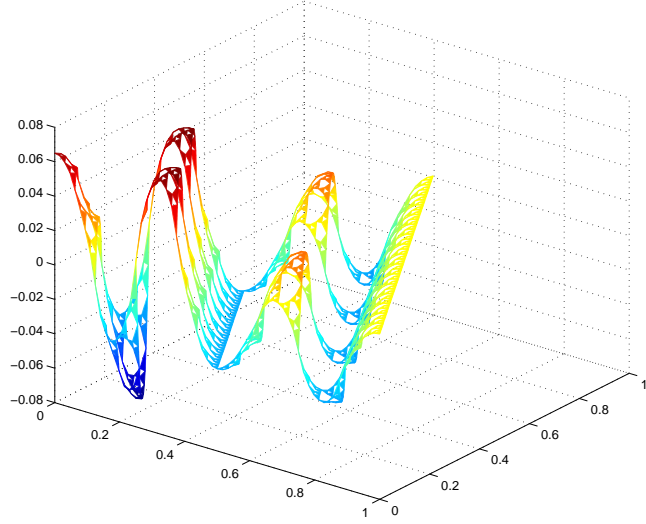


Figure 3.14: An eigenfunction of $-\mathcal{H}_6$ with eigenvalue $\lambda = \left(\phi_-((\phi_+(6))^2)\right)^3$

been described [59, 64, 20], and also for the general case of p.c.f. self-similar sets [49, 46, 65]. In [20] it was shown that for the SG case the eigenvalues of $-\Delta$ are non-negative, of finite multiplicity and the only accumulation point is ∞ in both the Dirichlet and Neumann cases.

In [49] it is proved that there exists $d_s > 0$ such that

$$0 < \liminf_{x \rightarrow \infty} \rho(x)x^{-\frac{d_s}{2}} \leq \limsup_{x \rightarrow \infty} \rho(x)x^{-\frac{d_s}{2}} < \infty, \quad (3.20)$$

where d_s is the spectral exponent ($d_s = \frac{\log 9}{\log 5}$ for the Sierpinski Gasket), and $\rho(x)$ is the eigenvalue counting function or integrated density of states defined by

$$\rho(x) = \#\{k | k \text{ is an eigenvalue of } -\Delta \text{ with } k \leq x\} \quad (3.21)$$

with either Dirichlet or Neumann boundary conditions. Fukushima and Shima [20, 64] showed that for the Sierpinski Gasket, a strict inequality holds in equation (3.20). An analogue of Weyl's theorem for Laplacians on Euclidean spaces has also been established, see [49].

Since in this thesis we are concerned with solving differential equations that model certain biological and physiological processes, the notion of the size of our domain becomes important. So far, we have only approximated the Sierpinski Gasket by a sequence of graphs with no definition of size or length scales. We address this issue here.

Let V_m be the vertex set of the order- m graph approximation to SG. We embed V_m into \mathbb{R}^2 so that each node can be represented in cartesian coordinates by the pair (x, y) . We define $V_m^{(0)}$ to be the vertex set whose boundary points are the vertices of an equilateral triangle with each side having unit length and P_1 is fixed at the origin. Then we define

$$V_m^{(n)} = 2^n V_m^{(0)}, \quad n = 0, 1, 2, \dots \quad (3.22)$$

for $m = 0, 1, 2, \dots$. Then Γ_m is the embedding into \mathbb{R}^2 of the order- m graph approximation to SG, whose side length is 2^n .

In the limit as $m \rightarrow \infty$, we similarly define

$$K(n) = 2^n K, \quad n = 0, 1, 2, \dots \quad (3.23)$$

and

$$K^{(\infty)} = \bigcup_{n=0}^{\infty} K^{(n)}. \quad (3.24)$$

So $K^{(\infty)}$ can be thought of as an infinite Sierpinski Gasket. We also denote by $\Delta_m^{(n)}$ the Laplacian on $V_m^{(n)}$, and similarly $\Delta^{(n)}$ denotes the Laplacian on $K^{(n)}$. From [20], we have the following proposition.

Proposition 3.5. *λ is an eigenvalue of $-\Delta$ ($= -\Delta^{(0)}$) iff $\frac{1}{5^n}\lambda$ is an eigenvalue of $-\Delta^{(n)}$.*

Proposition 3.5 says there is a bijection between the spectra of two differently sized gaskets: as the length of the side of the gasket increases by a factor of 2, the magnitude of the eigenvalues decreases by a factor of 5. We shall assume here that this same scaling relation holds on the finite approximations Γ_m .

3.3 A Problem with \mathcal{H}_m ... and a Solution

When defining the harmonic difference operator with Neumann boundary conditions, we multiplied the rows corresponding to the boundary vertices by a factor of two in order to ensure that the decimation method could be used to calculate the spectrum of \mathcal{H}_m . In this thesis we are interested in the solution of certain partial differential equations formulated with Neumann boundary conditions on the Sierpinski Gasket. A powerful tool for solving such PDEs is that of Fourier analysis, which exploits the orthogonality of eigenfunctions of the Laplacian in Euclidean space. Clearly, the harmonic difference matrix defined in Section 3.2.2 is not symmetric and therefore the eigenfunctions of $-\mathcal{H}_m$ do not form an orthogonal set.

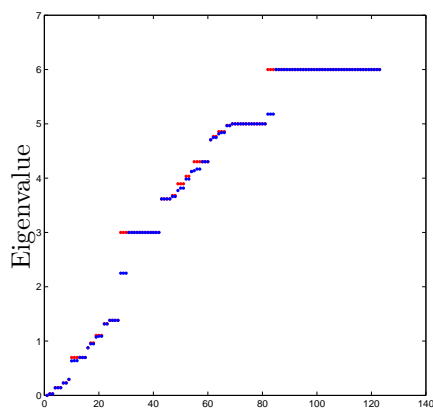
Let us now define the following harmonic difference operator with Neumann boundary conditions on the Sierpinski Gasket:

$$(\mathcal{H}_m^N f)(x) = \begin{cases} (H_m f)(x) & \text{if } x \in V_m \setminus V_0 \\ \sum_{x \sim_m y} (f(y) - f(x)) & \text{if } x \in V_0 \end{cases}. \quad (3.25)$$

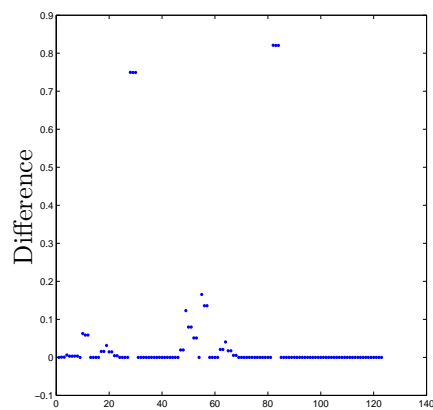
From a physical point of view the harmonic difference operators defined in equations (3.16) and (3.25) do not differ. Their spectra and eigenfunctions however are not identical. Since \mathcal{H}_m^N is a symmetric matrix, its eigenfunctions will be orthogonal. There is a disadvantage in that we cannot use the decimation procedure to determine the spectrum of \mathcal{H}_m^N . This must be computed numerically.

The spectra of \mathcal{H}_m and \mathcal{H}_m^N and the difference between the eigenvalues are shown in Figure 3.15. We see that in the limit as $m \rightarrow \infty$ the two spectra appear to converge apart from in certain areas, where the difference remains constant. This result is disappointing since we would like the advantage of being able to calculate the spectrum via the decimation method and to have an orthogonal set of eigenfunctions when carrying out numerical simulations.

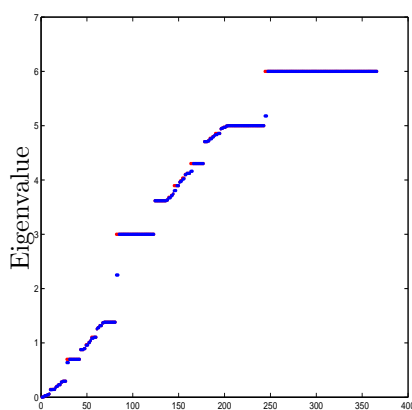
A way around this problem is to introduce the notion of a fractafold. A fractafold, which is the fractal analogue of the concept of a manifold in Euclidean space, was



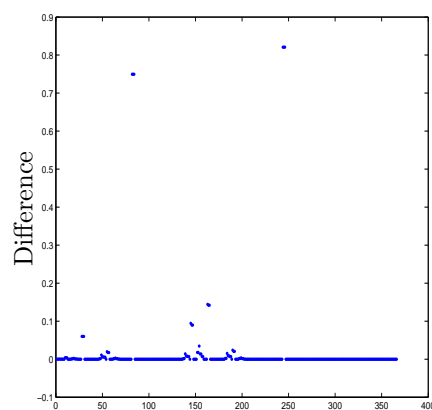
(a) The spectra of \mathcal{H}_4 (red) and \mathcal{H}_4^N (blue).



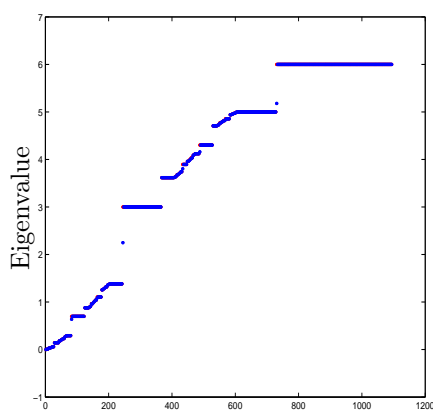
(b) The absolute value of the difference between \mathcal{H}_4 and \mathcal{H}_4^N .



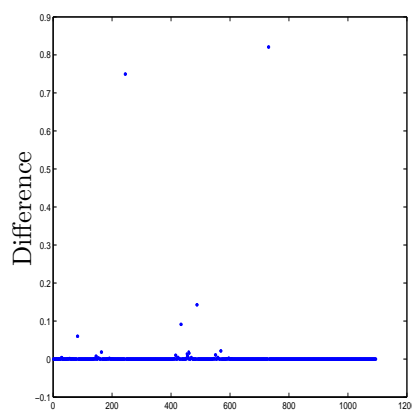
(c) The spectra of \mathcal{H}_5 (red) and \mathcal{H}_5^N (blue).



(d) The absolute value of the difference between \mathcal{H}_5 and \mathcal{H}_5^N .



(e) The spectra of \mathcal{H}_6 (red) and \mathcal{H}_6^N (blue).



(f) The absolute value of the difference between \mathcal{H}_6 and \mathcal{H}_6^N .

Figure 3.15: The difference between the spectra of \mathcal{H}_m and \mathcal{H}_m^N , for $m = 4, 5, 6$.

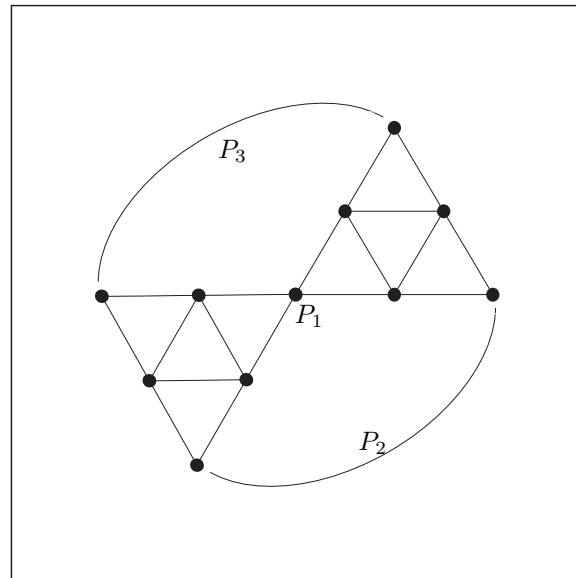


Figure 3.16: The second order approximation to the double of SG.

introduced by Strichartz [67]. We consider a specific example of a fractafold based on the Sierpinski Gasket known as the double of SG, see Figure 3.16. The double of SG consists of two copies of SG that are glued together at the three boundary points. We can construct a harmonic difference operator on the double of SG in exactly the same manner as we have done for the Sierpinski Gasket. In the fractafold case, we have the advantage that every vertex is now a true interior vertex with exactly four neighbours so the decimation method can be used to determine the spectrum and, since the harmonic difference operator is symmetric, the eigenfunctions do indeed form an orthonormal basis.

3.4 Localised Eigenfunctions of the Laplacian on the Sierpinski Gasket

The eigenvalues and eigenfunctions of the Laplacian on the Sierpinski Gasket are quite different from those of Laplacians on Euclidean domains. In particular, there

exist localised eigenfunctions: a non-zero eigenfunction which vanishes on some open subset of the gasket. The existence of localised eigenfunctions of the Laplacian on the Sierpinski Gasket was first suggested by Rammal and Toulouse [60]. Here, we summarise the basic results, see [7] or Chapter 4 in [48] for a detailed description in the case of general p.c.f. self-similar sets.

We begin by defining the notion of a pre-localised eigenfunction.

Definition 3.6. *A function u is called a pre-localized eigenfunction of $-\Delta$ if u is an eigenfunction of $-\Delta$ and u satisfies both Dirichlet and Neumann boundary conditions (u is a DN-eigenfunction) for some eigenvalue λ .*

For the case of SG, it is easy to find DN-eigenfunctions. In fact every eigenfunction of the harmonic difference operator $-\mathcal{H}_m^0$ with eigenvalue equal to 6 or a descendent of 6 under the map ϕ satisfies Dirichlet-Neumann conditions. We then have the following Lemma:

Lemma 3.7. *For $w \in W_*$, define u_w by*

$$u_w(x) = \begin{cases} u(f_w^{-1}(x)) & x \in K_w \\ 0 & \text{otherwise} \end{cases}.$$

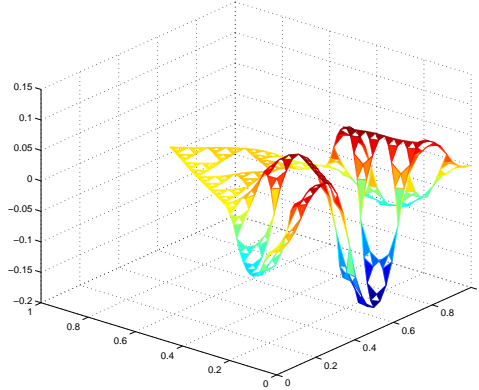
If u is a pre-localised eigenfunction of $-\Delta_m$ with eigenvalue λ , then u_w is an eigenfunction of $-\Delta_{m+|w|}$ with eigenvalue $5^{|w|}\lambda$ and support in K_w .

Lemma 3.7 says that given a pre-localised eigenfunction on Γ_m (clearly we must have $m \geq 2$) we can construct a localised eigenfunction on Γ_{m+n} for any $n \geq 1$ whose support is confined to an order n subset of our graph.

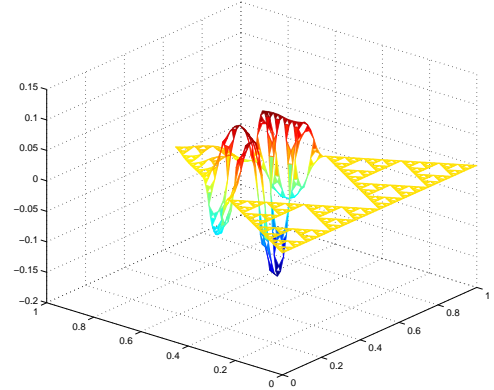
As an example, let us consider the eigenfunctions of $-\Delta_5^0$. The first DN-eigenfunction we arrive at corresponds to the eigenvalue

$$\lambda = \frac{3}{2} \times \phi_-^{(3)}(\phi_+(6)) \approx 673.125.$$

This is our pre-localised eigenfunction u . To construct a localised eigenfunction on Γ_6 , we choose one of the maps of our IFS, in this case we choose f_3 , so the support



(a) The pre-localised eigenfunction on Γ_5 .



(b) The localised eigenfunction on Γ_6 .

Figure 3.17: The extension of a pre-localised eigenfunction on Γ_5 to Γ_6 under the map f_3 .

of our localised eigenfunction will be those nodes $x \in V_6$ whose address begins with a 3, and the value of our localised eigenfunction at these nodes will be precisely the value of u at the pre-image of x under f_3 . This is shown in Figure 3.17.

In [47], Kigami divided the eigenvalue counting function into two parts. He let $\rho^W(x)$ denote the eigenvalue counting function corresponding to the localised eigenfunctions and $\rho^F(x)$ denote the eigenvalue counting function corresponding to the non-localised eigenfunctions. It was found that as $x \rightarrow \infty$, $\rho^W(x) \approx x^{\frac{d_s}{2}}$, whereas $\rho^F(x) \approx x^{\kappa_F}$, where $\kappa_F < \frac{d_s}{2}$. The localised eigenvalues therefore dominate.

Localised eigenvalues also have physical implications in that there are solutions to the heat or wave equation on the Sierpinski Gasket whose support remains in a small part of the gasket.

Chapter 4

The Cable Equation

4.1 Introduction

The human brain is the most complex structure known to man. All of our movements, thoughts and abilities are determined by this organ, so it is no surprise that its extraordinary anatomy and properties are the focus of the research of many scientists. We focus here on the building block of the brain: the nerve cell, or neuron. We are interested in how electrical signals propagate along sequences of such cells. To be able to understand this process we must first familiarise ourselves with the structure and physical properties of individual nerve cells. A neuron consists, as almost all cells do, of a cell body (or soma) and a nucleus that contains all the genetic information of the cell. However, the structure of a neuron is tailored to aid its function by means of two additions: the axon is a long cylindrical extension of the neuron which transmits electrical signals away from the cell, and the dendritic tree which extends out from the nerve cell to receive signals from impinging axons.

Neurons are an example of excitable cells and exhibit threshold behaviour. Under rest conditions the neuron remains at a roughly constant rest state. If a weak stimulus is applied, the cell is briefly disturbed but quickly returns to the rest state. If a stronger, super-threshold stimulus is applied the neuron's state undergoes a large

excursion before returning to the rest state.

Remarkably accurate mathematical models have been devised as a result of well-developed experimental techniques and good experimental data. In this and the next chapter, we shall consider the question how do potentials spread in a dendritic tree or an axon? There have been many mathematical models developed in answer to this question, which range greatly in their detail and accuracy. In [70], Tuckwell describes and analyses the principle mathematical models that have been developed for neurons.

The simplest models capable of predicting the quantitative behaviour of nerve cells are known as single compartment or point neuron models. This type of model was introduced by Lapicque in 1907 and considers the whole cell by a single representative circuit. The problem with this kind of model is that we cannot address questions concerning the effects of input position or the interaction between inputs at various points on the surface of the cell. We are also unable to see how the branching point in the dendritic tree or axon affects the integration of an input. So, rather than considering a neuron as a single lumped circuit, we model the dendritic or axonal branches as long, cable-like structures. It is for this reason that we call the mathematical analysis of how impulses propagate along this type of structure in neurons cable theory.

The application of cable theory to dendritic neurons began when scientists who had been researching into nerve function found it necessary to interpret the experimental data obtained from individual neurons. Originally the cable equation was applied to the conduction of potentials in an axon by Hodgkin and Rushton in 1946 [34] and it was later applied to dendritic trees in neurons by Rall in 1962 [58]. Cable theory is concerned with how synaptic inputs propagate from the dendritic tree to the soma, how these inputs interact with one another and how the placement of an input on a dendritic tree affects its functional importance to the neuron. Since the structures concerned are so narrow in comparison to their length, variations in the membrane

potential in the radial direction are negligible compared to those in the axial direction and so we can measure the membrane potential as a function of two variables only: the distance along the cable x and time t . We wish to solve our problem for the membrane potential V . It is important to note here that cable theory only realistically models passive processes in neurons where the input currents are neither large enough nor close enough together to cause an action potential to fire.

4.2 Derivation of the Cable Equation

4.2.1 Definition of Parameters

In order to derive the cable equation, we assume that the neuronal cable is a uniform cylinder, of radius a , of conducting fluid (axoplasm), separated from the external medium (which also has conducting properties) by the cell membrane. The membrane itself has an electrical resistance and capacitance. The cable is split up into compartments or segments of infinitesimal length as shown in Figure 4.1. We will assume that the following three types of current occur:

1. Current flow through the cell membrane. This is split into contributions from the capacitance and the conducting properties of the membrane, I^c and I^M respectively and we must remember that, by convention, membrane currents are defined to be positive outwards (as opposed to currents from an electrode, which are positive inwards).
2. Current flow in the axial direction along the interior of the segment, I .
3. Current flow in the axial direction along the exterior of the segment. It does not affect our derivation if we ignore this current. So, for simplicity, we will set this to zero.

We now go on to define some important membrane parameters.

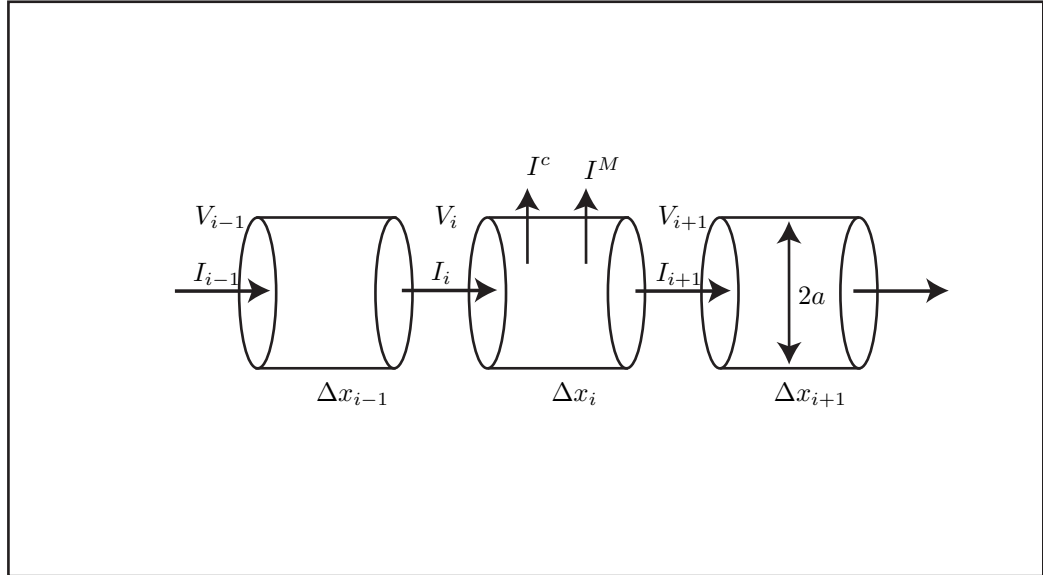


Figure 4.1: This figure shows three segments of our neuronal cable, length Δx , radius a , along with the currents we shall be considering.

- The axial current along the interior of the segment is subject to a resistance known as the Specific Axial Resistance R_L . This is the resistance to current flowing along a 10mm long segment of cable with a 10mm² end surface area. The inverse of this quantity is the Specific Axial Conductance, denoted by G_L .
- There is also a resistance to the current flowing through the neuronal membrane. This is known as the Specific Membrane Resistance R_M and is defined to be the resistance of a 10mm² patch of membrane. The inverse of R_M is G_M , the Specific Membrane Conductance.
- We must also consider the capacitance of the membrane. The Specific Membrane Capacitance, C_M is defined to be the capacitance of a 10mm² patch of membrane and is usually treated as constant.

Now that we have defined these specific membrane parameters, we can define their counterparts for our segment of cable.

Specific Membrane Capacitance	$C_M \simeq 10\text{nF}/\text{mm}^2$
Radius of Cable	$a \simeq 2\mu\text{m}$
Specific Axial Resistance	$1\text{K}\Omega\text{mm} \leq R_i \leq 3\text{K}\Omega\text{mm}$
Specific Membrane Resistance	$1\text{M}\Omega \leq R_m \leq 10\text{M}\Omega$

Table 4.1: Typical Values for the Specific Membrane Parameters

- The axial resistance of our segment will be R_L multiplied by the length of the segment Δx and divided by the cross-sectional area, so we have

$$r_L = \frac{\Delta x}{\pi a^2} R_L \quad \text{and} \quad g_L = \frac{\pi a^2}{\Delta x} G_L.$$

We see that these definitions make sense because increasing the cross-sectional area will increase the conductance, while increasing the length of the segment will reduce it.

- The resistance and conductance across the membrane will be proportional to the surface area of the segment, provided that we assume that the ion channels are evenly distributed over the surface of the segment. Therefore, the larger the surface area, the higher the conductance. This gives us our definitions for the membrane resistance and conductance:

$$r_M = \frac{R_M}{2\pi a \Delta x} \quad \text{and} \quad g_M = 2\pi a \Delta x G_M$$

- Similarly, the total membrane capacitance is also proportional to the surface area of the segment and so we have membrane resistance and conductance:

$$c_M = 2\pi a \Delta x C_M.$$

For biologically realistic neurons, Table 4.1 gives appropriate values. The values for the Specific Membrane Resistance vary considerably for different neurons and for different excitation levels and times within a single cell.

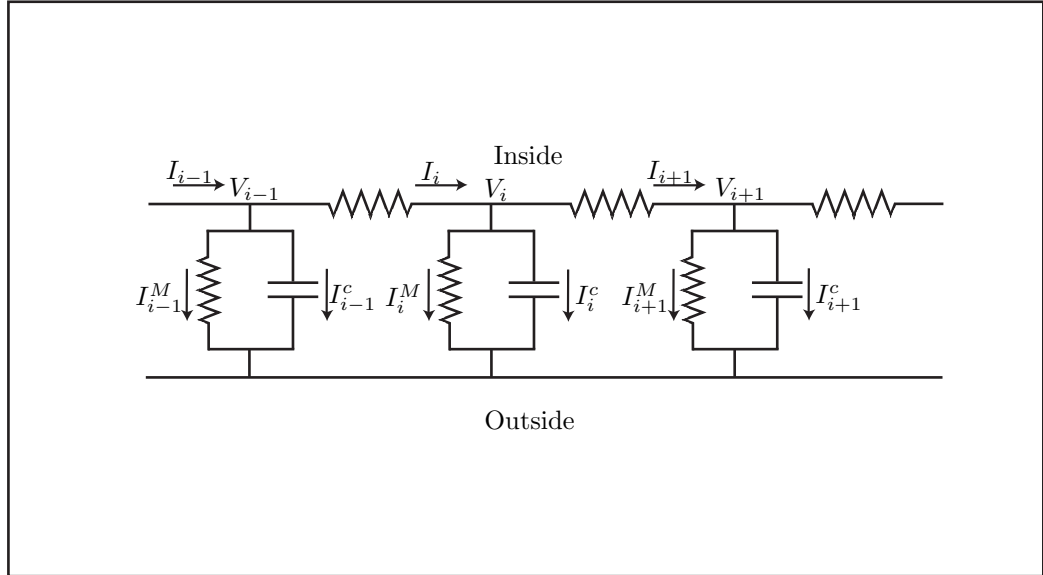


Figure 4.2: The equivalent electrical circuit to Figure 4.1.

4.2.2 Derivation of the Cable Equation

To derive the cable equation, focus on the central segment of cable in Figure 4.1 and consider the current flow between this segment and its two neighbours and the external medium. The point where two or more segments meet is called a node and we say that the length of the segment of cable beginning at node i is Δx_i and the current entering this segment from the previous segment in the axial direction is I_i . The membrane potential at node i is defined to be V_i . The equivalent circuit to Figure 4.1 is shown in Figure 4.2.

The voltage at node i is given by Ohm's law, which tells us

$$V_i = V_{i-1} - I_i r_L = V_{i-1} - I_i \frac{R_L \Delta x_i}{\pi a^2} \quad (4.1)$$

so that

$$\Delta V_i = V_i - V_{i-1} = -I_i \frac{R_L \Delta x_i}{\pi a^2}. \quad (4.2)$$

We can rearrange (4.2) and take the limit as $\Delta x_i \rightarrow 0$ to give us the expression for

the axial current I_i :

$$I_i = -\frac{\pi a^2}{R_L} \frac{\partial V_i}{\partial x_i}. \quad (4.3)$$

We now apply Kirchoff's Current Law at node i , which says that the current entering a node must equal the current leaving the node. This yields

$$I_i = I_i^M + I^c + I_{i+1} \quad (4.4)$$

and, similarly

$$\Delta I_i = I_{i+1} - I_i = -I_i^M - I^c. \quad (4.5)$$

Again, using Ohm's law and the time derivative of the equation for a capacitor we can write

$$-I_i^M = -\frac{V_i}{r_M} = -2\pi a \Delta x_i \frac{V_i}{R_M} \quad (4.6)$$

and

$$-I^c = -c_M \frac{\partial V_i}{\partial t} = -2\pi a \Delta x_i C_M \frac{\partial V_i}{\partial t}, \quad (4.7)$$

which, when substituted into 4.5 gives us

$$\frac{\Delta I_i}{\Delta x_i} = -2\pi a \frac{V_i}{R_M} - 2\pi a C_M \frac{\partial V_i}{\partial t}. \quad (4.8)$$

In the limit as $\Delta x_i \rightarrow 0$ (4.8) gives us an expression for the spatial derivative of the axial current at node i

$$\frac{\partial I_i}{\partial x_i} = -2\pi a \left(\frac{V_i}{R_M} + C_M \frac{\partial V_i}{\partial t} \right). \quad (4.9)$$

We can obtain an equivalent expression for this derivative by differentiating (4.3) with respect to x_i . This is

$$\frac{\partial I_i}{\partial x_i} = -\frac{\pi a^2}{R_L} \frac{\partial^2 V_i}{\partial x_i^2}. \quad (4.10)$$

Equating equations (4.9) and (4.10) then gives us

$$\frac{\partial^2 V_i}{\partial x_i^2} = \frac{2R_L}{a} \left(\frac{V_i}{R_M} + C_M \frac{\partial V_i}{\partial t} \right). \quad (4.11)$$

Here we have assumed that the radius of the cable a is independent of x . Finally, multiplying (4.11) through by $\frac{aR_M}{2R_L}$ and dropping the nodal subscripts yields the cable equation

$$\frac{aR_M}{2R_L} \frac{\partial^2 V}{\partial x^2} = V + R_M C_M \frac{\partial V}{\partial t}. \quad (4.12)$$

4.2.3 Space and Time Constants

The product $R_M C_M$, which multiplies the time derivative on the right hand side of (4.12) is a quantity with units of time, called the membrane time constant, $\tau_M = R_M C_M$. The membrane time constant is independent of area (since R_M and C_M have reciprocal dependencies on the surface area of the membrane) and sets the basic timescale for changes in the membrane potential. We can see that this is the case if we suppose that our segment of cable is space-clamped at uniform voltage V_0 at time $t = t_0$, so that $\frac{\partial^2 V}{\partial x^2} = 0$. In this case, the distribution of voltage along the cable remains uniform for all time following the release of the voltage-clamp, and the cable equation (4.12) reduces to

$$V + \tau_M \frac{dV}{dt} = 0. \quad (4.13)$$

This linear first order ODE, together with the initial condition $V(t_0) = V_0$ is easily solved to give the solution

$$V(t) = V_0 \exp\left(-\frac{1}{\tau_M} (t - t_0)\right). \quad (4.14)$$

We see that in this case the potential decays exponentially with time constant τ_M at every point along the cylinder following the release of the voltage-clamp.

The constant $\frac{aR_M}{2R_L}$ in equation (4.12) also has a physical interpretation. If we think about applying a constant trans-membrane current at some point on our segment of cable. Then, after sufficiently long time the voltage will become a function of the axial distance, x , only and $\frac{\partial V}{\partial t} \rightarrow 0$. This corresponds to a steady state, and at this steady state the PDE (4.12) reduces to the ODE

$$\frac{aR_M}{2R_L} \frac{d^2 V}{dx^2} = V, \quad (4.15)$$

the general solution of which is given by

$$V = A \exp\left(\sqrt{\frac{2R_L}{aR_M}}x\right) + B \exp\left(-\sqrt{\frac{2R_L}{aR_M}}x\right). \quad (4.16)$$

The constants A and B in (4.16) are determined by the boundary conditions. The simplest case to consider is that of an infinite cable, extending from $-\infty$ to $+\infty$. Let's assume that at $x = 0$, the voltage is clamped to $V = V_0$. In this case we require

$$V(-\infty) = V(+\infty) = 0$$

and thus for $x \geq 0$ we have $A = 0$ and $B = V_0$. Similarly, for $x \leq 0$ we have $A = V_0$, $B = 0$. We define by

$$\lambda = \sqrt{\frac{aR_M}{2R_L}} \quad (4.17)$$

the electrotonic length of a cable of radius a . So, in the case of an infinite cable, the general solution of equation (4.15) is given by

$$V(x) = V_0 e^{-\frac{|x|}{\lambda}}. \quad (4.18)$$

It is now clear why λ is called a length-constant, it determines the voltage attenuation with distance: λ is the distance along a cable at which a constant applied voltage will decay to $\frac{1}{e}$ of its original value.

Expressed in terms of the space and time constants τ_M and λ , the linear cable equation becomes

$$\lambda^2 \frac{\partial^2 V}{\partial x^2} = V + \tau_M \frac{\partial V}{\partial t}. \quad (4.19)$$

4.3 The Solution of the Cable Equation on the Sierpinski Gasket

The structure of dendrites is extremely complex, consisting of (often several) complicated trees. It therefore seems natural to model this complex structure as a fractal

and use this as our domain on which to solve the cable equation. We are, however, limited in our choice of fractal domain as the theory of analysis on fractals has thus far only been developed in the case of p.c.f. self-similar sets. Ultimately a p.c.f. fractal tree such as Hata's tree-like set would be an excellent choice to model a dendrite. However, the application of the formalism described in previous chapters to the Hata Tree seems to miss important features that might be expected to hold for a reasonable model. These limitations appear to be such that we lose nothing by working with the Sierpinski Gasket and so we shall use this as our complex domain on which to solve the cable equation. In this section we shall solve equation (4.19) on the Sierpinski Gasket.

Our purpose here will be relatively straightforward. The cable equation is a linear, dissipative dynamical system where the dissipation is due to transmembrane effects as well as axial resistance. From an engineering point of view we might study such a system by looking at its response to a sharp temporal pulse. (There is a huge literature on this (see [13])– however mathematically this is essentially a way to compute the Green's function for the system.) So, in this chapter we consider the cable equation on the Sierpinski Gasket as a linear input/output system by applying a sharp pulse near to one boundary point of the gasket, and observing the response near the other boundary points. We shall do this for Dirichlet (voltage-clamped) and Neumann (zero current flow at the boundaries) boundary conditions – this will allow us to distinguish some of the effects of membrane dissipation and axial dissipation.

We shall be interested in finding numerical results which are independent of the graphical approximation to the Sierpinski Gasket. We shall use the correctly scaled Laplacian discussed earlier – however the spatial form of the input spike is something that we must deal with. Naïvely, we might imagine constructing a spatial delta function to represent spatial localisation of the input spike. Here, however, we shall do something very simple – we shall apply an initial stimulus of magnitude 1 to the vertices neighbouring the boundary point P_1 . If we imagine how this projects onto

the eigenfunctions of the Laplacian, we can understand that this will change as the order of the graphical approximation changes. The following will be an investigation of how to find behaviour which becomes independent of the graphical approximation – we do this by finding a way to scale the magnitude of the input spike.

4.3.1 Dirichlet Boundary Conditions

Let us now consider the discrete cable equation on the Sierpinski Gasket

$$\lambda^2 \Delta_m^0 \mathbf{V}^m = \mathbf{V}^m + \tau_M \frac{\partial \mathbf{V}^m}{\partial t}, \quad (4.20)$$

where \mathbf{V}^m is a vector containing the value of the voltage at the vertices of Γ_m . We are interested in the solution to equation (4.20) subject to Dirichlet boundary conditions where the initial condition takes the form of a stimulus, amplitude 1, applied at the two neighbours of the boundary point P_1 . We fix the voltage to be zero at the boundary nodes so that current can flow out from these nodes. We can write the solution to (4.20) in the form

$$\mathbf{V}^m = \sum_j c_j(t) \mathbf{F}_j^m, \quad (4.21)$$

where the \mathbf{F}_j^m s are solutions to the discrete eigenvalue problem on Γ_m ,

$$\Delta_m^0 \mathbf{F}_j^m + k_j^m \mathbf{F}_j^m = 0, \quad (4.22)$$

subject to Dirichlet boundary conditions, and the c_j s are time-dependent constants given by

$$c_j(t) = \mathbf{F}_j^m \cdot \mathbf{V}^m(t). \quad (4.23)$$

Substituting (4.21) into (4.20) we see that the c_j s satisfy the following first order ODE:

$$\frac{dc_j}{dt} = -\frac{1}{\tau_M} (\lambda^2 k_j^m + 1) c_j, \quad (4.24)$$

the solution of which is given by

$$c_j(t) = c_j(0) \exp\left(-\frac{(\lambda^2 k_j^m + 1)}{\tau_M} t\right). \quad (4.25)$$

We can therefore write the solution to the discrete cable equation (4.20) as:

$$\mathbf{V}^m = \sum_j c_j(0) \exp\left(-\frac{(\lambda^2 k_j^m + 1)}{\tau_M} t\right) \mathbf{F}_j^m. \quad (4.26)$$

All the eigenvalues k_j^m are positive so the solution will decay exponentially. The Fourier mode corresponding to the smallest eigenvalue will decay at the slowest rate so, assuming a generic initial condition, after a sufficiently long time, we expect the solution of the cable equation to be of the form of the ground state Dirichlet eigenfunction of $-\Delta_m^0$ (see Figure 3.9).

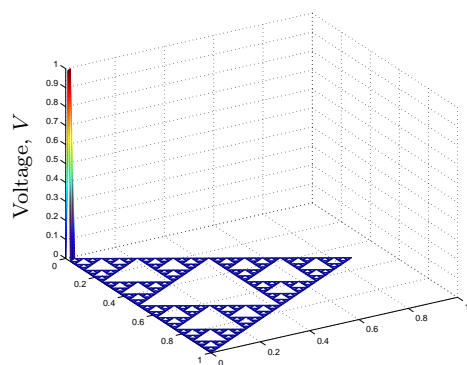
We solve equation 4.20 on Γ_m using a suitable numerical scheme (the solutions presented here were obtained using the Matlab solver ode23, which uses an explicit Runge-Kutta method). For all numerical calculations the values for the time and length constants are chosen to be $\tau_M = 10$ and $\lambda^2 = \frac{1}{3}$. The numerical solution when equation (4.20) is solved on Γ_6 along with the initial condition is shown in Figure 4.3. We note that in Figure 4.3(d), the solution of the cable equation is of the form of the ground state Dirichlet eigenfunction. This form, however, is only apparent on a small scale due to the current flowing out at the boundary nodes and the cell membrane.

How does the level of approximation to the Sierpinski Gasket affect the solution of cable equation on SG? To see this, we solved equation (4.20) on Γ_m , $m = 3, 4, 5, 6$ where in each case the initial condition is a stimulus, amplitude 1, applied at the two neighbours of the boundary node P_1 . The average voltage of the neighbours of the other boundary points P_2 and P_3 was then observed and is plotted against time in Figure 4.4. We notice that as the order of our graph approximation increases, the voltage attained at the neighbours of the boundary points P_2 and P_3 decreases.

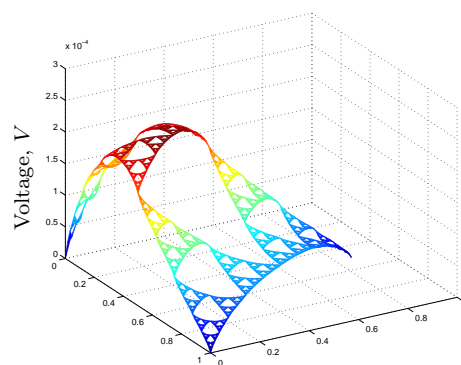
To investigate this we consider the form of the solution of equation (4.20), which after a sufficiently long time is given by

$$\mathbf{V}^m(t) = c_1(0) \exp\left(-\frac{\lambda^2 k_1^m + 1}{\tau_M} t\right) \mathbf{F}_1^m, \quad (4.27)$$

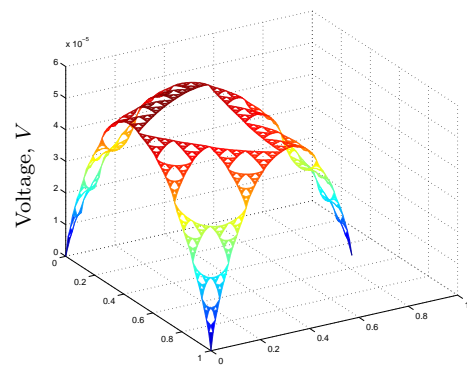
where \mathbf{F}_1^m is the eigenfunction of $-\Delta_m^0$ with the smallest eigenvalue k_1^m . We are interested in the average voltage of the two neighbours of P_2 (or P_3), given an ini-



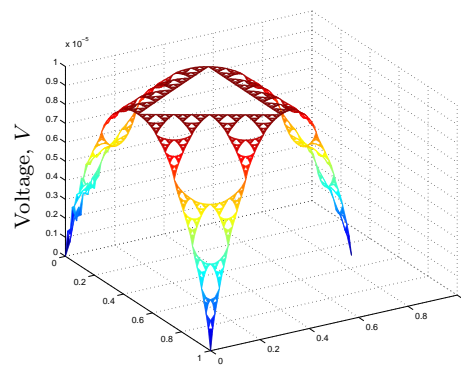
(a) $t = 0$



(b) $t = 0.1$



(c) $t = 0.25$



(d) $t = 0.5$

Figure 4.3: The solution of the discrete cable equation (4.20) on Γ_6 with Dirichlet boundary conditions.

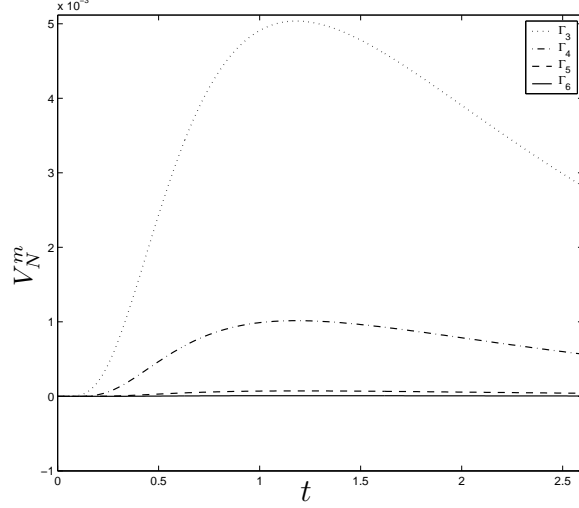


Figure 4.4: The average voltage of the neighbours of the boundary point P_2 obtained by solving the cable equation with Dirichlet boundary conditions, subject to an initial stimulus, amplitude 1, at the neighbours of the boundary point P_1 .

tial stimulus applied at the two neighbours of P_1 . Due to symmetry, the value of the ground state Dirichlet eigenfunction is equal at all the neighbours of the three boundary points, we call this value $F_1^m(N)$. Similarly we let $V_N^m(t)$ denote the average voltage of the two neighbours of P_2 at time t . From (4.23) we see that $c_1(0) = 2F_1^m(N)$ and we therefore write

$$V_N^m = 2F_1^m \exp\left(-\frac{\lambda^2 k_1 + 1}{\tau_M} t\right) F_1^m \quad (4.28)$$

$$= 2\left(F_1^m(N)\right)^2 \exp\left(-\frac{\lambda^2 k_1^m + 1}{\tau_M} t\right), \quad (4.29)$$

so

$$\ln V_N^m = \ln 2\left(F_1^m(N)\right)^2 - \frac{\lambda^2 k_1^m + 1}{\tau_M} t = C_m - a_m t. \quad (4.30)$$

Figure 4.5 shows $\ln V_m$ against time for the tails of the plots in Figure 4.4 for different order approximations to the gasket and, as expected from equation (4.30), we see four straight lines that appear to be parallel and equally-spaced. The gradient of the lines in Figure (4.5), given by $-a_m$ is in fact independent of m since as m increases, the

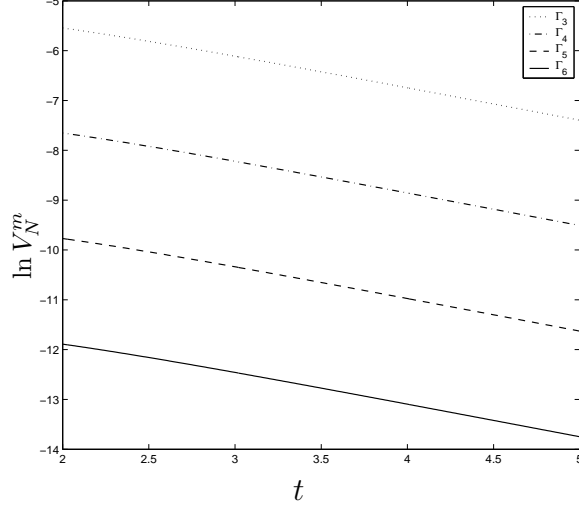


Figure 4.5: A log plot of the the average voltage of the neighbours of the boundary point P_1 against time.

value of k_1^m tends to a constant ≈ 16.816 . The fact that $a_m \rightarrow a$ as m increases accounts for the lines being parallel.

The intercept of the lines in Figure 4.5, given by C_m , however does depend on the order of approximation. We have

$$C_m = \ln 2 \left(F_1^m(N) \right)^2 = \ln 2 + 2 \ln F_1^m(N) \quad (4.31)$$

and so we would like to know how $F_1^m(N)$ changes with m . As m increases, we find that the ratio between $F_1^{m-1}(N)$ and $F_1^m(N)$ approaches $\frac{5}{\sqrt{3}}$. Then for large enough m , we have

$$F_1^m(N) \approx \frac{\sqrt{3}}{5} F_1^{m-1}(N) \quad (4.32)$$

and therefore

$$F_1^m(N) \approx A \left(\frac{\sqrt{3}}{5} \right)^m, \quad (4.33)$$

where calculation shows that $A \approx e^{-0.3094}$. This gives us the following expression for C_m :

$$C_m \approx \ln(2A^2) + m \ln \left(\frac{3}{25} \right). \quad (4.34)$$

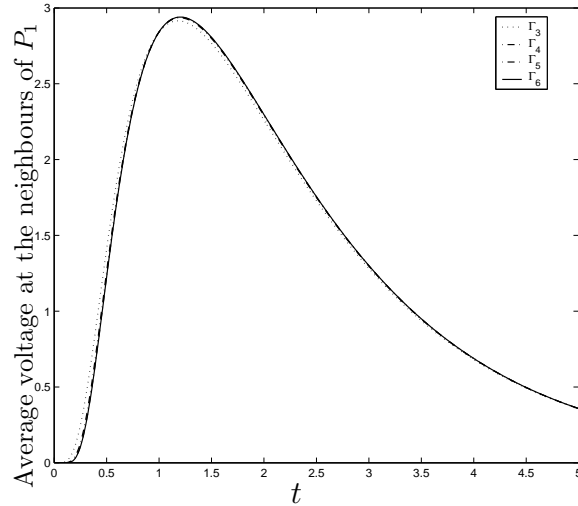


Figure 4.6: Here, the input is scaled by a factor of $\left(\frac{25}{3}\right)^m$, and we see that the output is now independent of the level of approximation of the gasket

By considering the difference between C_{m-1} and C_m we find that the distance between neighbouring lines in Figure 4.5 is $\ln\left(\frac{25}{3}\right)$ and

$$C_m \approx C_{m-1} - \ln\left(\frac{25}{3}\right) = C_0 - m \ln\left(\frac{25}{3}\right). \quad (4.35)$$

Taking the exponential of equation (4.30) then gives us the solution to equation (4.20), which is given by

$$\mathbf{V}^m(t) \approx A \left(\frac{3}{25}\right)^m \exp\left(-\frac{\lambda^2 k_1 + 1}{\tau_M} t\right) \quad (4.36)$$

and so, if we scale our input according to $\left(\frac{25}{3}\right)^m$, we should expect to see that the output values become independent of the order of the graph approximation of the Sierpinski Gasket. This is indeed what happens, and is shown in Figure 4.6.

4.3.2 Neumann Boundary Conditions

We once again consider the discrete cable equation (4.20) on the Sierpinski Gasket and we repeat the numerical calculations from Section 4.3.1, this time imposing Neumann conditions at the boundary points. This is the equivalent of a segment of neuronal cable with sealed ends so no current can escape through the boundary nodes, only

through the cell membrane due to its capacitance and conducting properties. Once again the initial condition takes the form of a localised stimulus, amplitude one, applied this time at the boundary point P_1 .

The solution of equation (4.20) is given by equation (4.26) so we expect that after a long enough time, the solution will be of the form of the eigenfunction of the Laplacian (with Neumann boundary conditions) with the smallest eigenvalue. In the Neumann case there is always a zero eigenvalue that corresponds to a constant eigenfunction. We therefore expect to see the voltage diffuse to some spatially independent average value and slowly fall as current escapes through the membrane. The numerical solution of equation (4.20) is shown in Figure 4.7 and we see that this is indeed the case.

As in the Dirichlet case, we compare the output values obtained by solving the cable equation on Γ_m , $m = 3, 4, 5, 6$ for a consistent initial condition as shown in Figure 4.8 and once again, we find it necessary to scale the input. Equation (4.27) tells us that after a sufficiently long time the solution of equation (4.20) will be given by

$$\mathbf{V}^m(t) = c_1(0) \exp\left(-\frac{t}{\tau_M}\right) \mathbf{F}_1^m, \quad (4.37)$$

where \mathbf{F}_1^m is the eigenfunction of $-\Delta_m$ (subject to Neumann conditions at the boundary) corresponding to the zero eigenvalue. In its normalised form the value of \mathbf{F}_1^m at every vertex $x \in V_m$ is

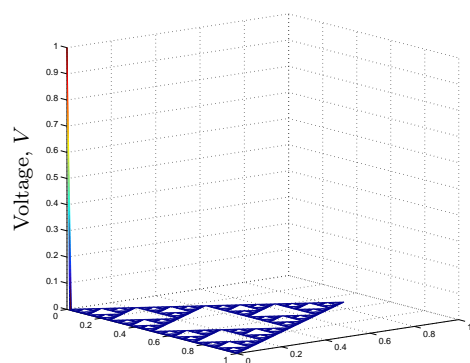
$$\mathbf{F}_1^m(x) = \frac{1}{\sqrt{\#(V_m)}} = \frac{1}{\sqrt{\frac{3}{2}(3^m + 1)}}, \quad (4.38)$$

and, (4.23) tells us that

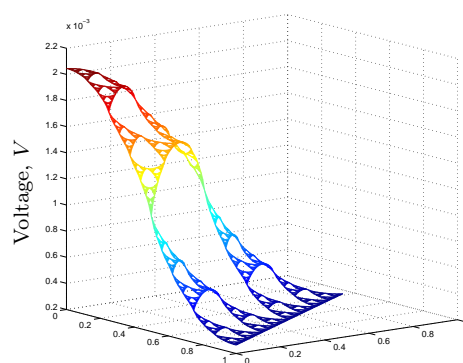
$$c_1(0) = \frac{1}{\sqrt{\frac{3}{2}(3^m + 1)}}. \quad (4.39)$$

We are interested in the voltage attained at the boundary point P_2 (which will be equal to that at P_3 due to symmetry) and after long enough time this is given by

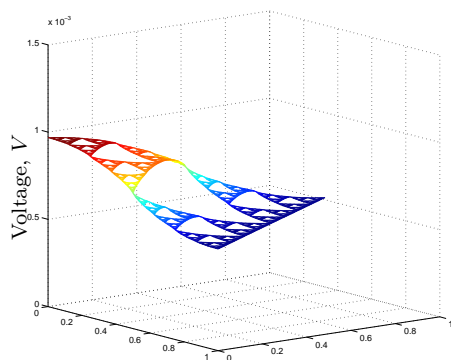
$$V_{P_2}^m = \frac{1}{\frac{3}{2}(3^m + 1)} \exp\left(-\frac{t}{\tau_M}\right). \quad (4.40)$$



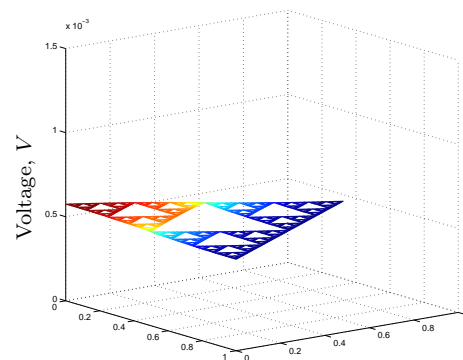
(a) $t = 0$



(b) $t = 0.1$



(c) $t = 0.25$



(d) $t = 0.5$

Figure 4.7: The solution of the discrete cable equation (4.20) on Γ_6 with Neumann boundary conditions.

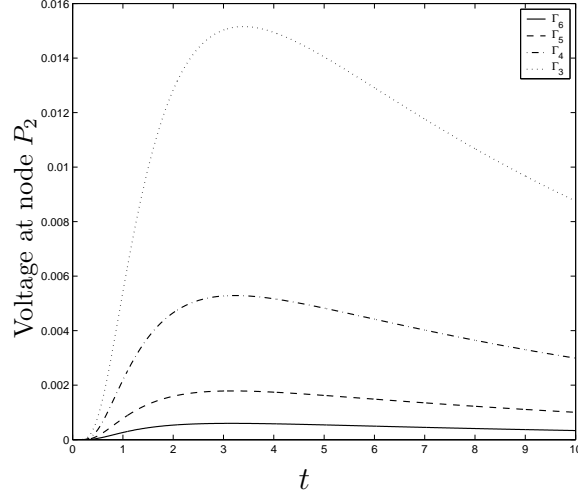


Figure 4.8: The voltage at the boundary point P_2 obtained by solving the cable equation with Neumann boundary conditions, subject to an initial stimulus, amplitude 1, at the boundary point P_1 .

Taking the natural logarithm of equation (4.40) we obtain

$$\ln \mathbf{V}_{P_2}^m = -\ln\left(\frac{3}{2}(3^m + 1)\right) - \frac{t}{\tau_M}, \quad (4.41)$$

which is in the form of a straight line $\ln \mathbf{V}_{P_2}^m = C_m - at$. We have

$$C_m = \ln\left(\frac{2}{3}\right) - \ln(3^m + 1) \approx \ln\left(\frac{2}{3}\right) - \ln(3^m), \quad (4.42)$$

provided $3^m \gg 1$. The difference between C_{m-1} and C_m is approximately $\ln(3)$ and the expression for C_m is then given by

$$C_m \approx C_{m-1} - \ln(3) = C_0 - \ln(3^m), \quad (4.43)$$

and so

$$\mathbf{V}^m(t) \approx A \left(\frac{1}{3}\right)^m \exp\left(-\frac{t}{\tau_M}\right). \quad (4.44)$$

In this case, we see that scaling the input by a factor of 3^m should give a constant output that is independent of the level of approximation to SG. The results of this are shown in Figure 4.9 and we see that, as m increases, the output voltage is indeed becoming independent of m . We notice that in this case, the convergence is slower due to the condition that we must have $3^m \gg 1$.

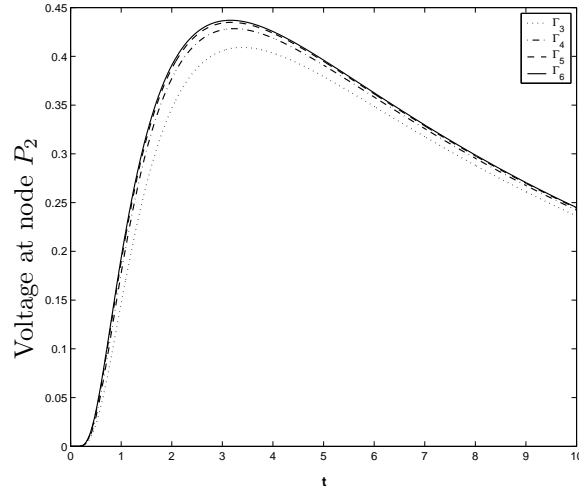


Figure 4.9: The voltage at the boundary point P_2 obtained by solving the cable equation with Neumann boundary conditions, subject to an initial stimulus, amplitude 3^k , at the boundary point P_1 .

4.3.3 Conclusion

We have found that, as the order of the graphical approximation to the Sierpinski Gasket increases, we must provide an increasingly large voltage spike in order to observe the same asymptotic behaviour. Moreover, the way that this voltage input scales depends on the boundary conditions. Effectively, we have been looking at the projection of the initial spike (always of magnitude 1 applied at the vertices which are the neighbours of P_1) onto the eigenfunction corresponding to the smallest magnitude eigenvalue of the Laplacian given Dirichlet or Neumann boundary conditions.

In the case of Dirichlet boundary conditions, current can leak from the system both at the boundaries and through the membrane. While for Neumann boundary conditions we see the effects of the membrane alone. In this latter case, if we were to let $\tau_M \rightarrow \infty$ we would see the initial pulse decay to a constant voltage which is uniform across the whole gasket. This constant is related to the average value, over all the nodes, of the initial input voltage. The scaling is then simply a matter of allowing for the increasing size of the approximating graph.

In this chapter we have established that we are seeing sense, that our linear PDE on the Sierpinski Gasket behaves in a reasonable way. In fact, we know that it is possible to observe some unusual behaviour also. For example, if our original disturbance took the form of one of the localised eigenfunctions of the Laplacian, discussed in Chapter 3, we expect that the resulting voltage distribution would remain localised while it decays. If we construct an orthogonal set of eigenfunctions for Neumann boundary conditions, then, because the constant function is always an eigenfunction, any localised eigenfunction must also have zero mean value. Thus the decay of a localised eigenfunction can be thought of as a mutual cancellation of its negative and positive voltage variations. Such behaviour takes place with no information reaching as far as the boundary of the Sierpinski Gasket. This is the dissipative analogue of the “hearing the shape of a drum” paradox. In particular, we note that such behaviour makes boundary value inverse problems likely to be ill-posed.

Chapter 5

FitzHugh-Nagumo Type Models

5.1 Introduction

In the previous chapter, we modelled the conduction of electrical impulses in neural tissue using the linear cable equation. The drawback of modelling such propagation using the cable equation is that it omits the essential feature that neurons are excitable. In this chapter we consider simple models of excitable neural systems. On a Euclidean domain, it is known that such systems can support various forms of wave solutions. We are interested in the solutions that exist when the system is solved on the Sierpinski Gasket; we wish to know if the geometrical complexity of the domain manifests itself in the phenomena that arise.

5.2 Excitable Media

An excitable medium can be considered as a continuum of coupled excitable elements whose dynamics behave nonlinearly and which interact with each other by a diffusion process. Excitable media have the ability to support undamped propagating waves of excitation: as each element is perturbed over some threshold value, it in turn excites its neighbours at a rate determined by the diffusion coefficient (a *passive* property of

the medium), and how quickly the diffused species of the excited element rises (an *active* property of the medium). Excitable systems occur in many different contexts, but they are all characterised by the following properties: each excitable element has a rest state which is stable for small perturbations. An impulse that exceeds a certain threshold value can, however, trigger a significant excursion before eventually returning to the rest state. After such a response, the medium becomes refractory; that is: it cannot undergo another excursion until it recovers full excitability.

We now give some examples of excitable systems, the wave solutions of which often give rise to complex spatial patterns. Travelling waves are commonly observed in chemical systems, the most well-studied being the Belousov-Zhabotinsky (BZ) reaction [18], where two-dimensional patterns have been observed [74, 75]. In a physiological context, the best known example is that of the propagation of an action potential along the axon of a nerve cell. Similar phenomena are also observed in cardiac tissue.

A general form of excitable media model is represented by the interaction of two variables: a fast excitation variable u and a slow recovery variable v . These variables interact locally according to the differential equations $\frac{du}{dt} = f(u, v)$, $\frac{dv}{dt} = g(u, v)$. The model is therefore given by the following pair of reaction diffusion equations:

$$\begin{aligned}\varepsilon \frac{\partial u}{\partial t} &= \varepsilon^2 \Delta u + f(u, v) \\ \frac{\partial v}{\partial t} &= \varepsilon \delta \Delta v + g(u, v),\end{aligned}\tag{5.1}$$

where ε is a small positive parameter, which represents the time scale distinction between the dynamics of the fast and slow variables u and v . The parameter δ is the ratio of the diffusion coefficients of the two variables.

Much work has been carried out on the study of wave propagation in excitable media based on equations of the form of (5.1) in one, two and three spatial dimensions. Singular perturbation methods have been used to analyse such wave solutions in two main cases: firstly, when $\delta = 0$, the recovery variable does not diffuse in space, which is characteristic of pulse propagation in neural fibres and secondly, when $\delta \approx 1$, which

is characteristic of activity waves in the BZ reaction (see [39] and [71] and references therein for a summary of important work on singular perturbation theory in these cases).

The existence of spiral waves in the two dimensional case has proved to be of great interest due to its relevance to fibrillation in cardiac tissue [40, 10, 35, 16]. More recently, the three dimensional counterpart of the spiral wave, the scroll wave, has been studied and the singular perturbation methods used to understand spiral waves have been extended to the three dimensional case, [54], [55].

5.3 Hodgkin-Huxley Theory

In one spatial dimension, the best known example of an excitable medium is that of the nerve cell or neuron. Our understanding of this theory today is due chiefly to the experiments on the giant squid axon by the physiologists Hodgkin and Huxley, the results of which were presented in a series of papers [33, 30, 29, 31, 32].

The cell membrane of a nerve cell consists of two layers of fat molecules, which are separated by an insulating gap. When a neuron is at rest, the concentrations of various ions differs between the interior and the exterior of the cell. These differing ionic concentrations give rise to a net voltage across the membrane, commonly referred to as the membrane potential. The membrane potential for most neurons at rest typically lies between -50mV and -90mV, so the interior of the cell is negatively charged with respect to the exterior. This separation of charge creates a capacitance effect and so the basic model for a cell membrane is based on that of a capacitor:

$$C \frac{dV}{dt} = \frac{dQ}{dt}, \quad (5.2)$$

where C is the capacitance of the membrane, V is the potential across the membrane and Q is the charge. A key assumption of Hodgkin and Huxley was that the membrane, under certain conditions, can become permeable to sodium and potassium ions. Therefore, the total current flowing across the membrane is made up from

contributions from the capacitance and ionic currents. This can be written as:

$$I(t) = C \frac{dV}{dt} + I_i, \quad (5.3)$$

where I_i is split into contributions from the flow of sodium and potassium ions and a leakage current:

$$I_i = I_{Na} + I_K + I_L. \quad (5.4)$$

Each contribution can be written as

$$I_\gamma = g_\gamma(V - V_\gamma), \quad \gamma \in \{Na, K, L\}, \quad (5.5)$$

where g_γ ($g_\gamma(0) = 0$) is a function giving the voltage dependence of the conductance of the membrane to the ion in question and V_γ is the potential at which there is no net flux of the ion across the membrane. Equation (5.3) then becomes

$$I(t) = C \frac{dV}{dt} + g_{Na}(V - V_{Na}) + g_K(V - V_K) + g_L(V - V_L). \quad (5.6)$$

Hodgkin and Huxley hypothesised that the ionic conductances, g , can be written in terms of the maximum conductances \bar{g} and the *gating* variables for the opening and closing of the ion channels. We therefore have

$$\begin{aligned} g_{Na} &= \bar{g}_{Na} m^3 h, \\ g_K &= \bar{g}_K n^4. \end{aligned} \quad (5.7)$$

The dynamics of the gate variables m, n, h are assumed to follow kinetics governed by equations of the form

$$\frac{dw}{dt} = \alpha_w(V)(1 - w) - \beta_w(V)w, \quad w \in \{m, n, h\}, \quad (5.8)$$

where α and β are functions of the voltage V chosen by Hodgkin and Huxley to fit the experimental data. Taken together, equations (5.3) and (5.8) represent the four dimensional Hodgkin-Huxley model for nerve impulse propagation.

5.3.1 The FitzHugh-Nagumo Model

In the mid 1950s, FitzHugh sought to reduce the Hodgkin-Huxley model to a two variable model for which phase plane analysis applies. His general observation was that the gating variables n and h have slow kinetics relative to m and that for Hodgkin and Huxley's parameter values, $n + h$ is approximately constant. This led to a two variable model in V and n . A further observation due to FitzHugh was that the V -nullcline had the shape of a cubic function and the n -nullcline could be approximated by a straight line. The model, originally proposed by FitzHugh in 1961 [19] and subsequently developed by Nagumo and his coworkers in 1962 [56] is known as the FitzHugh-Nagumo (FHN) system. In dimensionless form the FHN system is written as follows:

$$\begin{aligned}\frac{du}{dt} &= u(1-u)(u-\alpha) - v + I \\ \frac{dv}{dt} &= \varepsilon(u - \gamma v),\end{aligned}\tag{5.9}$$

where u represents the fast variable (membrane potential), v represents the slow variable (sodium gating), α , γ and ε are constants with $0 < \alpha < 1$ and $\varepsilon \ll 1$ (accounting for the slow kinetics of the sodium channel) and I is an applied electrical stimulus. Many different forms of the FHN system exist, [63] gives many of the popular versions along with a conversion between them.

A typical phase portrait for the system (5.9), when $I = 0$, is shown in Figure 5.1. From Figure 5.1 we see how the FHN system exhibits excitable behaviour. If the initial condition is less than the threshold value α , then the potential returns quickly to the unique fixed point at the origin. If, however, the initial condition is perturbed above the threshold, then the potential undergoes a large excursion before returning to the rest state.

We have discussed how an excitable medium comprises a continuum of coupled excitable cells. We therefore need to add some spatial dependence into our problem. The FHN model can then be written as a system of two coupled partial differential

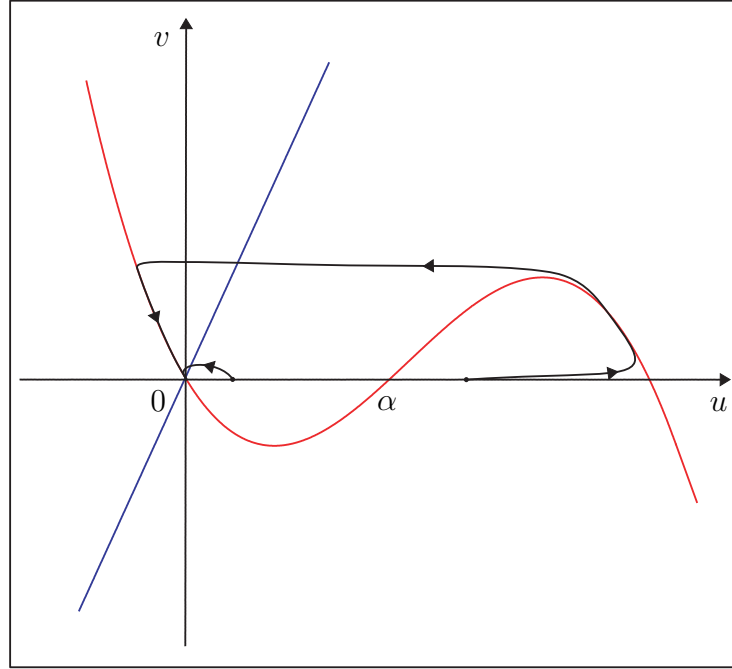


Figure 5.1: A typical phase portrait for the system (5.9).

equations:

$$\begin{aligned} \frac{\partial u}{\partial t} &= d\Delta u + u(1-u)(u-\alpha) - v + I \\ \frac{\partial v}{\partial t} &= \varepsilon(u - \gamma v), \end{aligned} \tag{5.10}$$

where the term $d\Delta u$ represents the propagation of the potential u at a rate determined by the diffusion coefficient d . We note that diffusion is not added to the equation governing v , since this represents the voltage-dependent opening and closing of the sodium channels and is not assumed to have spatial dependence. A comparison between this model and the cable equation studied in Chapter 4 (see equation (4.12)) shows that the term $v - u(1-u)(u-\alpha)$ replaces the linear term in the cable equation which represents the membrane leakage current (and of course the FitzHugh-Nagumo equation models the dynamics of the sodium gating).

The system (5.10) looks like system (5.1) under a rescaling of the spatial coordinate and with $\delta = 0$. In one spatial dimension, equations of this form are used to model

nerve impulse propagation and in two spatial dimensions, equations of this form can model excitation in cardiac tissue.

5.4 The Heart as an Excitable Medium

The heart is essentially an electromechanical pump consisting of four chambers: the two upper atria and the two lower ventricles. The function of the right side of the heart is to collect deoxygenated blood from the body and circulate it to the lungs. Once reoxygenated, the blood flows to the left side of the heart, from where it is pumped to the rest of the body. The cardiac cycle consists of two main actions: systole and diastole. The term systole is synonymous with contraction of a muscle and comprises two phases: atrial systole, where both atria contract at the same time forcing blood into the ventricles (known as atrial kick); and ventricular systole, where the subsequent contraction of the ventricular muscle pumps blood out into the body. This contracting phase is followed by complete cardiac diastole, where the heart relaxes in preparation for refilling.

The mechanical action of a heart beat is governed by underlying electrical activity. Each of the chambers of the heart is composed predominately of muscular tissue called myocardium. The myocardium is special because, unlike other muscles, it can conduct electricity, like nerve cells. Cardiac muscle is myogenic, meaning that it stimulates its own contraction without requiring an electrical impulse. A single cardiac cell, if left without input will rhythmically contract at a steady rate. If a number of cardiac cells interact, the contraction of the first will stimulate the second and so on. In this way, rhythmic sequences of electrical pulses propagate through the myocardium, triggered by stimuli that spread from the sinoatrial node, sometimes referred to as the heart's natural pacemaker. As is the case with nerve cells, this wave of excitation is called an action potential.

Action potentials differ in different portions of the heart, both qualitatively and

in duration. The governing processes are, however, the same and are outlined here. At rest, the myocardial cell has a resting membrane potential of around -90mV , due to differing ion concentrations on either side of the cell membrane. The arrival of a stimulus increases the membrane potential and causes voltage-gated sodium channels to open. Positively charged Na^+ ions then enter the cell, increasing the membrane potential further, thus causing more sodium channels to open. This is an auto-catalytic process and causes a sudden, fast influx of sodium ions, which is known as fast depolarisation. Soon after they open, the sodium channels close. The potential now saturates as the outward movement of potassium ions (K^+) is balanced by the inward movement of calcium ions (Ca^{2+}) through their respective ion channels. The potassium channels remain open well after the calcium channels have closed, the continuing efflux of K^+ ions repolarises the cell and the potential returns to its resting value.

The Modified FHN System

The system we consider here is a modified form of the FitzHugh-Nagumo Equations proposed in [21]:

$$\begin{aligned} u_t &= \nabla^2 u + \varepsilon^{-1} u (1 - u) \left(u - \frac{v + \gamma}{\alpha} \right) \\ v_t &= u^3 - v. \end{aligned} \tag{5.11}$$

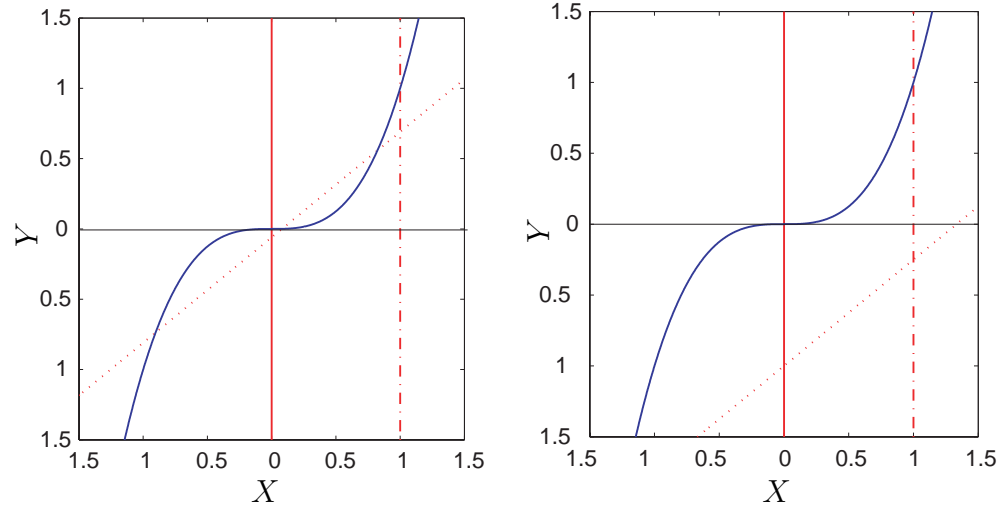
Initially, let us consider the spatially independent case:

$$\begin{aligned} \frac{dX}{dt} &= \varepsilon^{-1} X (1 - X) \left(X - \frac{Y + \gamma}{\alpha} \right) \\ \frac{dY}{dt} &= X^3 - Y. \end{aligned} \tag{5.12}$$

System (5.12) has fixed points satisfying

$$Y = X^3, \quad X(1 - X) \left(X - \frac{X^3 - \gamma}{\alpha} \right) = 0, \tag{5.13}$$

and we note that these fixed points correspond to spatially uniform fixed points of the PDE system (5.11). Clearly, there will be two fixed points at $(0, 0)$ and $(1, 1)$ and



(a) Here $\alpha = 0.75$ and $\gamma = 0.06$, so in this case the system (5.11) has five fixed points.

(b) In this case α remains the same, while $\gamma = 1$, and we see now the number of steady states is reduced to three.

Figure 5.2: The nullclines of the modified FHN system. The red curves show $\frac{dX}{dt} = 0$ and the blue curves show $\frac{dY}{dt} = 0$.

either one or three more, corresponding to the roots of the cubic $X^3 - \alpha X + \gamma = 0$. Whether this cubic will have one root or three roots depends on the values of the parameters α and γ . The transition from one case to the other occurs when the second turning point (minimum) of the curve touches the X -axis, i.e. when

$$3X^2 - \alpha = 0 \quad \Leftrightarrow \quad X_{min} = \sqrt{\frac{\alpha}{3}}$$

We have two cases:

$$\begin{aligned} X_{min}^3 - \alpha X_{min} + \gamma > 0 &\Rightarrow \text{one root,} \\ X_{min}^3 - \alpha X_{min} + \gamma < 0 &\Rightarrow \text{three roots,} \end{aligned} \tag{5.14}$$

giving us either three or five fixed points. The nullclines for both of these cases are shown in Figure 5.2.

5.5 Wave Solutions of a Modified FitzHugh-Nagumo System-Euclidean Domain

We have discussed how a super-threshold stimulus on an excitable medium can elicit a wave of excitation travelling from the initiation site. The remainder of this chapter will be concerned with various types of travelling wave solutions of the system (5.11) that exist and the initial conditions that give rise to them. We restrict ourselves to the second case in (5.14), where α and γ satisfy:

$$\gamma < \frac{2}{\sqrt{3}} \alpha^{\frac{3}{2}}. \quad (5.15)$$

We shall therefore fix $\alpha = 0.75$, $\gamma = 0.06$ and let ε vary as a bifurcation parameter.

For the numerical calculations reported in the chapter, the system is solved using an analogue of the method of lines: we semi-discretise the problem replacing the Laplacian by the standard five point difference formula in the case of a Euclidean domain and our standard discrete Laplacian in the SG case. The resulting ODE system is then solved, subject to Neumann boundary conditions and a suitable initial condition, using the Matlab solver `ode23`.

We consider here the effects of applying super-threshold stimuli to a homogeneous excitable medium. The refractoriness of the medium affects pulse propagation in that pulses generally travel forwards towards previously unexcited tissue. The numerical simulations here are carried out on the square domain $\Omega = [0, 50] \times [0, 50]$ with Neumann boundary conditions. This box size has been chosen to be large compared with the length scale over which u diffuses in the scaled unit time.

5.5.1 Planar Wave Fronts in Two Dimensions

The first case we shall consider is that of a planar wave. To initiate a planar wave, we excite the whole of the left hand side of the domain. The Neumann conditions at the boundary cause the wave to propagate to the right and it is well known that this

wave will propagate across the domain at a constant velocity. Figure 5.3 shows the propagation of such a wave. In this case we took $\varepsilon^{-1} = 14$.

It is possible to calculate the wave speed of the planar wave shown in Figure 5.3 numerically. We consider the values of the potential u along the lower edge of our domain. Figure 5.4 shows the propagation of the wavefront as a function of the spatial coordinate at discrete time intervals. At different instances in time, the position of the wavefront can be identified by locating the greatest negative difference in the values of u . Figure 5.5 shows the location of the wavefront as a function of time. This appears to be a straight line indicating that the planar wave does propagate with constant velocity. The wave velocity is denoted by \tilde{c} and is given by the gradient of the curve in Figure 5.5. We find that the plane wave propagates across our domain at a velocity

$$\tilde{c} \approx 2.17 \tag{5.16}$$

Later on in this chapter, we shall be comparing the velocities of wave propagating across Euclidean domains and the Sierpinski Gasket. It therefore makes sense to normalise the wave speed by dividing by the linear size of our domain. This gives us

$$\tilde{c}_N \approx 0.043. \tag{5.17}$$

The velocity of waves propagating in an excitable medium can be found approximately using asymptotic analysis. This is a well-studied problem, see [71], and usually considers a pair of reaction-diffusion equations of the form:

$$\begin{aligned} \varepsilon u_t &= \varepsilon^2 \nabla^2 u + f(u, v) \\ v_t &= \varepsilon \delta \nabla^2 v + g(u, v), \end{aligned} \tag{5.18}$$

where u and v take values in $[0, 1]$. Equations (5.11) can be reduced to the same form as equations (5.18) by setting $\delta = 0$ and choosing a suitable rescaling. We therefore rescale space according to $X = \sqrt{\varepsilon}x$ and seek travelling wave solutions of the form $u(X, t) = u(z)$, $v(X, t) = v(z)$, $z = X - ct$. This represents a pulse with fixed wave

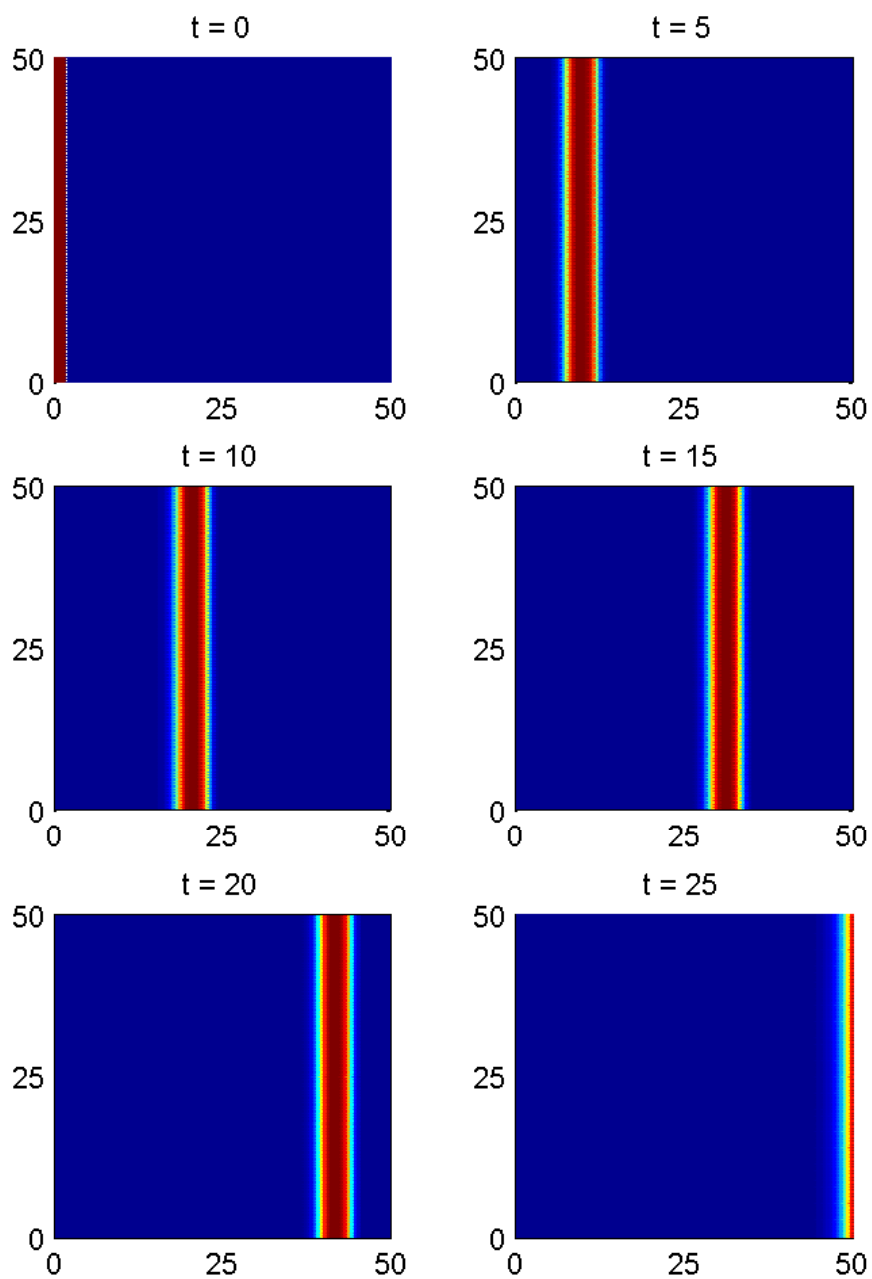


Figure 5.3: The potential, u , plotted for a planar wave initiated by putting u above the threshold at the left edge of the domain. A movie of this figure can be found on the accompanying CD, named FHNMov1.avi.

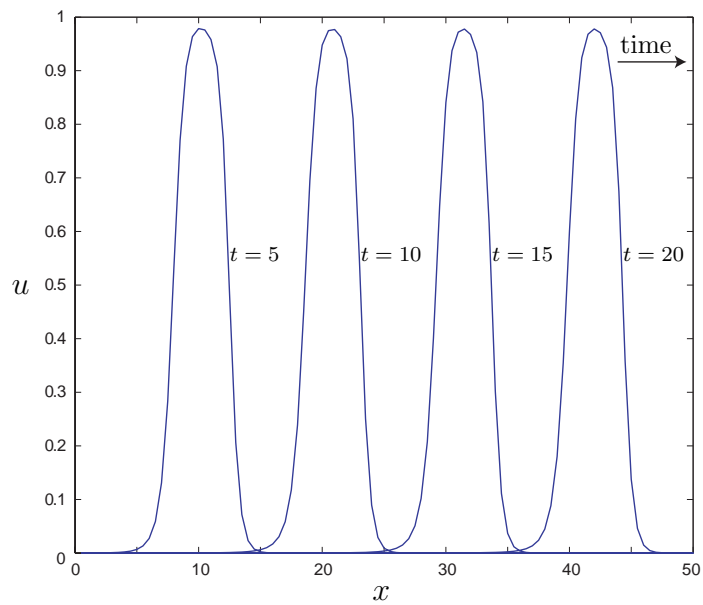


Figure 5.4: The position of a planar wave for discrete times.

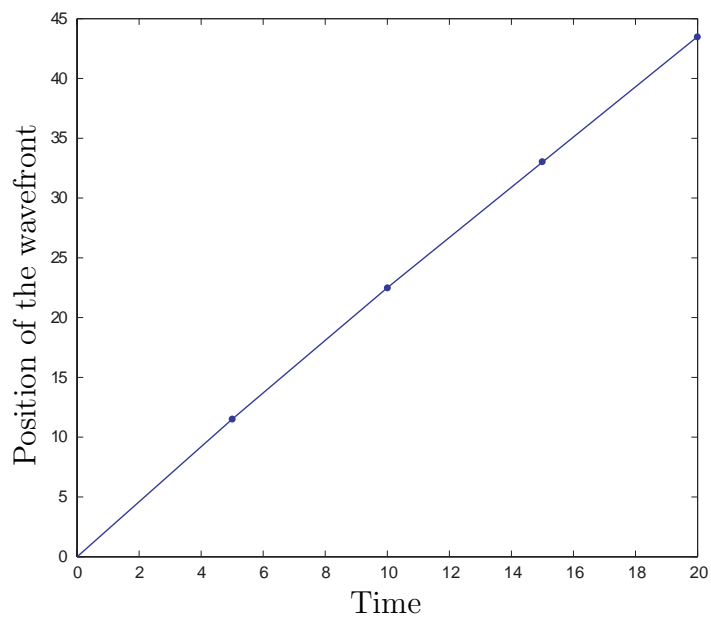


Figure 5.5: The position of the wavefront as a function of time.

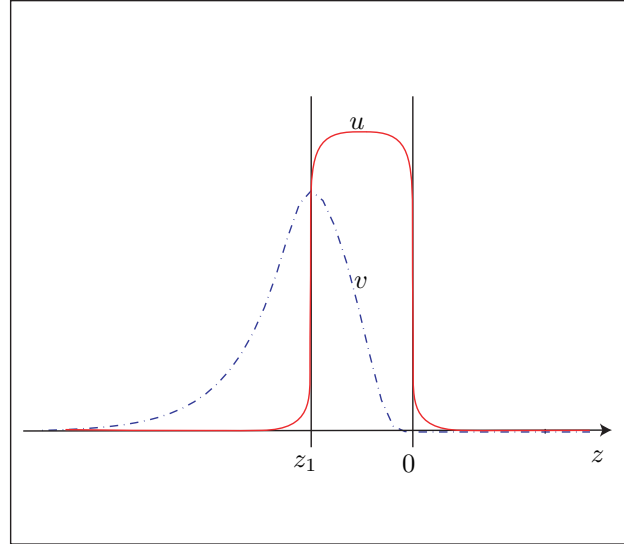


Figure 5.6: Schematic diagram showing the form of u and v in the travelling frame.

form travelling to the right with speed c . Ahead of the pulse, the variable u remains at rest. At the wave front, $z = 0$, the value of u increases rapidly to the excited state and returns to rest at $z = z_1 < 0$. Figure 5.6 shows the form of the wave solutions we are seeking in the travelling frame.

In the travelling coordinate system, equations (5.11) become

$$\begin{aligned} \varepsilon^2 u_{zz} + \varepsilon c u_z + u(1-u) \left(u - \frac{v+\gamma}{\alpha} \right) &= 0 \\ c v_z + u^3 - v &= 0. \end{aligned} \tag{5.19}$$

Since ε is small, the first equation in (5.19) will remain in equilibrium provided $f(u, v) = u(1-u) \left(u - \frac{v+\gamma}{\alpha} \right) \approx 0$ and so we expect that the solution trajectories will stay close to this curve, apart from points where they may jump from branch to branch. In this case the first and second derivatives of u with respect to z will be large. The condition $f(u, v) = 0$ has, for our parameter values, four branches:

1. $u = 0 \Rightarrow \partial_t v = -v$.

This equation has a globally attracting fixed point at $v = 0$.

2. $u = 1 \Rightarrow \partial_t v = 1 - v.$

This equation has a globally attracting fixed point at $v = 1.$

3. $u = \frac{v+\gamma}{\alpha} \Rightarrow \partial_t v = \frac{1}{\alpha^3}(v + \gamma)^3 - v.$

For our chosen values of α and γ , this has two solutions in the region of interest. The first solution (smaller value of v) being stable, and the second being unstable.

For our purposes there are two relevant branches: $u = 0$, which we shall call u_- ; and $u = 1$, or $u_+.$

We consider the problem in three regions: ahead of the wave front, $z > 0$; during the pulse, $z_1 < z < 0$; and behind the wave back, $z < z_1.$ The two outer solutions must then be matched to the inner solution.

Ahead of the Wave Front

For $z > 0$ the medium is at rest and excitable so we have:

$$\begin{aligned} u &= 0, \\ cv_z &= v, \\ \lim_{z \rightarrow \infty} v &= 0, \\ v(0) &= v_0. \end{aligned} \tag{5.20}$$

We note that $v = 0$ is an unstable solution of the second of equations (5.20) and so, in order to satisfy the condition that $v \rightarrow 0$ as $z \rightarrow \infty$, we must have $v(0) = v_0 = 0.$

Behind the Wave Back

After the pulse has propagated through the medium it returns to the rest state and so for $z < z_1$, we have

$$\begin{aligned}
 u &= 0, \\
 cv_z &= v, \\
 \lim_{z \rightarrow -\infty} v &= 0, \\
 v(z_1) &= v_1.
 \end{aligned} \tag{5.21}$$

During the Pulse

During the pulse, the medium is in the excited state giving the following:

$$\begin{aligned}
 u &= 1, \\
 cv_z &= v - 1, \\
 v(z_1) &= v_1, \\
 v(0) &= v_0 = 0.
 \end{aligned} \tag{5.22}$$

Matching Inner and Outer Solutions

At $z = z_1$ and $z = 0$, the solution is discontinuous and so we introduce a boundary layer where we can match the solutions in the inner and outer regions. To do this, we introduce a stretched coordinate $\xi = \frac{z}{\varepsilon}$, then equations (5.19) become

$$\begin{aligned}
 u''(\xi) + cu'(\xi) + u(1-u)\left(u - \frac{v+\gamma}{\alpha}\right) &= 0 \\
 cv'(\xi) + \varepsilon(u^3 - v) &= 0.
 \end{aligned} \tag{5.23}$$

For matching at $z = 0$, we require:

$$\begin{aligned}
 \lim_{\xi \rightarrow \infty} u(\xi) &= u_- = 0, \\
 \lim_{\xi \rightarrow -\infty} u(\xi) &= u_+ = 1.
 \end{aligned} \tag{5.24}$$

Conditions (5.24) are simply reversed to match the solutions at $z = z_1$. Setting $v(0) = 0$ and neglecting terms of order ε gives us a single second order ODE in u :

$$u'' + cu' + u(1 - u)(u - \frac{\gamma}{\alpha}) = 0. \quad (5.25)$$

Setting $u' = w$ yields the first order system:

$$\begin{pmatrix} u' \\ w' \end{pmatrix} = \begin{pmatrix} w \\ -u(1 - u)(u - \frac{\gamma}{\alpha}) - cw \end{pmatrix}, \quad (5.26)$$

subject to boundary conditions $u(-\infty) = 1$, $u(\infty) = 0$.

System (5.26) has three steady states, namely $(u_*, w_*) = (u_i, 0)$, $u_i \in \{0, \frac{\gamma}{\alpha}, 1\}$.

To analyse the system, we linearise it about these three steady states:

$$\begin{pmatrix} u' \\ w' \end{pmatrix} \approx \begin{pmatrix} 0 & 1 \\ 3u^2 - 2u(1 + \frac{\gamma}{\alpha}) + \frac{\gamma}{\alpha} & -c \end{pmatrix} \Big|_{(u_*, w_*)} \begin{pmatrix} u \\ w \end{pmatrix} \quad (5.27)$$

and we find that they are (for $c > 0$) a saddle, a stable focus or node (depending on the values of c , α and γ) and a saddle respectively. If

$$c^2 > 4 \left(\frac{\gamma}{\alpha} - \left(\frac{\gamma}{\alpha} \right)^2 \right)$$

then the fixed point will be a stable node, otherwise, it will be a stable focus.

When $c = 0$ the system is Hamiltonian and the potential is given by:

$$V(u) = \int f(u, 0) du = u^2 \left(-\frac{1}{4}u^2 + \frac{1 + \frac{\gamma}{\alpha}}{3}u - \frac{\gamma}{2\alpha} \right).$$

In this case there exists a homoclinic orbit of the saddle at the origin which encircles the fixed point at $(\frac{\gamma}{\alpha}, 0)$, which is a centre. A small, positive perturbation of c leads to this orbit being broken and the saddle at the origin will connect to the stable focus at $(\frac{\gamma}{\alpha}, 0)$. If the value of c is increased further, both saddles will connect to the fixed point at $(\frac{\gamma}{\alpha}, 0)$, see Figure 5.7. There exists a unique value of c , c_* which separates the two cases mentioned above. For this value of c there is a heteroclinic orbit connecting the saddles at the origin and at $(1, 0)$. This heteroclinic orbit describes the change

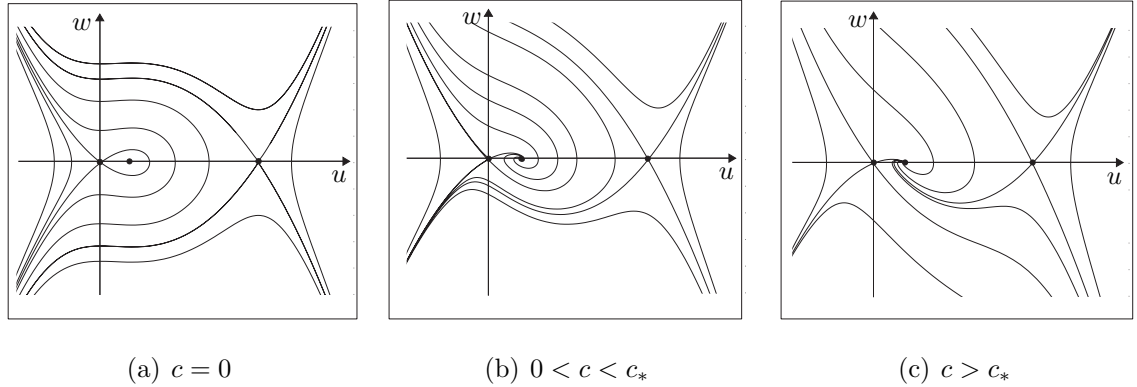


Figure 5.7: Phase portraits of the system (5.26) for different values of c .

of the potential from the rest state to the excited regime and back again. That is, it provides the matching between solutions in the inner and outer regions.

An approximate value for c_* can be found using a shooting method. System (5.26) is solved numerically with initial condition equal to $(1, 0)$ perturbed with a small amount of the eigenvector corresponding to the unstable eigenvalue of the matrix in equation (5.27) evaluated at $(u_*, w_*) = (1, 0)$. Using this method, the value of c_* is found to be $c_* \approx 0.5657$. In terms of our original spatial variable x , the wave speed is given by:

$$\tilde{c} = \frac{c}{\sqrt{\varepsilon}}. \quad (5.28)$$

Let us compare this to the wave speed we calculated numerically earlier in this section given in equation (5.16). With $\varepsilon^{-1} = 14$, equation (5.28) gives us

$$\tilde{c} = \sqrt{14} c_* \approx 2.1166. \quad (5.29)$$

The asymptotic analysis therefore gives us a reasonable approximation to our computed wave speed.

5.5.2 Curved Wave Fronts in Two Dimensions

Let us now consider the effect of applying a localised stimulus to the domain. This is the equivalent of exciting a single cell or group of neighbouring cells. In this case a

wave of excitation moves out as an expanding circle, called a target pattern. Figure 5.8 shows the evolution of a target wave generated by solving system (5.11) when the initial condition is a stimulus, amplitude 1, applied at the centre of the domain. The target pattern is destroyed as it collides with the boundary of the domain. Target waves are produced by the simplest of excitations. When analysing the propagation of such waves, however, the effect of curvature must be taken into consideration.

The analysis of the wave speed of curved wave fronts was first carried out by Zykov, [78, 77] in the case when $\delta = 0$, and by Keener [41, 42] when $\delta \geq 0$. The wave speed of a curved wave front is given by the relation (up to order ε):

$$N = c + \varepsilon K \tag{5.30}$$

Here, N is the normal velocity and c is the wave speed of a planar wave propagating across the domain. The curvature of the propagating wavefront is given by K . If the wave front is curved away from its direction of propagation, then $K < 0$. If the curvature is in the direction of propagation, then $K > 0$. The correction term εK is only meaningful if $K \gg 1$, however if $K = O(1)$ then the wave can be treated as planar. Equation (5.30) is given in dimensionless form. If the variables are considered in terms of physical units, equation (5.30) reads:

$$N = c + DK, \tag{5.31}$$

where D is the diffusion coefficient of the fast variable u (the product DK does indeed have dimensions of a velocity).

Clearly in the case of target patterns, the curvature only affects the wave speed close to the initiation site. As the wave expands away from the central region of excitation, the (negative) curvature becomes negligible and the wave speed increases to that of a planar wave. There are, however, certain types of curved wavefront for which the curvature plays an important role in determining the wave speed.

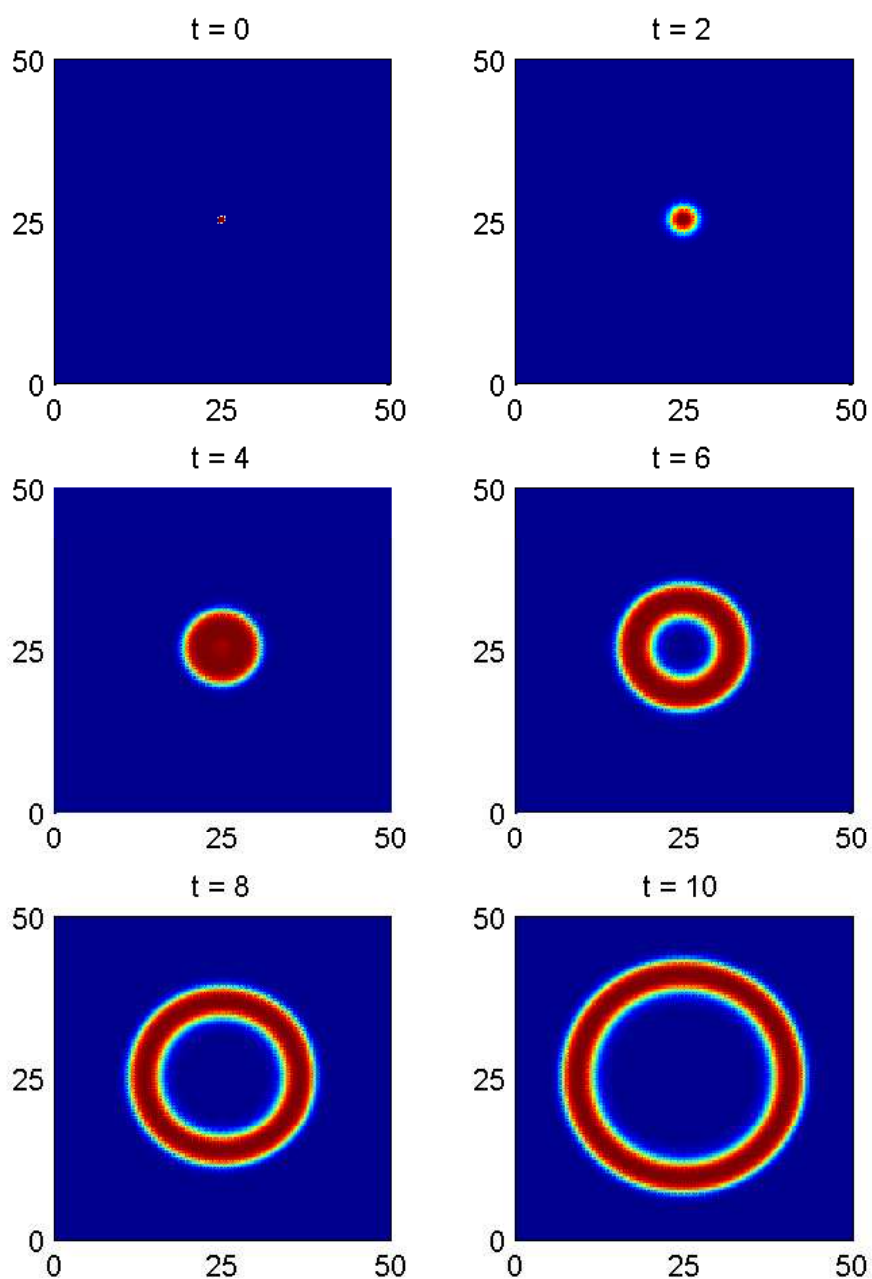


Figure 5.8: The propagation of a target wave resulting from a stimulus applied to the centre of the domain. A movie of this figure can be found on the accompanying CD, named FHNMov2.avi.

5.6 Wave Solutions of a Modified FitzHugh-Nagumo System-Sierpinski Gasket

We have seen how waves of excitation can propagate across a homogeneous excitable medium. In this section we are concerned with whether similar solutions exist if the medium in question is geometrically complex and we shall investigate the similarities and differences that exist between the Euclidean and fractal cases. Here we shall solve system (5.11) numerically using the same method and parameter choices as in Section 5.5.

Once again we must choose the domain to be sufficiently large so that the size of our wave (the distance between the wavefront and the waveback) is small compared to the size of the domain. We therefore choose to work on an approximation to SG whose sidelength is $32 = 2^6$ units. In addition, we choose our order of approximation to be $m = 6$. This level of approximation is high enough to reasonably represent the gasket, yet small enough to make numerical simulations relatively fast. We denote this domain by Γ_6^6 .

As opposed to the Euclidean case, a planar wave on the Sierpinski Gasket could propagate in two ways: from an edge towards the opposite corner, or from a corner to an edge. Figures 5.9 and 5.10 show the propagation of such a wave in both of the above cases. The wave in Figure 5.9 was initiated by setting $u = 1$ along the left hand edge of the gasket, whereas in Figure 5.10 the boundary point P_3 and its two nearest neighbours were excited.

A Numerical Estimate of the Wave Speed

In [1] and [2] a different discretisation of the Sierpinski Gasket is considered and a numerical estimate for the wave speed of planar wave solutions to an excitable reaction-diffusion system is obtained. The system studied is known as the Rinzel-Keller (RK) model [62], in which the cubic reaction term of the FHN system is replaced

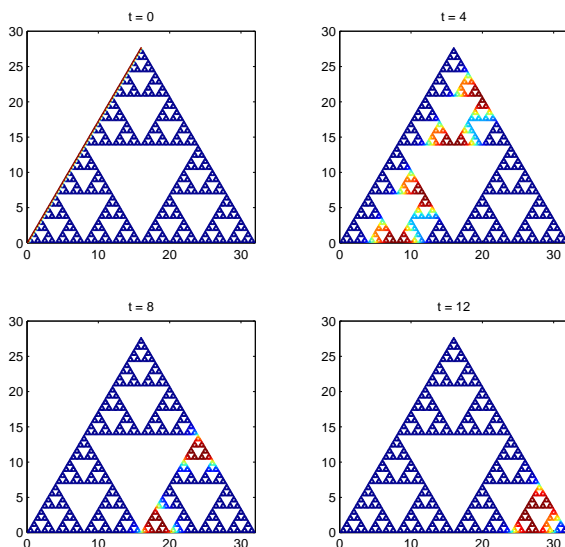


Figure 5.9: The potential, u , plotted for a planar wave, resulting from setting $u = 1$ along the edge between the boundary points P_1 and P_3 . A movie of this figure can be found on the accompanying CD, named FHNMov3.avi.

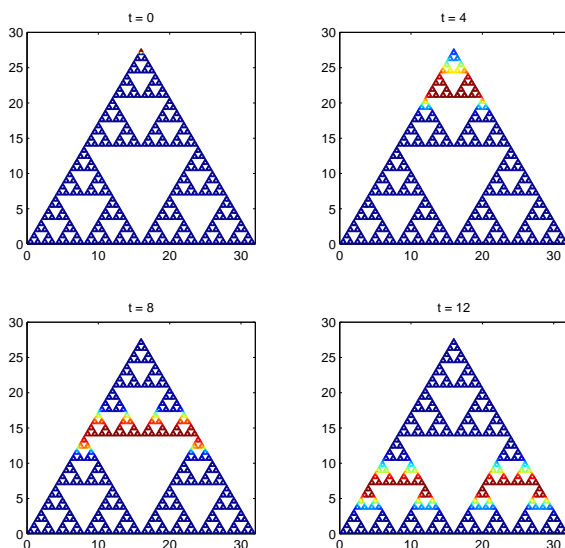


Figure 5.10: The propagation of a planar wave, resulting from setting $u = 1$ at the boundary point P_3 and its two neighbours. A movie of this figure can be found on the accompanying CD, named FHNMov4.avi.

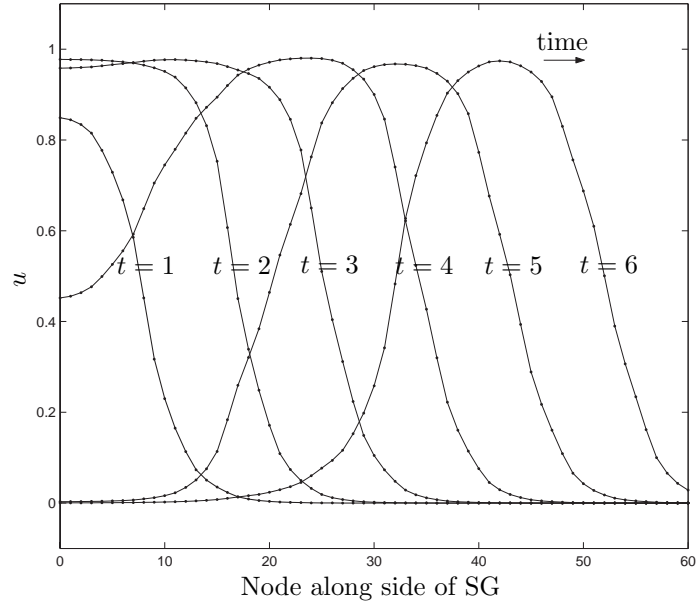
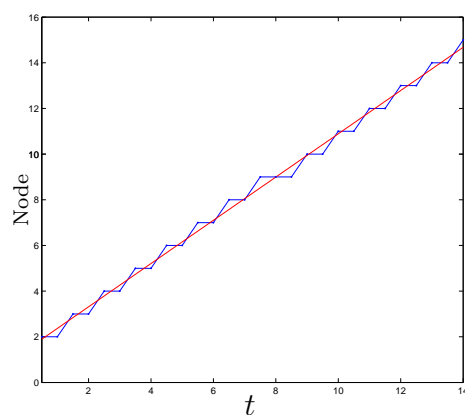


Figure 5.11: The wave profiles of a planar wave propagating across Γ_7^6 .

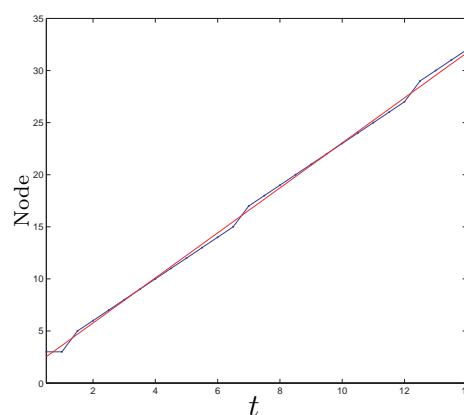
by a piecewise linear approximation. Here we use a similar method to calculate the wave speed of a planar wave solution of the modified FHN system (5.11) propagating across our graph approximations to the Sierpinski Gasket.

In order to obtain a numerical estimate for the wave speed of a planar wave propagating across the Sierpinski Gasket, we solve the system (5.11) on Γ_m for $m = 4, 5, 6, 7$ and 8. We initiated a planar wave by exciting a small number of nodes in one corner of V_m (for $m = 4, 5, 6$ the point P_3 and its two neighbours were excited, for $m = 7, 8$ it was necessary to excite P_3 and its five nearest neighbours for a planar wave to propagate), the wave then propagates to the opposite edge. As the wave propagates we look along one side of the gasket (where we number the nodes from 1 to $2^m + 1$) and consider the wave profiles at different instances of time. The wave profiles in the case where $m = 7$ are shown in Figure 5.11.

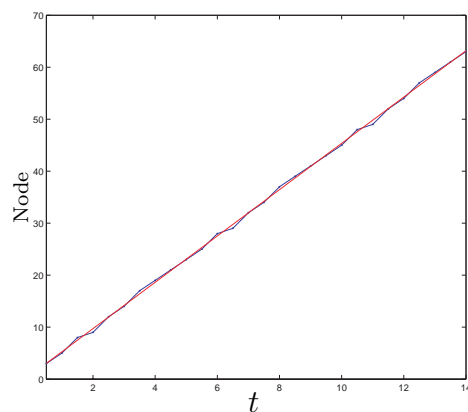
At a number of different instances of time, we identify the wavefront by locating the position along the side of Γ_m where the difference in the value of u at two adjacent nodes is greatest. Figure 5.12 shows the position of the wavefront as a function of time



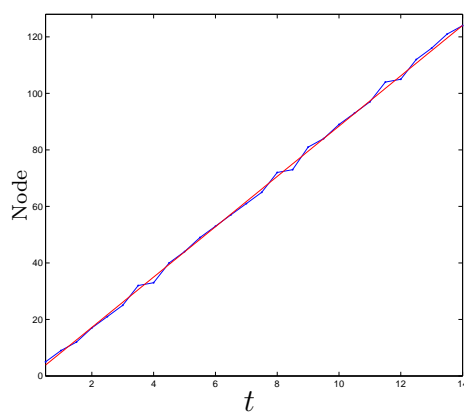
(a) Γ_4 : The gradient of the linear approximation is 0.9469



(b) Γ_5 : The gradient of the linear approximation is 2.1606



(c) Γ_6 : The gradient of the linear approximation is 4.4548



(d) Γ_7 : The gradient of the linear approximation is 8.9025

Figure 5.12: The nodal position of the wavefront (blue) and a linear least squares approximation (red) plotted as a function of time.

for $m = 4, 5, 6, 7$. We see that the position of the wavefront appears to change linearly with time and this suggests that the planar wave does indeed propagate across Γ_m at a constant speed. We note here that the curves plotted in Figure 5.12 do not appear as straight lines. This is probably due to the wave speed and the sampling times not being synchronised. The velocity of the wave is found from the gradient of the lines plotted in Figure 5.12. Since the wave speed depends on the order of approximation to the gasket, we divide by the number of nodes on one side of Γ_m . We carried out similar calculations for a plane wave travelling across the gasket from an edge towards the opposite corner. Figure 5.13 shows this normalised wave speed as a function of m in both these cases. We see that, as m increases, the speed of propagation tends to a constant value. For a wave travelling from a corner to an edge we have

$$c_N \approx 0.069, \tag{5.32}$$

and for a wave travelling from an edge to a corner, we have

$$c_N \approx 0.075. \tag{5.33}$$

In both the Euclidean and Sierpinski Gasket cases, the phenomena seen here are comparable. The two wave forms are structurally similar and behave in the same way, propagating at a constant velocity. We can normalise the wave speed in the Euclidean case by dividing by the number of nodes along one edge of the domain. This gives us a normalised wave speed of $\tilde{c}_N \approx 0.042$. The two wave speeds are similar, although planar waves appear to propagate faster across the fractal medium.

We have found, therefore, a qualitative and quantitative distinction between the propagation speeds of such travelling waves on the Euclidean domain and on the Sierpinski Gasket. Qualitatively, we find that there are (at least) two wave speeds on the Sierpinski Gasket, depending upon the propagation direction. Quantitatively, both of these speeds differ from that found in the Euclidean case. A possible route to understanding these differences would be to consider the linear wave equation

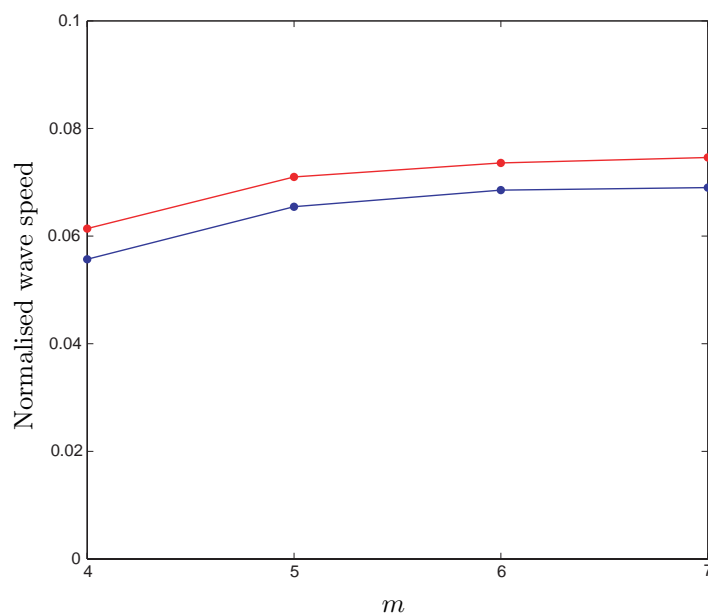


Figure 5.13: The normalised wave speed as a function of the level of approximation, m for a wave propagating from a corner to an edge (blue) and from an edge to a corner (red).

on the Sierpinski Gasket. This has been studied numerically in [14] and the wave speed has been shown to be infinite in this case. For our problem, however, the wave velocity is determined by the nonlinearity of the reaction kinetics. It might be useful therefore to set up an analogous asymptotic analysis on the Sierpinski gasket. This is an interesting but open problem as there is currently no well-defined definition of first order derivatives on p.c.f. self-similar sets apart from the normal derivative defined in Chapter 2. Another possible approach to understanding wave speeds might be to formulate the problem in weak form since we have used Dirichlet forms on the Sierpinski Gasket when defining the Laplacian.

5.7 Spiral Waves Solutions of a Modified FitzHugh-Nagumo System

5.7.1 Spirals Waves in the Myocardium

Electrical signals propagate through normal heart tissue in successive waves of electrical activity. Usually these impulses travel sufficiently quickly so that each cell will respond only once. These waves normally occur approximately once every 0.8s. Under certain conditions these planar waves can form or propagate abnormally, leading to *arrhythmia*. There are many different forms of cardiac arrhythmia of varying severity, one of the most frequently occurring and dangerous being so-called reentrant arrhythmias, caused by waves of excitation that repeatedly pass through the same tissue, forming a spiral. The mechanisms of the onset and stability of such spiral waves is the subject of extensive and ongoing investigation.

Spiral waves are waves of excitation that travel around a central, non-excitabile core re-exciting themselves. For this reason spiral waves are also referred to as reentrant waves. The formation of a spiral wave involves the generation of a semi-infinite wavefront in the plane. Since there are more excitable cells adjacent to the end of the

wavefront, the free end travels more slowly and curls back on itself to form a spiral. There are several possibilities as to how these broken waves can form, for example, if a propagating wave meets an obstacle such as a large vessel or a scar. Another possible cause of spiral waves is that impulses might propagate more slowly in certain areas of the heart. When part of the impulse arrives late, it is treated as a new excitation which can then spread backwards.

Ventricular tachycardia (VT) is one of many cardiac arrhythmia believed to be caused by a spiral-shaped reentrant wave front. VT is characterised by a fast heart-beat as spiral waves oscillate quickly with a period of about $0.2s$. Although not generally life-threatening in itself, VT often directly precedes the onset of ventricular fibrillation (V-Fib), which, if not treated immediately, results in death. V-Fib occurs when a spiral wave becomes unstable and degenerates into a chaotic pattern of many small waves. During fibrillation the ventricles quiver and writhe rather than contacting in unison, and so fail to pump blood around the body.

We can simulate a spiral wave on the domain $\Omega = [0, 50] \times [0, 50]$ with Neumann boundary conditions by solving the system (5.11) with initial condition consisting of a broken planar wave. In order to obtain the initial condition, a planar wave is simulated and allowed to propagate for a short time. Then we simply set $u = v = 0$ in the upper half of the domain and allow the wave to continue to propagate. Figure 5.14 show the potential u for such a wave when $\varepsilon^{-1} = 14$ and the consequent formation of the spiral wave.

Let us now look at the effect of the initial condition on the type of wave solutions arising. If, instead of truncating the wave in the middle, we set more or less of the plane to take zero value, we see that a spiral wave still forms but note that the centre of the spiral depends on where we set the plane wave to zero. Figure 5.15 illustrates this when the upper three quarters of the plane has been reset to $u = v = 0$.

Here, we have given a very brief overview of the existence of spiral waves in excitable media. A more detailed investigation of the circulation of excitation waves

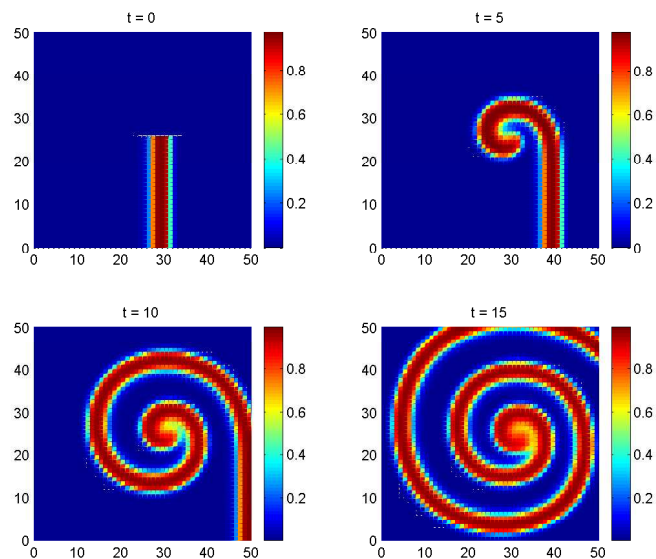


Figure 5.14: The potential, u , plotted for a rotating spiral wave. The initial condition in this case is a broken planar wave. A movie of this figure can be found on the accompanying CD, named FHNMov5.avi.

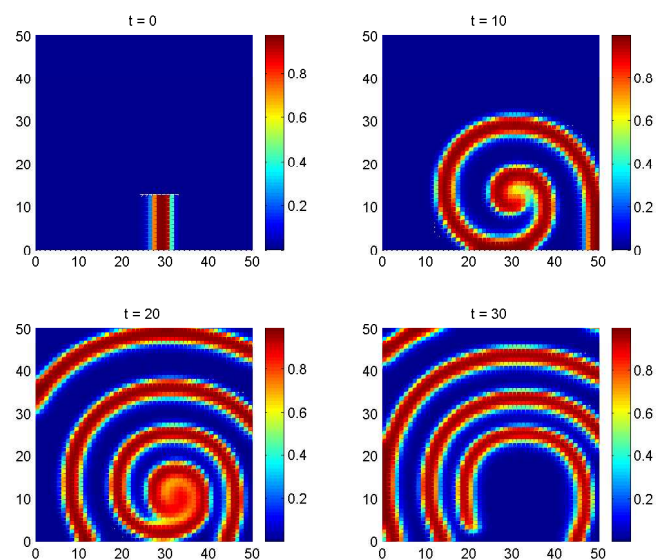


Figure 5.15: The potential, u , plotted for a skewed spiral wave. The initial condition in this case is a broken planar wave.

in two-dimensional excitable media is given by Zykov in [79]. For a review of the singular perturbation theory, [71] gives an overview of the general approach as well as a detailed analysis in the case of waves propagating in two spatial dimensions, including both target patterns and spirals rotating around a central hole or core.

The stability of rotating spiral waves has also proved to be of interest. In [5, 6] Barkley has carried out a linear stability analysis of such waves and shows that the transition between waves rotating rigidly around a circular core and so-called modulated rotating waves – whose tip paths meander – occurs via a Hopf bifurcation. Later work by Biktashev and Holden [9, 11] and by Nicol *et al* [4] has developed the theory of this meandering process in terms of the continuous symmetries of the system.

Spiral Break-up

It is widely accepted that the degeneration of ventricular tachycardia into ventricular fibrillation occurs when a spiral wave propagating in the myocardium spontaneously breaks up into many smaller excitation waves propagating in an erratic manner. The mechanism underlying spiral break-up is not well-understood although a possible cause [22] is that the wave front is slowed down by the refractoriness of the tissue ahead of the wave. The repolarisation wave (wave back) continues propagating at its original speed and therefore collides with the excitation front, causing it to break up.

In the model given in equations (5.11), whether a spiral wave will continue rotating or break up depends on the value of the parameter ε^{-1} . For given values of a and γ , there exists some critical value ε_c^{-1} such that for $\varepsilon^{-1} < \varepsilon_c^{-1}$ spiral break-up occurs. One can intuitively see why this is the case for two reasons. Firstly as ε^{-1} decreases the planar wave speed \tilde{c} slows, which may account for the collision of the wave front and wave back as described above. Secondly, as ε^{-1} decreases, the role of diffusion in the system becomes dominant over that of the reaction kinetics. Figure 5.16 shows the process of spiral break-up. The initial condition here is the same as in Figure

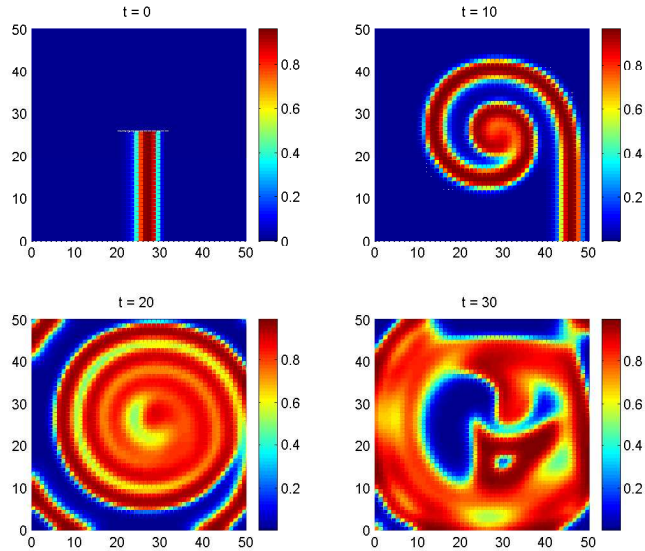


Figure 5.16: The potential, u , plotted for the break-up of a spiral wave. The initial condition in this case is a broken planar wave. A movie of this figure can be found on the accompanying CD, named FHNMov6.avi.

5.14, however, here we have taken $\varepsilon^{-1} = 12.5$.

The calculation of the precise value of ε_c^{-1} for which spiral break-up occurs is difficult. In [21], Mischaikow and coworkers introduce a new technique to measure the spatial-temporal complexity of patterns using algebraic topology. The system they used to illustrate this method is given by equations (5.11). They solved this on the domain $\Omega = [0, 80] \times [0, 80]$ with Neumann boundary conditions and the plotted the solutions for the potential u . The parameters α and γ were fixed at $\alpha = 0.75$, $\gamma = 0.06$ and ε^{-1} varied. In order to obtain a clear contrast between the excited and non-excited regions, the data were thresholded so that every point (x_i, y_j) for which $u(x_i, y_j) \geq 0.9$ (indicating the excited region) was shaded black, producing a complex pattern. Since the evolution in time of the excited region is of interest, Mischaikow *et al* represented the excited region by a set of voxels:

$$E = \{V_{i,j,k} | u(x_i, y_j, t_k) \geq 0.9\} \subseteq \mathbb{R}^3, \quad (5.34)$$

where $V_{i,j,k}$ is the voxel corresponding to the (i, j) th pixel at discrete time k . They then took time slices of the excited region. Let

$$T_{n,b} = \{V_{i,j,k} \in E | n \leq k \leq n + b\}. \quad (5.35)$$

Then, for fixed b , the time evolution of the pattern is given by the map from $T_{n,b}$ to $T_{n+1,b}$.

The topological complexity of such patterns can be quantified using algebraic topology. In particular, the topological features of the set $T_{n,b}$ can be partially characterised by calculating the Betti numbers $\beta_i(T_{n,b})$. Essentially, β_0 gives the number of connected components of a set, β_1 gives the number of tubes (corresponding to target waves), and β_2 gives the number of enclosed cavities. Since, in this case, they consider a three dimensional example (two spatial dimensions and time) $\beta_i = 0$ for $i \geq 3$.

Mischaikow *et al* have developed computer algorithms for the computation of the homology of cubical sets [38] meaning that the Betti numbers of such complicated patterns can be calculated. For the excitable media example discussed here, they find that β_2 is zero. This is due to the refractoriness of the medium: once excited, a region cannot be re-excited for some time afterwards. In order for a closed cavity to exist, an expanding target wave would have to change direction, which is clearly impossible. They also find that β_0 is piecewise constant and small which, again, is intuitively reasonable. The behaviour of β_1 , however, proves to be more interesting. The value of β_1 changes as tubes are created or destroyed. This behaviour occurs during the break-up of spiral waves. In the fourth frame of Figure 5.16 ($t = 30$) we see that a tube has been created.

Mischaikow *et al* considered the time series

$$B_{(10)} = \{\beta_1(m) | m = 1, 2, \dots, 10000\} \quad (5.36)$$

for different values of ε^{-1} (the subscript 10 indicates the width of the time slice). The

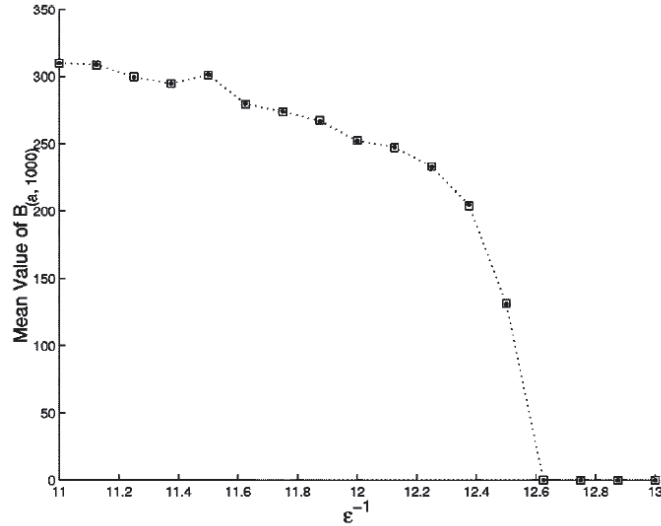


Figure 5.17: Mean values of the time series $B_{(10)}$ (squares), and the mean values of the time series $B_{(100)}$ (dots), as functions of ϵ^{-1} .

mean of β_1 , $\bar{\beta}_1$ was then plotted as a function of ϵ^{-1} , see Figure 5.17¹. We see that, as ϵ^{-1} increases through some critical value, $\bar{\beta}_1$ decreases to zero, where it remains. This result is interesting since the Betti numbers are non-negative integers so if their mean is zero then all the β_1 in the time series must be zero, so the excited region of the domain contains no tubes. It is therefore possible to determine the critical value of ϵ^{-1} for which spiral wave solutions of the modified FHN system become unstable and undergo spiral break-up. This critical value, ϵ_c^{-1} , was found to be between 12.5 and 12.625 so that for $\epsilon^{-1} > \epsilon_c^{-1}$ spiral waves are stable and for $\epsilon^{-1} < \epsilon_c^{-1}$ spiral waves are unstable and undergo break-up.

¹Reprinted figure with permission from [21]. Copyright 2004 by the American Physical Society.

5.7.2 Spirals on the Sierpinski Gasket

Spiral Waves

The work of Mischaikow *et al* demonstrates the generation of non-trivial topological structures on a Euclidean domain – that is, topology generated by the dynamics rather than the structure of the domain. What can be seen in this system in the case of a non-simply connected domain? In particular, what happens on the Sierpinski Gasket where the topology is extremely complex?

To compute an analogue of the spiral wave on the Sierpinski Gasket we simulate a planar wave as in Figure 5.9 and allow it to propagate for a short time before initiating a spiral by truncation. This is done by setting u and v to zero in the lower left order-one triangle K_1 . Figure 5.18 shows an analogue of a spiral wave on the Sierpinski Gasket after the initial plane wave was allowed to propagate until $t = 5$ before being truncated. This is a wave, of fixed amplitude, which travels round the central triangular hole. This wave, unless disturbed, appears to propagate without changing in velocity or form.

We can think of this kind of wave as a sequence of plane waves, which propagate across subgaskets. For example, consider Figure 5.18 at $t = 4$. The node q_1 can be thought of as being excited sufficiently to initiate a wave which propagates across the subgasket K_2 (in this configuration the subgasket K_3 is in a refractory state). When the wave reaches the base of K_2 it is annihilated (reflection is prevented by the refractoriness so the local dynamics on the base nodes simply cycle back to the fixed point ($u = 0, v = 0$)). However, diffusion couples the vertex q_3 to the subgasket K_1 so the dynamics at this vertex initiate a planar travelling wave which propagates across K_1 . This process is thus repeated in the cyclic sequence of subgaskets $K_1 \rightarrow K_3 \rightarrow K_2 \rightarrow K_1 \rightarrow \dots$ giving a stable analogue of a spiral wave.

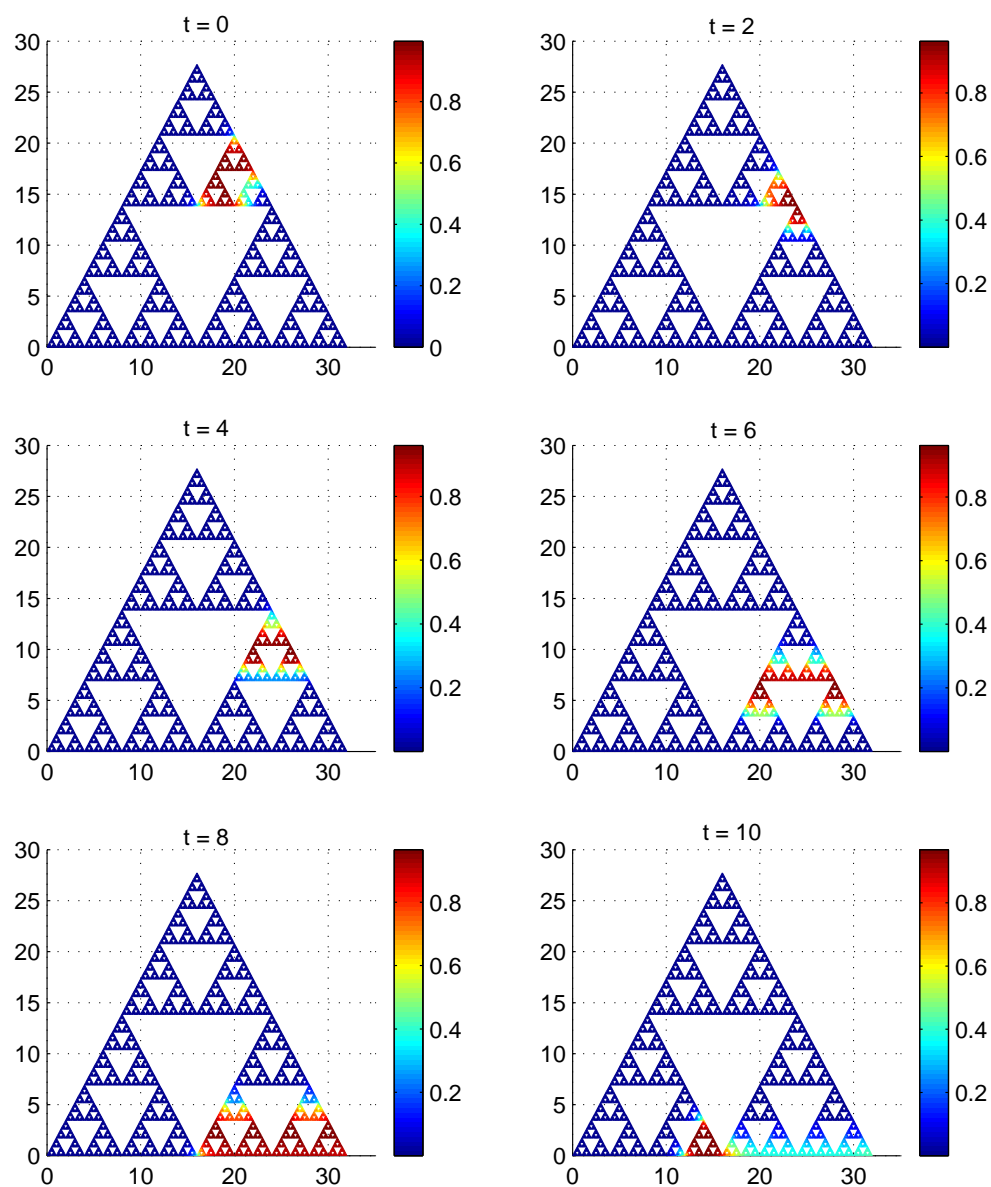


Figure 5.18: The potential, u , plotted for the analogue of a spiral wave. The times shown are after the truncation of a planar wave, propagating for 5 time units. A movie of this figure can be found on the accompanying CD, named FHNMov7.avi.

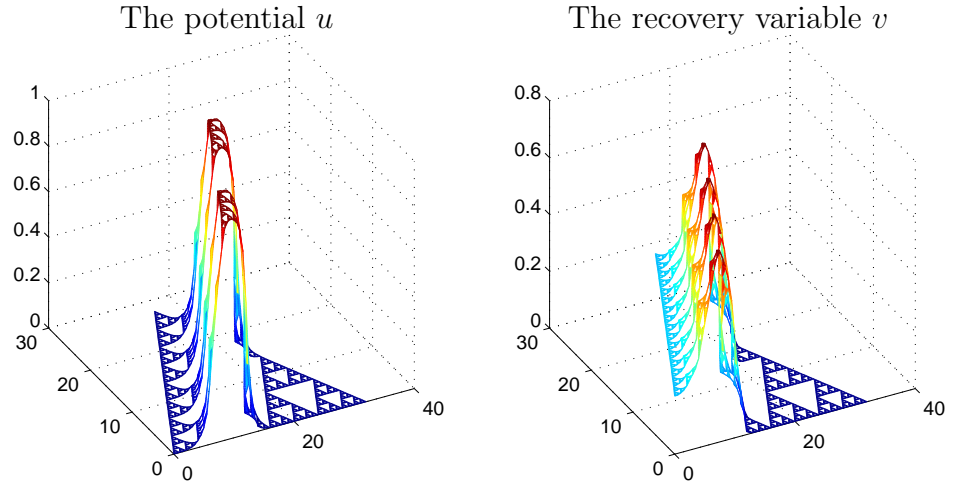


Figure 5.19: The position of the planar wave at $t = 4.5$.

Hints of Complexity

We now examine the second type of spiral wave seen in Section 5.7.1, that is, when the initial planar wave is not truncated in its centre so the resulting spiral wave becomes skewed. To replicate this result on the Sierpinski Gasket, we follow the same procedure as in the case of the regular spiral. However, as well as setting u and v to zero in K_1 , we also prescribe zero values on K_{31} . Now the wave can not only propagate forwards in its original direction, it should also be able to travel backwards.

To initiate the wave in this instance, we allow the initial planar wave to propagate until the maximum value of the potential has travelled exactly one quarter of the way across the gasket so it has just entered K_{32} and K_{12} . This happens at $t = 4.5$. The wave profiles for u and v in this case are shown in Figure 5.19. Then we truncate the wave as described and allow the wave to continue across the domain. The evolution of this wave at discrete time intervals is shown in Figure 5.20. Now we see that the wave does indeed propagate backwards into the region that was reset to zero (compare Figure 5.20 with Figure 5.18).

In this case we effectively have a number of small planar waves propagating in different directions around the central hole of each order-one subgasket. These waves

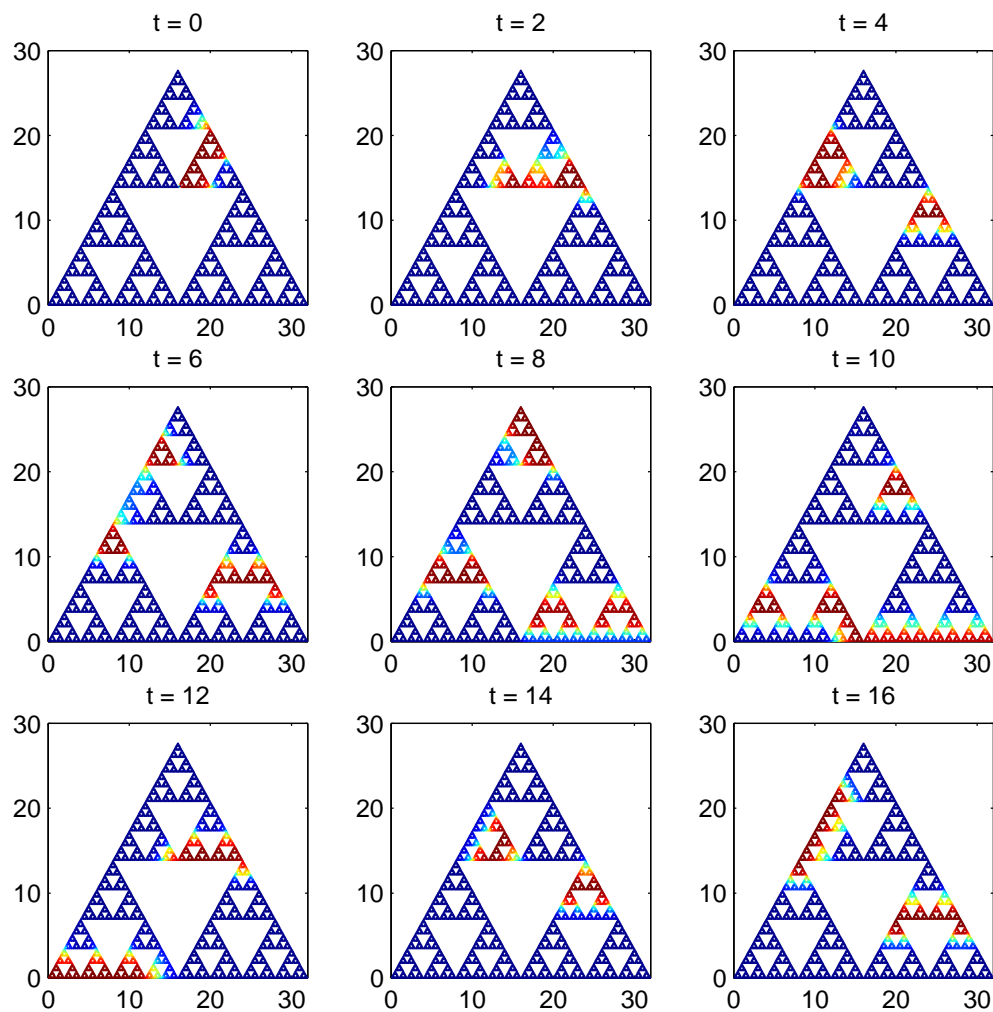


Figure 5.20: The potential, u , plotted for the analogue of a spiral wave. The times shown are after the truncation of a planar wave, propagating for 4.5 time units. A movie of this figure can be found on the accompanying CD, named FHNMov8.avi.

split into two at the junction points between the order-two subgaskets. At time $t = 10$ we see two waves have entered K_1 from different directions. Due to the Neumann boundary conditions and the fact that the parts of the gasket behind these waves are in recovery, these waves are annihilated. This leaves us with two wave fronts that, at $t = 14$, are in a similar position on the gasket to those at $t = 4$. By defining unit time as the time taken for an excitation front to propagate over a fixed region of the gasket, it can be shown that the wave propagation in this case becomes periodic after an initial transient.

The behaviour of the wave shown in Figure 5.20 can be interpreted as follows. The analogue of a spiral wave is propagating around the central hole of the order-one triangle K_3 . Each time this wave meets one of the junction points q_1 or q_2 , other plane waves are initiated which propagate across K_1 and K_2 . When these plane waves collide, they die out. With the correct choice of initial condition and value of ε , it should be possible to initiate spiral waves that travel around the central hole of any order- m triangle of the gasket, K_w , $|w| = m$. At each order- m junction point, plane waves will propagate into the neighbouring subgaskets. The ultimate fate of these waves could be that they destroy each other as is the case here, however, there is clearly the possibility of much more complex interactions.

This behaviour is reminiscent of certain patterns seen in the “Game of Life” invented by the mathematician John Conway in 1970. Life is an example of a cellular automaton and is played on a grid of square cells. Each cell is in one of two states – alive or dead. The evolution of the game from an initial configuration of cells then depends on a particular set of rules.

The Game of Life is one of the simplest examples of a system that exhibits “emergent complexity” (for more information on Life and examples of many patterns that occur, see [73]). One of the most interesting patterns seen in Life is that of a glider – a small pattern which repetitively rearranges itself and, in doing so, moves across the grid. There also exist so-called “glider guns”, which emit gliders at regular intervals.

It is possible to arrange the Game of Life so that the gliders interact to perform computations. In fact, it has been shown (see [61]) that the Game of Life can emulate a universal Turing machine: anything that can be computed via an algorithm can be computed with Conway's Game of Life.

We have seen that there is a sense in which the solution of the FHN system on the Sierpinski Gasket can behave like a cellular automaton: a spiral wave travels around K_3 and periodically gives rise to propagating plane waves in a way that suggests an analogy with glider guns. With this observation comes the possibility that reaction-diffusion systems on the Sierpinski Gasket might be capable of complex computational tasks.

Unstable Behaviour

For our next simulation we consider the same situation but this time we allow the plane wave to propagate a little bit further across the gasket before truncating. Figure 5.21 shows this when the initial planar wave is truncated at $t = 5$. Now we see different behaviour. Initially, as we expect, the wave propagates forward in its original direction and backwards into K_{31} , which has been reset to zero. However, shortly after this has occurred, this part of the wave appears to propagate in two directions, back into K_{32} , producing an extra small plane wave. As we proceed in time, pairs of these small plane waves collide and destroy each other. Eventually, we are left with a single wave of excitation which travels around the central hole as we saw in Figure 5.18.

The unusual behaviour seen here occurs around the junction point between K_{31} and K_{32} between times $t = 0$ and $t = 4$. To investigate this behaviour further, we consider the junction point between K_{31} and K_{32} and three vertices close to it. We label these vertices a, b, c and d , see Figure 5.22. We are interested in how the values of u and v change with time at these nodes and in how this differs to the behaviour seen in the previous simulation. We therefore consider the phase trajectories in both cases at each of these nodes. We plot u against v for times between $t = 0$ and $t = 4$

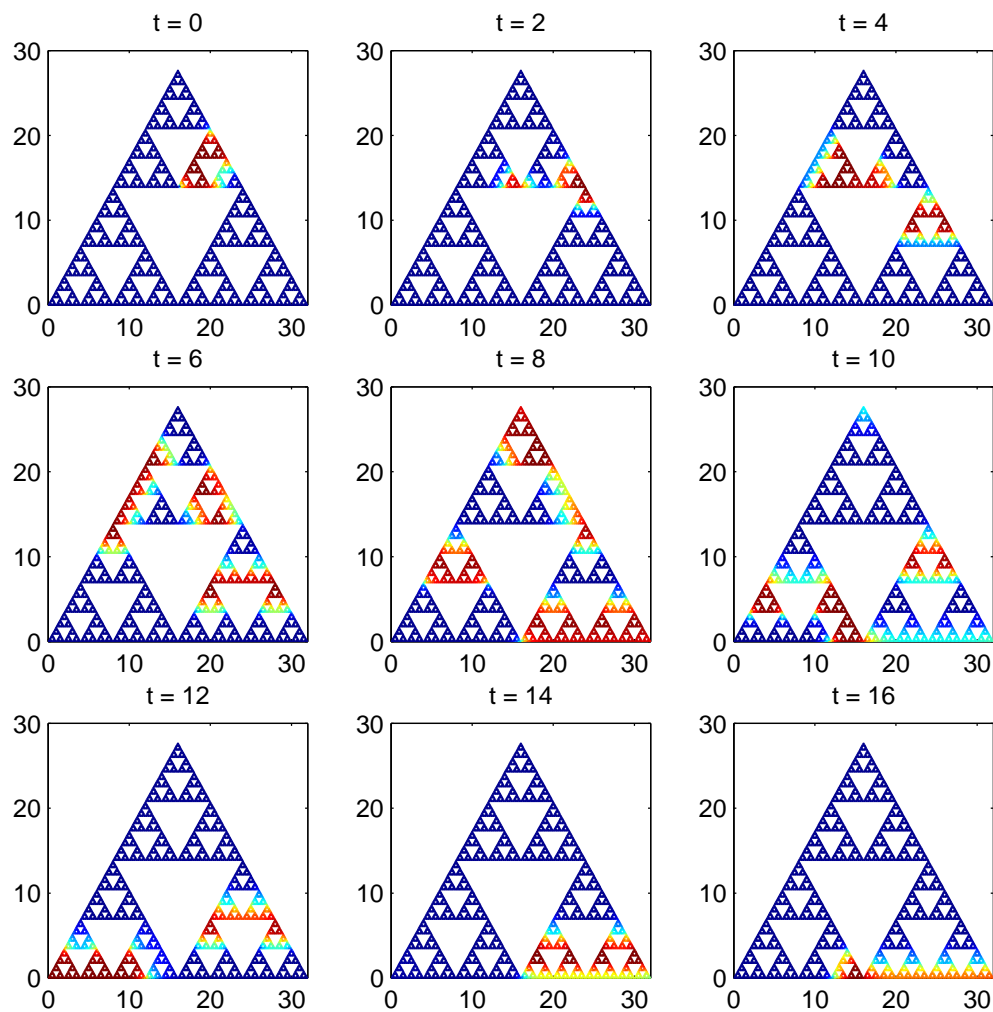


Figure 5.21: The potential, u , plotted for the analogue of a spiral wave. The times shown are after the truncation of a planar wave, propagating for 5 time units. A movie of this figure can be found on the accompanying CD, named FHNMOV9.avi.

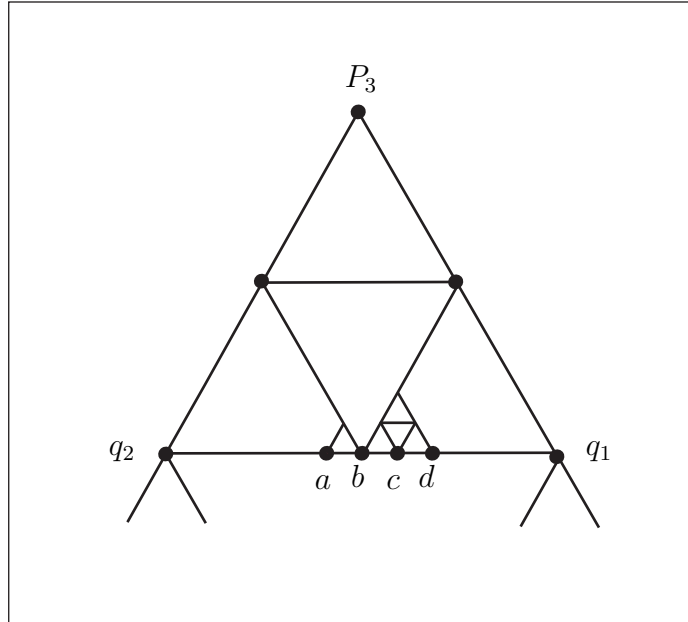


Figure 5.22: The location of the nodes we are interested in, a, b, c and d .

since this is the time interval in which this interesting behaviour occurs.

Figure 5.23 shows the phase space for the nodes a and b (nodes that have initially been reset to zero) in both cases. Similarly, Figure 5.24 shows the phase space for the nodes c and d (initially in the excited state). In both of these figures, the left hand column shows the first case where the initial planar wave is truncated at $t = 4.5$, and the right hand column shows the case where the planar wave is truncated at $t = 5$. The red dots indicate the initial values.

Figures 5.25 and 5.26 show the values of u and v against time in each of these cases. We see that there is a marked difference between the left and right columns of these figures, although this difference is far more pronounced when comparing the vertices c and d in the two cases.

We begin by considering the nodes a and b . Initially, these nodes have been reset to zero and are at rest. Two of the neighbours of b , however, are in the excited state. Very quickly the diffusion causes u to rise rapidly, exciting node b . Soon afterwards,

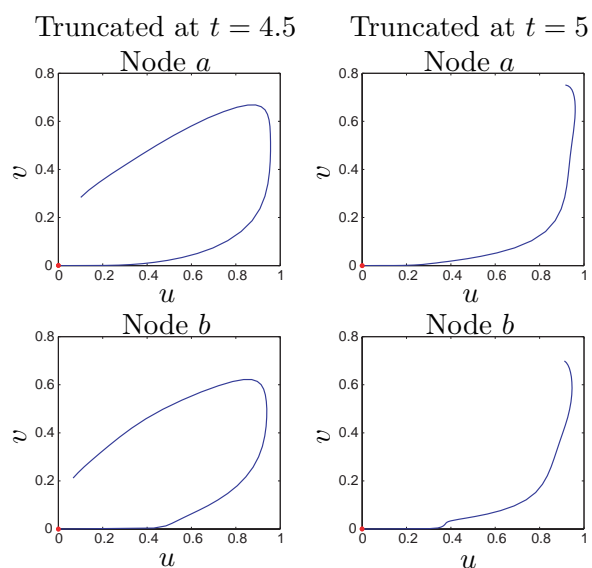


Figure 5.23: The phase space for $t = 0$ to $t = 4$ for the nodes a and b . In the left had column the planar wave has been truncated at $t = 4.5$. In the right hand column the planar wave has been truncated at $t = 5$.

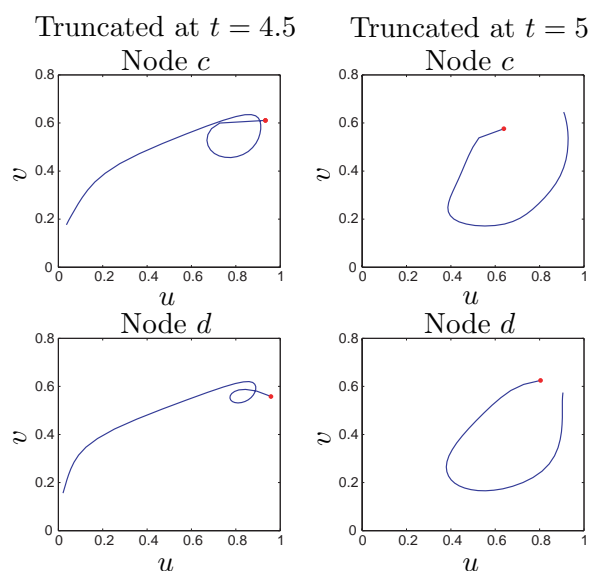


Figure 5.24: The phase space for $t = 0$ to $t = 4$ for the nodes c and d . In the left had column the planar wave has been truncated at $t = 4.5$. In the right hand column the planar wave has been truncated at $t = 5$.

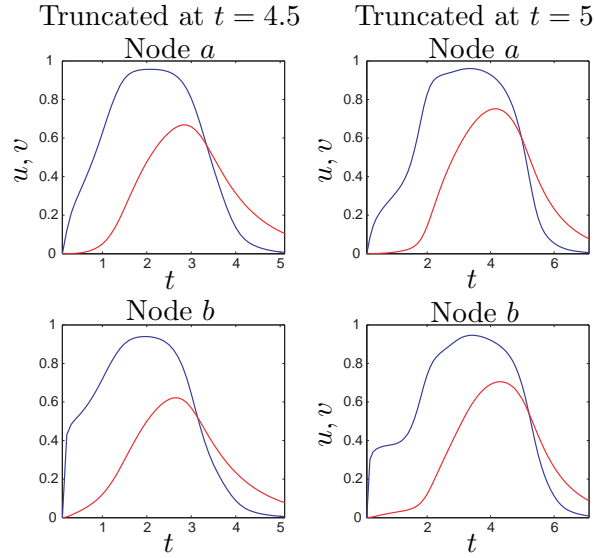


Figure 5.25: The u (blue) and v (red) values plotted against time for the nodes a and b . In the left hand column the planar wave has been truncated at $t = 4.5$. In the right hand column the planar wave has been truncated at $t = 5$.

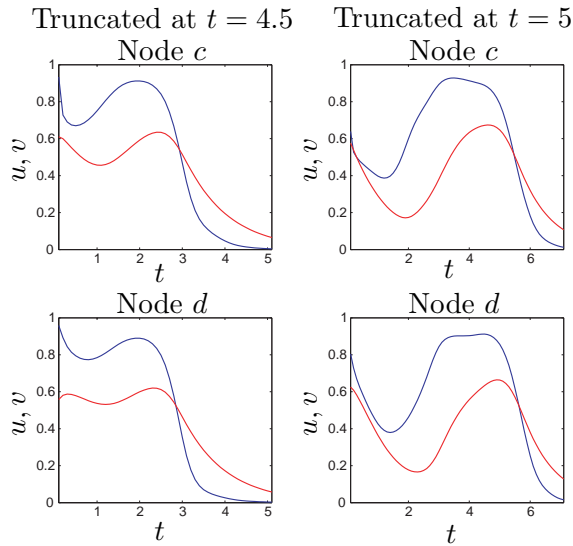
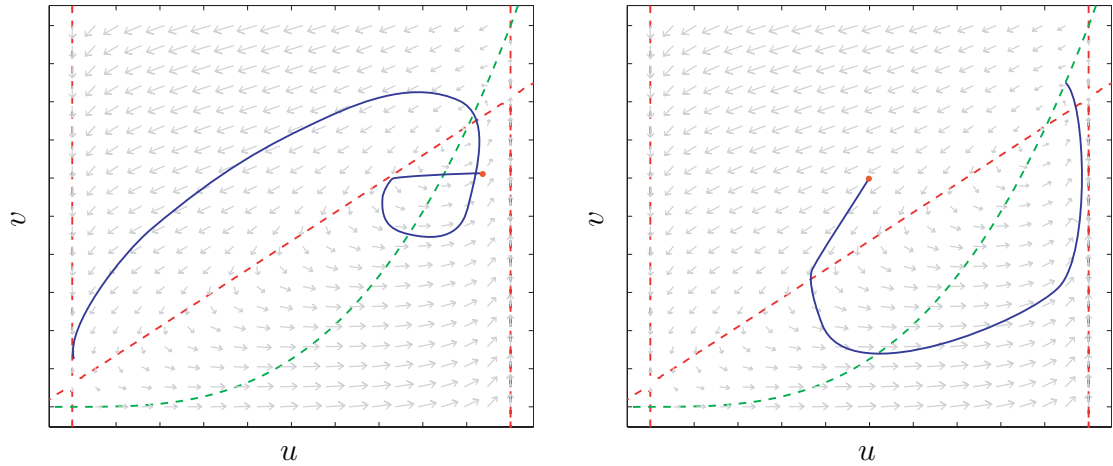


Figure 5.26: The u (blue) and v (red) values plotted against time for the nodes c and d . In the left hand column the planar wave has been truncated at $t = 4.5$. In the right hand column the planar wave has been truncated at $t = 5$.

a is also excited. The phase portraits for these nodes are exactly as we would expect: the increase in u activates v , which begins to increase soon afterwards. The increase in v then inhibits u , which plateaus and then begins to decrease as v reaches its maximum. The decrease in u also causes v to decrease and both variables return to the rest state at the origin. The behaviour seen here is essentially the same in both cases, although, when the plane wave is truncated at a later time, the value of u at nodes neighbouring b is lower so the diffusion takes a longer time to push b above the threshold.

Now we consider the nodes c and d . Initially these nodes are in the excited state so we would expect the u and v values at these nodes to return directly to the rest state at the origin. This, however, is not the case. When the planar wave is truncated at $t = 4.5$, we see the trajectories make a small loop before beginning to return to rest. In the case where the plane wave is truncated at a later time the nodes in question seem to become re-excited rather than returning to rest. Again, the onset of this behaviour is explained in terms of diffusion. Since initially node c has a neighbour that has been reset to zero, the diffusion quickly decreases the value of u at this node. This implies that when the dynamics come into play, the initial value is in a different area of the phase space.

For our parameter values, the reaction kinetics of the system are such that, in the absence of diffusion, there is a fixed point at $(u, v) \approx (0.823, 0.557)$, which is an unstable focus. So, when the diffusion initially shifts the value of u , the trajectories follow this orbit, forming a loop before returning to the rest state. Figure 5.27 shows the nullclines and the vector field of the system without diffusion and two possible phase trajectories accounting for the behaviour of node c in Figure 5.24. In the first case we considered, the loop is small and the node quickly returns to the rest state. In the second case, the node undergoes a larger excursion, and therefore takes a much longer time to return to the rest state. This is why we see such different behaviour in the two cases considered here.



(a) Here the plane wave is truncated at $t = 4.5$.

(b) Here the plane wave is truncated at $t = 5$.

Figure 5.27: A comparison between actual phase trajectories (with diffusion) and the vector field of the diffusionless FHN system.

We first recall that, if the value of v at a node is high, then the node is refractory and therefore not susceptible to re-excitation. In our first case, since the loop is small, node c is re-excited quickly. By the time node d is recovered, node c has returned to the rest state and does excite node d . In our second case, however, by the time node d has recovered, node c is still in the excited state. This causes a wave of excitation to be initiated from node c in the clockwise direction. We can see this in Figure 5.28 where we plot the (u, v) values on node c against the value of v on node d . In the right hand plot we see that large values of $u(c)$ can be found when $v(d)$ is small. This is in marked contrast to the left hand plot.

Spiral Break-up on the Sierpinski Gasket

It is not obvious what is meant by *spiral break-up* on the Sierpinski Gasket as our domain is full of holes. We can, however, study the effects of reducing the parameter ε^{-1} . Recall that on the Euclidean case, it was shown that spiral break-up occurs for values of ε^{-1} less than some $\varepsilon_c^{-1} \approx 12.5$.

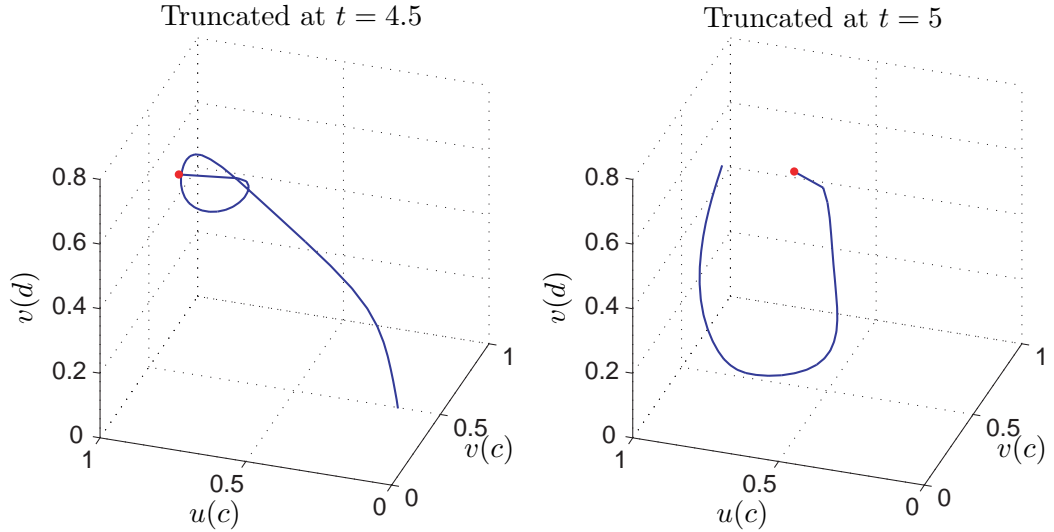


Figure 5.28: The relationship between the state of node c and the recovery variable on node d .

We begin by repeating the simulation shown in Figure 5.18, this time with $\varepsilon^{-1} = 12.5$. We note here that prior to truncation, the planar wave propagated with $\varepsilon^{-1} = 14$ for 5 time units to ensure the same initial condition for the two simulations. The wave propagation in this case is shown in Figure 5.29. We see that when the wave has passed through the junction point q_1 it seems to be reflected back again into K_3 as well as continuing to propagating in its original direction. This behaviour is reminiscent of that seen in Figure 5.21.

As in that case, we can consider the phase space at this node for times $t = 0$ to $t = 10$. The trajectories once again form a loop before returning to the rest state. This gives the neighbouring node behind the wave front (node n) enough time to recover before being re-excited by the node q_2 , thus initiating a wave in the anticlockwise direction. The phase space at node q_2 is shown on the left of Figure 5.30. The relationship between the value of v at node n and $u(q_2)$ and $v(q_2)$ is shown on the right of Figure 5.30.

This demonstrates that a similar dynamical process accounts for the production

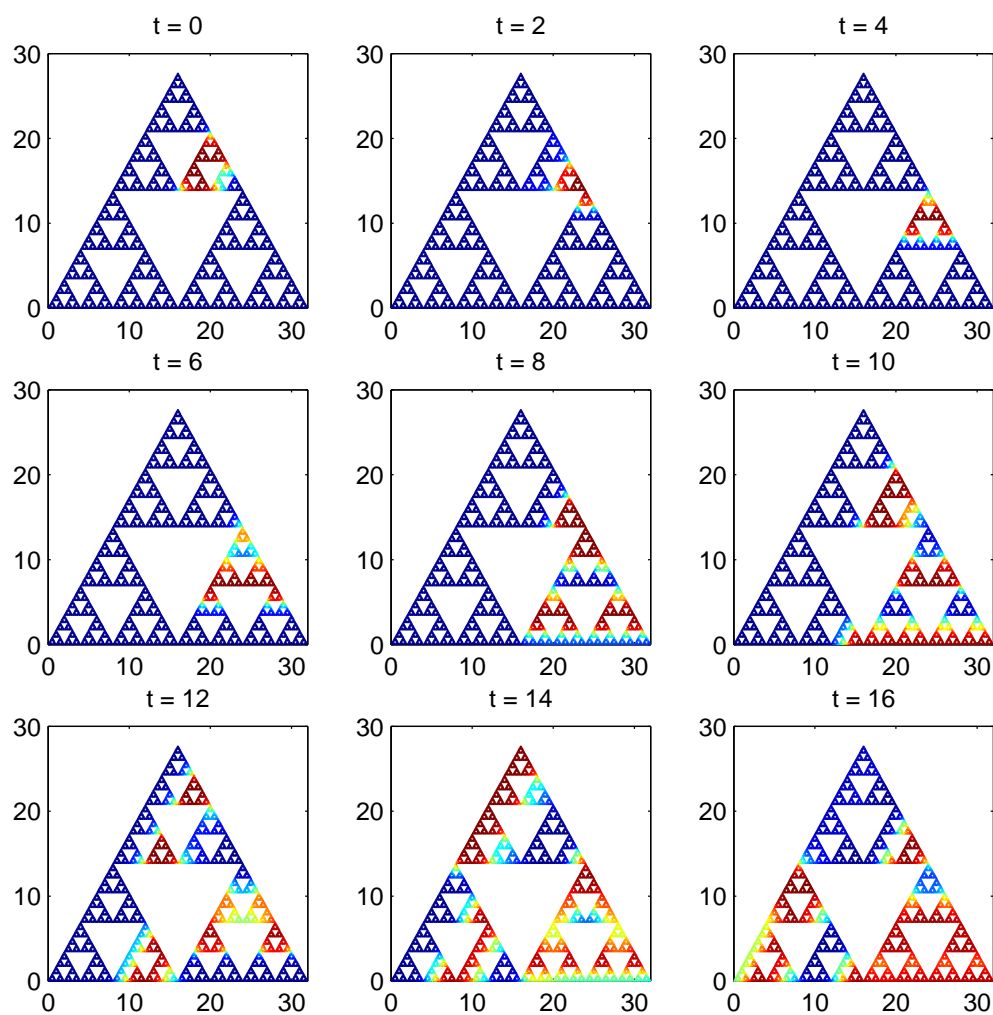


Figure 5.29: The initial condition here is a plane wave reset to $K_1 = 0$ after propagating until $t = 5$. $\varepsilon^{-1} = 12.5$. A movie of this figure can be found on the accompanying CD, named FHNMov10.avi.

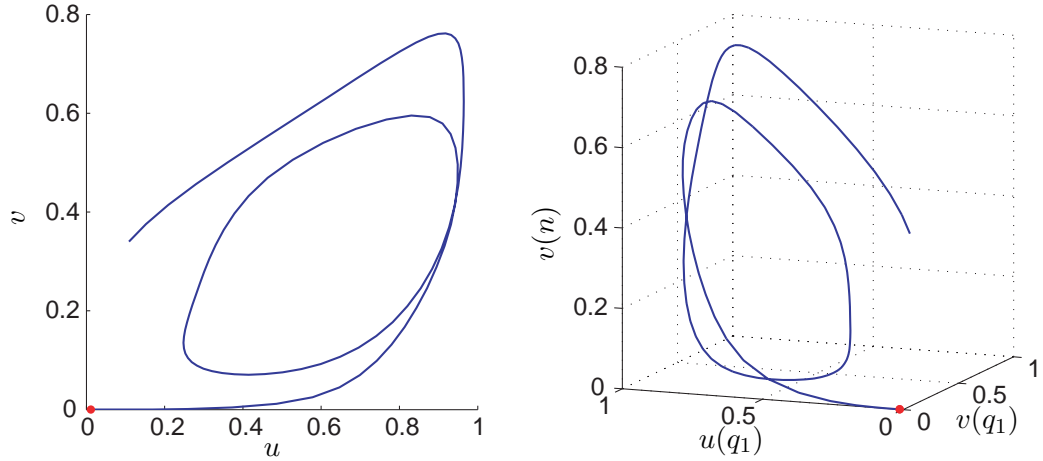


Figure 5.30: The left hand plot shows the state of node q_1 and the right hand plot shows this state in relation to the value of the recovery variable at node n .

of a reflected wave in both this case and that described earlier (see Figure 5.21). The underlying mechanism is, however, different. In the present case, the extra diffusion makes it far less useful to compare the actual local phase space trajectory with the vector field of the FitzHugh-Nagumo system. However, if we compare trajectories for the two cases we see that analogous things are happening.

We have demonstrated how a local effect can disturb the simple patterns that result from travelling waves on the Sierpinski Gasket. More generally, however, there is a great potential for complex behaviour in this system. For example, we see in Figure 5.31, that contrary to expectation, the regular oscillation shown in Figure 5.20 is preserved when ε^{-1} is reduced. A further reduction of ε^{-1} , however, gives the complicated spatio-temporal patterns shown in Figure 5.32. This suggests that global behaviour on the gasket such as the mutual destruction of counter propagating waves can lend extra stability in some circumstances. Clearly we have just begun to scratch the surface here.

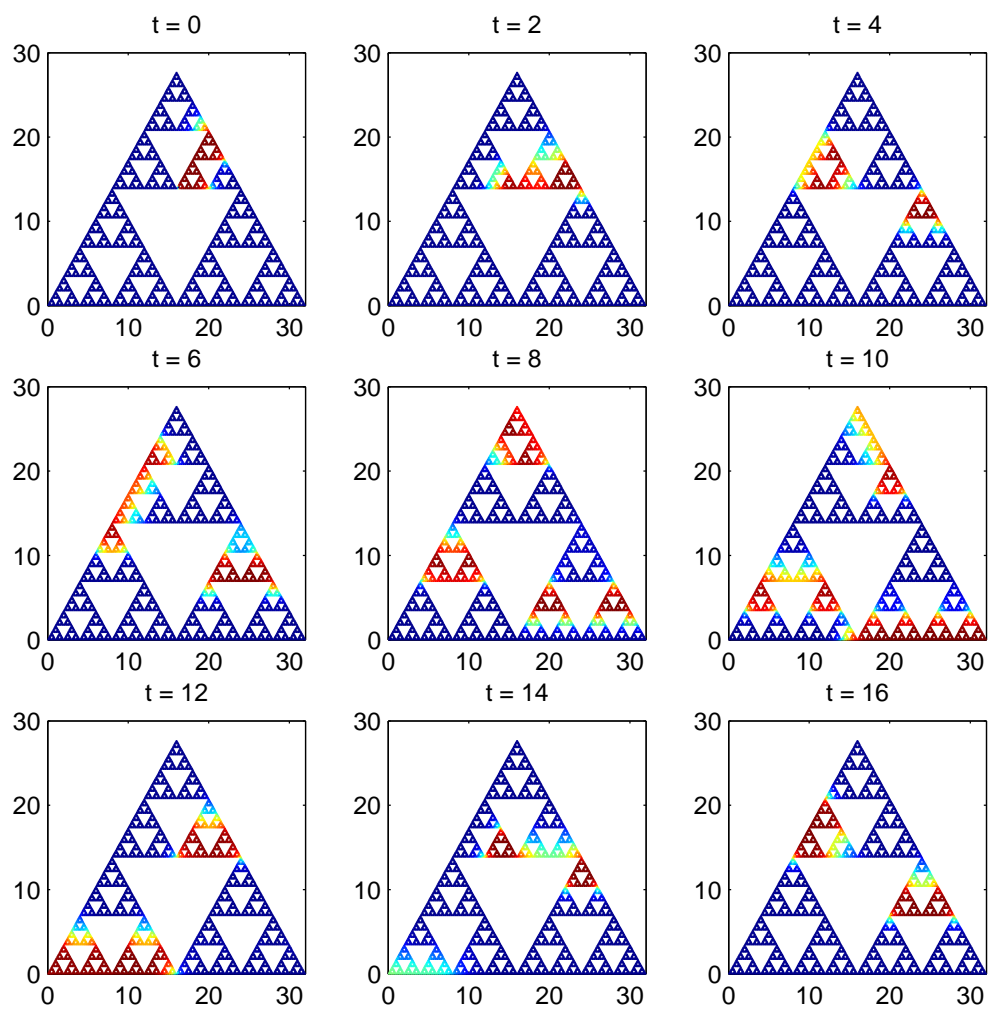


Figure 5.31: The initial condition here is a plane wave reset to $K_1 = 0$ and $K_{31} = 0$ after propagating until $t = 4.5$. $\varepsilon^{-1} = 12.5$.

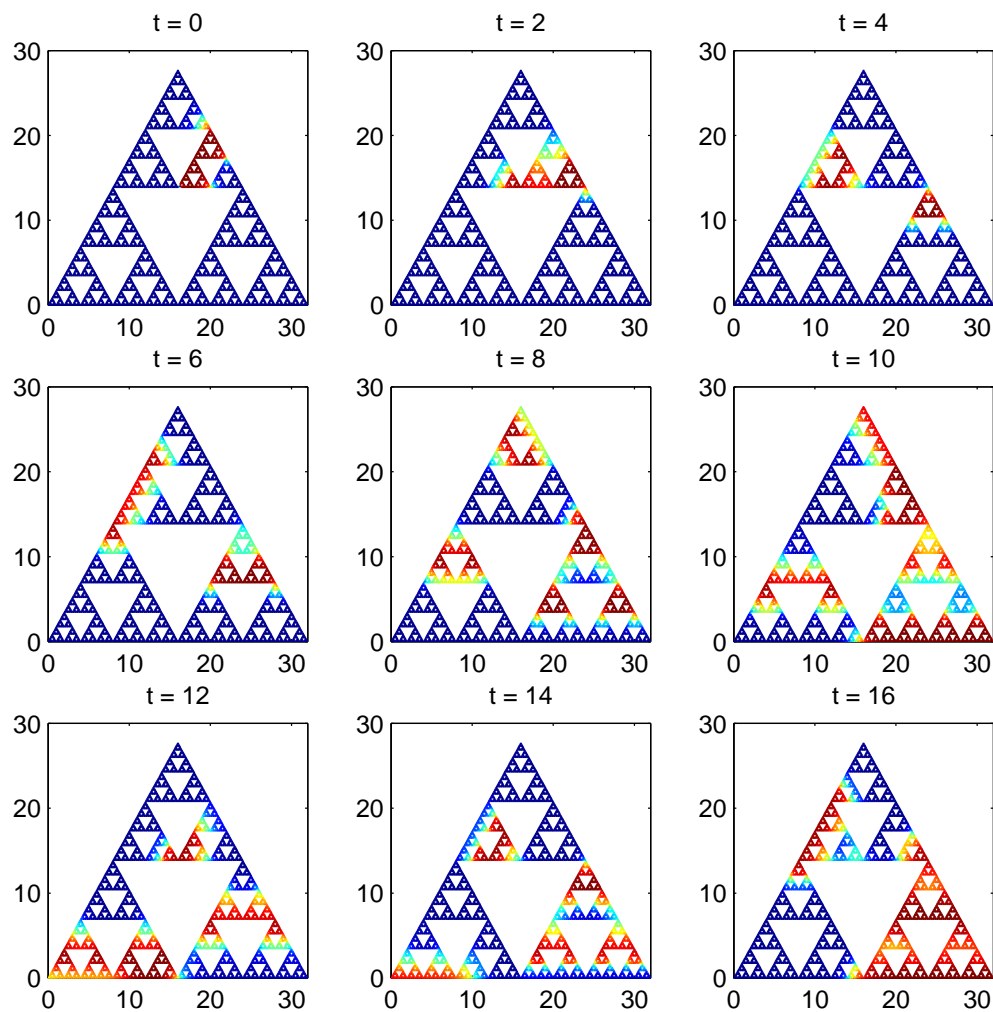


Figure 5.32: The initial condition here is a plane wave reset to $K_1 = 0$ and $K_{31} = 0$ after propagating until $t = 4.5$. $\varepsilon^{-1} = 12$. A movie of this figure can be found on the accompanying CD, named FHNMov11.avi.

Chapter 6

Conclusions and Further Work

In this thesis we have considered a number of dynamical processes that, in real life, can be seen to be occurring on domains that are spatially complex. The recent advances in the area on Analysis on Fractals mean that we are now able to define differential operators on a class of such sets. We can, therefore, solve PDEs modelling such processes on these domains with a view to understanding how the spatial complexity affects the phenomena seen.

We began by giving a review of the literature concerned with defining Laplacians on p.c.f. self-similar sets, primarily the Sierpinski Gasket. We then discussed the properties of the eigenvalues and eigenfunctions of the Laplacian on SG. In particular we described the decimation procedure (unique to the Sierpinski Gasket), which relates the eigenvalues and eigenfunctions of different order graph approximations to SG to each other. This was carried out for the Laplacian on SG with both Dirichlet and Neumann boundary conditions. We have also discussed the existence of localised eigenfunctions, which do not exist in the case of a Euclidean domain, and shown how to construct such functions. The main part of this thesis has been concerned with solving neural models on the Sierpinski Gasket. Our starting point was the linear cable equation which we then extended to a more sophisticated system.

When studying the cable equation in this context we see phenomena that arise

purely from the complexity of the domain (since this is a linear system). In the cases of both Dirichlet and Neumann boundary conditions, we have derived a scaling law, which enables us to see asymptotic behaviour that is independent of the order of approximation to the Sierpinski Gasket.

Since the cable equation is only relevant for passive processes in neurons we then introduced a system of equations, which provides a good qualitative model of the behaviour of excitable media such as nerve fibres and cardiac tissue. This is known as the FitzHugh-Nagumo system. In the case of a Euclidean domain we discussed the types of solutions that exist and gave a brief overview of research carried out in this area, including using an asymptotic analysis to determine the wave speed of travelling wave solutions of this system. We then carried out an analogous analysis where the domain is the Sierpinski Gasket. We saw that the gasket can support travelling waves, which (qualitatively at least) behave in a similar fashion to those seen in the Euclidean case. We then calculated the velocities of waves propagating across SG numerically and showed, interestingly, that the Sierpinski Gasket can support at least two different wave speeds.

We have discussed the existence of spiral waves on a Euclidean domain and how the break-up of these waves propagating in cardiac tissue can cause the onset of certain cardiac arrhythmia. Again, we have computed an analogy of a spiral wave on the Sierpinski gasket and investigated its behaviour. We have found that a “spiral wave” on the Sierpinski Gasket is just a cyclic sequence of planar waves propagating over subgaskets. This is a nice result, as we do not need to consider the effects of curvature of the wavefront. We have also seen how complex behaviour can arise, which is unique to the solution of the system on the Sierpinski Gasket. In particular we have seen phenomena which are reminiscent of behaviour seen in certain cellular automata.

As a result of the research carried out to produce this thesis, many questions arise which suggest further work that may be done. In Chapter 2, we discussed

Hata's tree-like set, which, initially seemed like a good choice of domain when solving neural systems on p.c.f. self-similar sets. We found, however, that Kigami's notion of boundary gave rise to harmonic functions that became trivially constant over the whole tree. We would therefore like to be able to construct a p.c.f. fractal tree whose boundary is identified as the tips of the branches. We must be able to uniquely identify the boundary points in this case. It may then be possible to apply this theory to certain fields of neuroscience.

Recently, research has been carried out by Broomhead and coworkers, [12], on the development of an iterated function system approach to signal processing. They have studied the effect of driving the cable equation with a random sequence of pulses and shown that this model has a unique attractor. A similar analysis could be carried out on the Sierpinski Gasket. Here, the spectrum of the Laplacian might be expected to enter the expression for the Hausdorff dimension of the attractor in an interesting way.

When considering the FitzHugh-Nagumo system on the Sierpinski Gasket, we feel that there are many possible directions in which this could go. We feel we have only investigated a small sample of the phenomena which may arise in this context. We have seen lots of complex behaviour and managed to account for the existence of some of this. It would be advantageous to set up an analogous asymptotic theory of wave velocities on the Sierpinski Gasket, however this would require knowledge of first order derivatives on SG, which have yet to be defined. A possible application of solving the FitzHugh-Nagumo system on the Sierpinski Gasket may be to use this as a cellular automaton that can carry out computations. Further investigation would be required as to the level of complex behaviour that can be seen in the FHN system such as spiral waves travelling around smaller subgaskets and giving rise to glider analogues.

Bibliography

- [1] J. Abdulbake, A. Mulholland, and J. Gomatam. A renormalization approach to reaction-diffusion processes on fractals. *Fractals*, 11(4):315–330, 2003.
- [2] J. Abdulbake, A. Mulholland, and J. Gomatam. Existence and stability of reaction-diffusion waves on a fractal lattice. *Chaos, Solitons & Fractals*, 20(4):799–814, 2004.
- [3] O.M. Ashford. *Prophet or Professor? The Life and Work of Lewis Fry Richardson*. Adam Hilger Ltd., 1985.
- [4] P. Ashwin, I. Melbourne, and M. Nicol. Drift bifurcations of relative equilibria and transitions of spiral waves. *Nonlinearity*, 12:741–755, 1999.
- [5] D. Barkley. Linear stability analysis of rotating spiral waves in excitable media. *Phys. Rev. Lett.*, 68(13), 1992.
- [6] D. Barkley. Euclidean symmetry and the dynamics of rotating spiral waves. *Phys. Rev. Lett.*, 72(1), 1994.
- [7] M.T. Barlow and J. Kigami. Localized eigenfunctions of the Laplacian on p.c.f. self-similar sets. *J. London. Math. Soc. (2)*, 56:320–332, 1997.
- [8] Michael Barnsley. *Fractals Everywhere*. Academic Press, San Diego, 2nd edition, 1993.

BIBLIOGRAPHY

- [9] V.N. Biktashev and A.V. Holden. Deterministic Brownian motion in the hypermeander of spiral waves. *Physica D*, 116:342–354, 1998.
- [10] V.N. Biktashev and A.V. Holden. Re-entrant waves and their elimination in a model of mammalian ventricular tissue. *Chaos*, 8:46–56, 1998.
- [11] V.N. Biktashev, A.V. Holden, and E.V. Nikolaev. Spiral wave meander and symmetry of the plane. *Int. J. Bifurc. & Chaos*, 6(12):2433–2440, 1996.
- [12] D.S. Broomhead, J.P. Huke, J. Motaldi, and M.R. Muldoon. The randomly forced cable equation. (In preparation).
- [13] Chi-Tsong Chen. *Introduction to Linear Systems Theory*. Holt, Rinehart and Winston Series in Electrical Engineering, Electronics, and Systems. Holt, Rinehart and Winston, Inc., 1970.
- [14] K. Dalrymple, R. S. Strichatz, and J. P. Vinson. Fractal differential equations on the Sierpinski gasket. *J. Fourier Anal. Appl.*, 5:203–184, 1999.
- [15] P. Diaconis and D. Freedman. Iterated random functions. *SIAM Rev.*, 41(1):45–76, 1999.
- [16] A.T. Winfree (Guest Editor). Focus issue: Fibrillation in normal ventricular myocardium. *Chaos*, 8:1–241, 1998.
- [17] Kenneth Falconer. *Fractal Geometry: Mathematical Foundations and Applications*. John Wiley & Sons, 1990.
- [18] R.J. Field, E. Koros, and R.M. Noyes. Oscillations in chemical systems ii, thorough analysis of temporal oscillations in the bromate-cerium-malonic acid system. *J. Am. Chem. Soc.*, 94:8649–8664, 1972.
- [19] R. FitzHugh. Impulses and physiological states in theoretical models of nerve membrane. *Biophysical J.*, 1:445–466, 1961.

BIBLIOGRAPHY

- [20] M. Fukushima and T. Shima. On a spectral analysis for the Sierpinski gasket. *Potential Analysis*, 1992.
- [21] M. Gameiro, W. Kalies, and K. Mischaikow. Topological characterization of spatial-temporal chaos. *Phys. Rev. E*, 70(3), 2004.
- [22] M. Gerhardt, H. Schuster, and J. J. Tyson. A cellular automation of excitable media including curvature and dispersion. *Science*, 247(4950):1563–1566, 1990.
- [23] G. Gerstein and B. Mandelbrot. Random walk models for the spike activity of a single neuron. *Biophys. J.*, 4:41–67, 1964.
- [24] M. Gibbons and A. Raj. The finite element method on the Sierpinski gasket website. <http://www.mathlab.cornell.edu/~gibbons/index.html>, 1999.
- [25] M. Gibbons, A. Raj, and R. S. Strichartz. The finite element method on the Sierpinski gasket. *Constr. Approx.*, 17:561–588, 2001.
- [26] S. Goldstein. Random walks and diffusions on fractals. In H. Kesten, editor, *Percolation Theory and Ergodic Theory of Infinite Particle Systems*, volume 8 of *IMA Math. Appl.*, pages 121–129. Springer, 1987.
- [27] M. Hata. On the structure of self-similar sets. *Jpn, J. Appl. Math.*, 3:381–414, 1985.
- [28] S. Havlin, L.A.N. Amaral, Y. Ashkenazy, A.L. Goldberger, P.Ch. Ivanov, C.-K. Peng, and H.E. Stanley. Application of statistical physics to heartbeat diagnosis. *Physica A*, 274:99–110, 1999.
- [29] A.L. Hodgkin and A.F. Huxley. The components of membrane conductance in the giant axon of *Loligo*. *J. Physiol.*, 116(4):473–496, 1952.

BIBLIOGRAPHY

- [30] A.L. Hodgkin and A.F. Huxley. Currents carried by sodium and potassium ions through the membrane of the giant axon of *Loligo*. *J. Physiol.*, 116(4):449–472, 1952.
- [31] A.L. Hodgkin and A.F. Huxley. The dual effect of membrane potential on sodium conductance in the giant axon of *Loligo*. *J. Physiol.*, 116(4):497–506, 1952.
- [32] A.L. Hodgkin and A.F. Huxley. A quantitative description of membrane current and its application to conduction and excitation in nerve. *J. Physiol.*, 117(1):500–544, 1952.
- [33] A.L. Hodgkin, A.F. Huxley, and B. Katz. Measurement of current-voltage relations in the measurement of the giant axon of *Loligo*. *J. Physiol.*, 116(4):424–448, 1952.
- [34] A.L. Hodgkin and W.A.H. Rushton. The electrical constants of a crustacean nerve fibre. *Proc. Royal Soc. B*, 133:444–479, 1946.
- [35] A.V. Holden. A last wave from the dying heart. *Nature*, 392:20–21, 1998.
- [36] J.E. Hutchinson. Fractals and self-similarity. *Indiana Univ. Math. J.*, 30:713–747, 1981.
- [37] P.Ch. Ivanov, M.G. Rosenblum, C.-K. Peng, J. Mietus, S. Havlin, H.E. Stanley, and A.L. Goldberger. Scaling behaviour of heartbeat intervals obtained by wavelet-based time-series analysis. *Nature (London)*, 383:323, 1999.
- [38] T. Kaczynski, K. Mischaikow, and M. Mrozek. Computing homology. *Homology, Homotopy & Applications*, 5(2):233–256, 2003.
- [39] J. P. Keener. Waves in excitable media. *SIAM J. Appl. Math.*, 3:528–548, 1980.
- [40] J. P. Keener. Direct activation and defibrillation of cardiac tissue. *J. Theor. Biol.*, 178:314–324, 1996.

BIBLIOGRAPHY

- [41] J.P. Keener. A geometrical theory for spiral waves in excitable media. *SIAM J. Appl. Math.*, 46:1039–1056, 1986.
- [42] J.P. Keener and J.J. Tyson. Spiral waves in the Belousov-Zhabotinskii reaction. *Physica D*, 21:307–324, 1986.
- [43] J. Kigami. A harmonic calculus on the Sierpinski spaces. *Japan J. Appl. Math.*, 6:259–290, 1989.
- [44] J. Kigami. Harmonic calculus on p.c.f. self-similar sets. *Trans. Amer. Math. Soc.*, 335:721–755, 1993.
- [45] J. Kigami. Harmonic calculus on limits of networks and its application to dendrites. *J. Funct. Anal.*, 128:48–86, 1995.
- [46] J. Kigami. Laplacians on self-similar sets and their spectral distributions. *Progr. Prob.*, 37:221–238, 1995.
- [47] J. Kigami. Distributions of localized eigenvalues of Laplacians on post critically finite self-similar sets. *J. Functional Analysis*, 156:170–198, 1998.
- [48] J. Kigami. *Analysis on Fractals*. Cambridge University Press, 2001.
- [49] J. Kigami and M.L. Lapidus. Weyl’s problem for the spectral distribution of Laplacians on p.c.f. self-similar fractals. *Commun. Math. Phys.*, 158:93–125, 1993.
- [50] S. Kusuoka. A diffusion process on a fractal. In K. Ito and N. Ikeda, editors, *Probabilistic Methods on Mathematical Physics*, Proc. of Tanuguchi International Symp. (Katata & Kyoto, 1985) (Tokyo), pages 251–274. Kinokuniya, 1987.
- [51] B.B. Mandelbrot. How long is the coast of Britain? statistical self-similarity and fractional dimension. *Science*, 156:636–638, 1967.

BIBLIOGRAPHY

- [52] B.B. Mandelbrot. *Fractals: Form, Chance and Dimension*. Freeman, 1977.
- [53] B.B. Mandelbrot. *The Fractal Geometry of Nature*. Freeman, 1982.
- [54] D. Margerit and D. Barkley. Selection of twisted scroll waves in three-dimensional excitable media. *Phys. Rev. Lett.*, 86(1), 2001.
- [55] D. Margerit and D. Barkley. Large-excitability asymptotics for scroll waves in three-dimensional excitable media. *Phys. Rev. E*, 66:036214, 2002.
- [56] J. Nagumo, S. Animoto, and S. Yoshizawa. An active pulse transmission line simulating nerve axon. *Proc. IRE*, 50:2061–2070, 1962.
- [57] M. Obert, P. Pfeifer, and M. Sernetz. Microbial growth patterns described by fractal geometry. *J. Bacteriol.*, 172(3):1180–1185, 1990.
- [58] W. Rall. Electrophysiology of a dendritic neuron model. *Biophys. J.*, 2(2 pt. 2):145–167, 1962.
- [59] R. Rammal. Spectrum of harmonic excitations on fractals. *J. Physique*, 45:191–206, 1984.
- [60] R. Rammal and G. Toulouse. Random walks on fractal structures and percolation clusters. *J. Physique Lett.*, 44:L13–L22, 1983.
- [61] P. Rendell. A Turing machine in Conway’s game life. http://www.cs.ualberta.ca/~bulitko/F02/papers/tm_words.pdf#search=%22rendell%20turing%20life%22, 2001.
- [62] J. Rinzel and J.B. Keller. Travelling wave solutions of a nerve conduction equation. *Biophys. J.*, 13:1313–1337, 1973.
- [63] C. Rocsoreanu, A. Georgescu, and Giurgiteanu N. *The FitzHugh-Nagumo Model: Bifurcation and Dynamics*. Kluwer Academic Publishers, Boston, 2000.

BIBLIOGRAPHY

- [64] T. Shima. On eigenvalue problems for the random walks on the Sierpinski pre-gaskets. *Japan. J. Indust. Appl. Math.*, 8:127–141, 1991.
- [65] T. Shima. On eigenvalue problems for Laplacians on pcf self-similar sets. *Japan. J. Indust. Appl. Math.*, 13:1–23, 1996.
- [66] M.F. Shlesinger and B.J. West. Complex fractal dimension of the bronchial tree. *Phys. Rev. Lett.*, 67(15):2106–2108, 1991.
- [67] R. S. Strichartz. Fractafolds based on the Sierpinski gasket and their spectra. *Trans. Amer. Math. Soc.*, 355(10):4019–4043, 2003.
- [68] R. S. Strichartz and M. Usher. Splines on fractals. *Math. Proc. Cam. Phil. Soc.*, 129:331–360, 2000.
- [69] Robert S. Strichartz. *Differential Equations on Fractals: A Tutorial*. Princeton University Press, 2006.
- [70] Henry Tuckwell. *Introduction to Theoretical Neurobiology: Linear Cable Theory and Dendritic Structure*. Cambridge University Press, 1988.
- [71] J. J. Tyson and J. P. Keener. Singular perturbation theory of traveling waves in excitable media (A Review). *Physica D*, 32:327–361, 1988.
- [72] B.J. West, V. Bhargava, and A.L. Goldberger. Beyond the principle of similitude: Renormalization in the bronchial tree. *J. Appl. Physiol.*, 60(3):1089–1097, 1986.
- [73] Wikipedia. Conway’s game of life — wikipedia, the free encyclopedia. http://en.wikipedia.org/w/index.php?title=Conway%27s_Game_of_Life&oldid=75735214, 14 September 2006.
- [74] A.T. Winfree. Spiral waves of chemical activity. *Sci.*, 175:634–636, 1972.
- [75] A.T. Winfree. Rotating chemical reactions. *Sci. Amer.*, 230:82–95, 1974.

BIBLIOGRAPHY

- [76] M. Yamaguti and J. Kigami M. Hata. *Mathematics of Fractals*, volume 167 of *Translations of Mathematical Monographs*. American Mathematical Society, 1997.
- [77] V.S. Zykov. Analytical evaluation of the dependence of the speed of an excitation wave in a two-dimensional excitable medium on the curvature of its front. *Biophysics*, 25:906–911, 1980.
- [78] V.S. Zykov. Kinematics of the steady state circulation in excitable media. *Biophysics*, 25:329–333, 1980.
- [79] V.S. Zykov. *Modelling of Wave Processes in Excitable Media*. Manchester University Press, 1988.